# Graphene-Assisted Integrated Nonlinear Optics

by

Behrooz Semnani

A thesis
presented to the University of Waterloo
in fulfillment of the
thesis requirement for the degree of
Doctor of Philosophy
in
Electrical and Computer Engineering

Waterloo, Ontario, Canada, 2018

**Examining Committee Membership**

The following served on the Examining Committee for this thesis. The decision of the Examining Committee is by majority vote.

| | |
|---|---|
| External Examiner | Mikael Fogelström<br>Professor |
| Supervisor | Safieddin Safavi-Naeini<br>Professor |
| Supervisor | Amir Hamed Majedi<br>Professor |
| Internal Member | Michal Bajcsy<br>Professor |
| Internal Member | Dayan Ban<br>Professor |
| Internal-external Member | Anton Burkov<br>Professor |

I hereby declare that I am the sole author of this thesis. This is a true copy of the thesis, including any required final revisions, as accepted by my examiners.

I understand that my thesis may be made electronically available to the public.

## Abstract

The unique linear and massless band structure of graphene in a purely two-dimensional Dirac fermionic structure has ignited intense research since the first monolayer graphene was isolated in the laboratory. Not only does it offer new inroads into low-dimensional physics; graphene exhibits several peculiar properties that promise to widen the realm of opportunities for integrated optics and photonics. This thesis is an attempt to shed light on the exceptional nonlinear optical properties of graphene and their potential applications in integrated photonics. Following a theoretical exploration of light-graphene interaction, disruptive new insight into the nonlinear optics of graphene was generated. It now appears that graphene can efficiently enable photon-photon interaction in a fully integrated fashion. This property, taken together with ultrawideband tunability and ultrafast carrier dynamics could be fully exploited within integrated photonics for a variety of applications including harmonic generation and all-optical signal processing. The multidisciplinary work described herein combines theoretical modeling and experimentation to proceed one step further toward this goal.

This thesis begins by presenting a semiclassical theory of light-graphene interaction. The emphasis is placed on the nonlinear optical response of graphene from the standpoint of its underlying chiral symmetry. The peculiar energy- momentum dispersion of the quasiparticles in graphene entails a diverging field-induced interband coupling. Following a many-body study of the carrier relaxations dynamics in graphene, it will be shown that the charged carriers in the vicinity of the Dirac point undergo an unconventional saturation effect that can be induced by an arbitrarily weak electromagnetic field. The perturbative treatment of the optical response of graphene is revisited and a theoretical model is developed to estimate the nonlinear optical coefficients including the Kerr coefficient of graphene. The theoretical models are complimented by the experimental results.

The peculiar nonlinear optical properties of graphene together with its ablity to being integrated with optical platforms would render it possible to perform nonlinear optics in graphene integrated nanophotonic structures. Here, the suitability of graphene for nonlinear optical applications is investigated both theoretically and experimentally. The emphasis is placed on an on-chip platform for ultrafast all-optical amplitude modulation. The experimental results indicate strong all-optical modulation in a graphene-cladded planar photonic crystal nanocavity. This development relies heavily on the unique properties of graphene, including its fast carrier dynamics and the special phonon induced relaxation mechanism. Finally, the potential application of graphene based all-optical modulation in time resolved nonlinear spectroscopy is also discussed.

**Acknowledgements**

I would like to express my sincere appreciation to my advisers Prof. Safieddin (Ali) Safavi-Naeini and Prof. Hamed Majedi for their consistent support and encouragement over the course of my PhD program. Their patience, motivation, and immense knowledge pushed me forward towards pursuing my true calling despite of successive failures, imperfections and fears of an obscure outcome. Today, I am more determined to fly out of my comfort zone, wisely plan and boldly fight for my ambitions and inspirations, and to overcome my fears of an uncertain future.

My endless gratitude to my parents for their unconditional love and support. I am thankful to my father for his bright thoughts. He never forced me but always motivated me to pursue learning, instilling in me a sincere appreciation for reality. My mother who exposed me to her absolute love and kindness. I am grateful to my brother Ehsan who has been kind, generous and supportive in all stages of my life.

Special thanks to Prof. Philippe Tassin for his kind hospitality and scientific support during my stay in Chalmers University of Technology, Sweden. I extend my appreciation to Prof. Ermin Malic and his student Roland Jago for lending me their expertise and intuition. My interaction with great scientists working as a part of Graphene Flagship, turned my visit to Chalmers as a successful life experience.

I would like to thank Prof. Donna Strickland for her generous help and insightful advice during my experimental works. Her amazing understanding of experimental nonlinear optics has been extremely helpful to my research. It is my pleasure to thank my PhD committee members in University of Waterloo, Prof. Michal Bajcsy, Prof. Anton Burkov and Prof. Dayan Ban for their invaluable comments and suggestions on my research. I express my sincere appreciation to Prof. Mikael Fogelström who kindly attended my PhD defense as external examiner.

Many hands made my experimental achievements possible. In particular, I am indebted to Dr. Arash Rohani who taught me practical optics from basics to sophisticated tricks. Thanks to Dr. Milad Khoshnegar who has done most of the fabrications in this research work. I express my appreciation to Dr. Mohsen Raieszadeh for his generous help and support over my PhD program. I acknowledge very fruitful collaboration with Sidd Thakur. Thanks to all friends in CIARS, Dr. Hadi Amarloo , Dr. Aidin Taeb, Dr. Shahed Shahid, Naiemeh Ghafarian, Dr. Suren Gigoyan and Ardeshir Palizban. Special thanks to Dr. Daryoush Shiri and Dr. Anita Fadavi for all inspirations I constantly receive from their side. I appreciate all friends' wonderful advice, support, and friendship, both academically and personally.

I acknowledge all supports I received from Keysight Technologies during my experimental works. In particular, I would like to thank Peter Schweiger and Nizar Messaoud for their kind support of my project and investing on future. Without the amazing laser package that I borrowed from Keysight I would not be able to achieve a big part of my experimental results.

I acknowledge the partial financial support from Waterloo Institute for Nanotechnology (WIN), Natural Sciences and Engineering Research Council of Canada (NSERC), Blackberry, Rune Bernhardsson's Graphene Funding (Sweden) and a number of awards from University of Waterloo.

Last but not least, my gratitude goes to all my dearest friends in Waterloo without whom my PhD's journey would not have been filled with the wonderful times and enjoyable moments that we shared together. Special thanks to my dear friends Ali, Meysam, Mohsen and Hadi for being incredibly kind and nice.

## Dedication

To My Parents for Their Endless Love.

# Table of Contents

# List of Tables

# List of Figures

# Preface

The present study is intended, as far as possible, to provide new insights into the theory of light-graphene interaction and its potential applications in nonlinear integrated optics. Four years ago, I was intrigued to work on this topic because of two reasons; (i) as a researcher, I thought of myself as someone who could comprehend new physical concepts and apply them effectively to emerging engineering applications. This was coincidentally accompanied with (ii) an uptake of research in the area of graphene and other two-dimensional materials. Therefore, graphene was one of the accessible goals in my quite limited horizon besides the other targets that I spotted but failed to attack. Luckily, my supervisors gave me enough freedom and guidance to explore my inspirations.

# Chapter 1

# Introduction

*What we observe is not nature itself, but nature exposed to our method of questioning.*

*Werner Heisenberg*
*1901-1976*

## 1.1 Motivation

### 1.1.1 Integrated Optics: Demand for Optically Nonlinear Materials

The move over the last few years towards integrated photonics is considered an important turning point [1–3]. The strong desire of humankind to push for *the best and the next* ! has stimulated recent intense research recently in exploring robust and versatile alternatives for semiconductor electronics. Hopes for overcoming the key issues associated with electronic devices, including operational speed and power consumption impose limitations that must be surpassed [1,4–6]. Integrated-photonics promises ultrafast and low-power operation that can be exploited for many sought-after applications [1, 6, 7]. Photonic and optoelectronic

components are most often wavelength-scale and the adoption of photonic technology for highly miniaturized applications is thereby hindered by the diffraction limit [8].

The key advantages of employing light rather than electrons to perform a variety of functions, stem from the weak interaction of photons. Unlike electrons, photons do not 'see' each other. If photons flow inside a waveguide, they do not obstruct the path; therefore *resistance* in optical paths is negligible compared to their electrical counterparts. Electron-impurity and other elastic and inelastic scattering processes most often pose stronger limitations on the resistance of channels where charge carriers flow in. The fundamental limits on the operational speed of electronic devices can be attributed to the Coulombic interaction of electrons. The speed of CMOS technology is generally limited by the RC time constant associated with the charge buildup within the device. This time constant is obviously imposed by the interactive nature of electrons. We should remind ourselves that capacitance (C) is an electrostatic effect. Photons can overcome this electrical bottleneck, thus the operational speed of all-optical integrated devices is expected to be superior [9]. However, when a *signal light* is supposed to be manipulated by a *control light*, the weak interaction of photons becomes problematic. In order to facilitate interaction between photons, the nonlinear optical properties of materials can be exploited [10].

All-optical signal processing – i.e. the direct manipulation of signals in the optical domain–, is anticipated to offer ultrafast operation and low power consumption by avoiding power-hungry optical-electrical-optical conversions [11–18]. Integrated nonlinear optical devices usually utilize ultrafast nonlinear processes including intensity-dependent refractive index and saturable absorption to perform all optical signal processing at femtosecond time scale. The operational speed of such device is most often limited by the intrinsic relxation time associated with light-matter interaction [19]. Since many nonlinear operations rely on high intensities of the fields participating in the nonlinear process, both well-designed optical platforms and strongly nonlinear materials are required to execute nonlinear functionalities. The exploration of satisfactory nonlinear materials that are integrable with state-of-the-art optical platforms remains thereby an active area of research [20–22].

There are several key functions that are considered to be the main building blocks in integrated photonic circuits and all-optical schemes. The most crucial of these are wavelength-conversion, optical switching and modulation [1, 22].

Wavelength-conversion is the most basic function required for all-optical signal processing and nonlinear photonics [1, 23–25]. The applications are diverse and encompass several categories including harmonic generation [26–28], difference frequency generation [29], data-multiplexing [30, 31]. Depending on goals, different nonlinear processes in materials must be utilized. For example, the *instantaneous nonlinearities* of materials can be

exploited to generate higher harmonics through mixing multiple frequencies [32]. The key figure of merit used to evaluate the performane of such devices, is the conversion efficiency [26–28]. Focusing on harmonic generation specifically, a combination of large optical nonlinearities and structural configurations enabling enhanced intensities would minimize resource requirements and maximize the output power. For example, plasmonic structures offer extreme localization of electromagnetic fields enabling efficient fulfillment of the power requirement for harmonic generation [33].

Ultra-low-power all-optical switching and all-optical modulation are indispensable functions in all-optical schemes. Intrigued by the promise of all-optical devices to operate at a reduced-power level as well as extremely fast operational speed, , researchers have been intensely targeting on-chip all-optical switching [9, 15, 17, 34, 35]. All-optical switching devices exploit the Kerr-type nonlinearity of materials together with a resonant cavity to observe the bistable response [15, 35]. Optical bistable devices were extensively researched in the 1980s and 1990s [36], but these studies showed the limits of such devices for practical structures. The problems are particularly serious for silicon (Si) based structures because of the relatively poor Kerr nonlinearity of silicon. Although ultra-small and high quality factor cavities can potentially overcome the fundamental problems, Si-based optical bistable devices suffer from high operational power and small bandwidth. In principle the operational energy is scaled as $V_c/Q^2$, where $V_c$ is the characteristic mode volume and $Q$ is the quality factor of the corresponding mode [37]. For carefully-designed high-Q microcavities, theories predict optical bistability in the $\sim$ mW power range. However the cost we have to pay is difficulty in fabrication and measurement as well as very narrow operating frequency band.

Crucial role in photonic integrated circuits is played by optical modulation [21, 22]. Compared to widely available electronic and electro-optic modulators, all-optical modulation schemes offer intrinsic advantages in terms of higher bandwidth and lower loss [21]. Such devices take advantage of the Kerr-type nonlinearity or saturable absorption of the materials incorporated into a cavity or a waveguide to change the transmission properties of the optical structure. The operational speed of such a device is thus limited by the effective life time of photo-excited carriers [21]. Since the modulation essentially takes place through a nonlinear effect, field enhancement mechanisms are required to reduce the switching power.

Two important characteristics of material(s) executing nonlinear operations in integrated photonic circuits, were frequently repeated above; **strong optical nonlinearity** and **ultrafast carrier relaxation dynamics**. In recent years, graphene and other two-dimensional (2D) materials have attracted increasing attention for applications in optics and photonics. Compared to bulk semiconductors, 2D materials offer several advantages

rooted in their reduced dimensionality as well as their crystalline structure [20, 21, 38]. Flexibility, mechanical stability and some peculiar optical properties are the most apparent excepetional features of 2D crystals. Specifically, several experimental reports have verified that graphene exhibits strong optical nonlinearity and ultrafast carrier dynamics [39,40]. These unique optical properties together with the innate flexibility of graphene that can be incorporated into state-of-the-art optical platforms make it a viable candidate for integrated nonlinear optics. In this thesis, the nonlinear optical properties of this wonder material will be explored to evaluate its performance for future graphene-assisted nonlinear integrated photonics.

### 1.1.2 The Rise of Graphene

Carbon is an incredibly versatile element. Depending on how the atoms are arranged, it can produce a broad range of materials from hard diamonds to soft graphite. In particular, graphite is made of stacks of 2D carbon sheets bonded together by weak van der Waals interactions. Graphene was the name selected by Hanns-Peter Boehm for the basic building blocks of graphite [41]. Graphene is a monolayer of carbon atoms tightly packed into a 2D honeycomb lattice [42].

In the 1930s, Landau and Peierls argued that strictly 2D crystals were thermodynamically unstable and could not exist [43, 44]. According to their theory, thermal fluctuations in low-dimensional crystal lattices lead to the displacements of atoms. The displacements are comparable to interatomic distances at any finite temperature. From this vantage point, 2D electronic system can only exist as an integral part of a larger 3D structure. According to this theory, without a 3D base, 2D materials were presumed not to exist [43]. However, in 2004 A. K. Geim and K. S. Novoselov successfully isolated the first monolayer graphene sheet [45]. The common wisdom collapsed in the face of their evidence. It was experimentally demonstrated that strictly free standing 2D atomic crystals such as graphene and single-layer boron nitride could be transferred on top of non-crystalline substrates, in liquid suspension and as suspended membranes. This significant achievement triggered intensive research on graphene and other 2D materials [46, 47]. Its reduced dimensionality and the symmetries of its crystalline structure render graphene a gapless semiconductor. Graphene exhibits interesting electronic, optical and mechanical properties [48]. A large number of its material parameters, such as mechanical strength [49]and very high electrical and thermal conductivity are superior [48]. These properties suggest that graphene could replace other materials in existing applications [50].

The electrons which effectively contribute in the electronic properties of graphene possess a linear energy-momentum dispersion and thus effectively behave as massless Dirac

fermions [48]. Graphene can be considered as a 2D gas of charged particles obeying the relativistic Dirac equation, rather than the non-relativistic Shrödinger's equation [51]. The carriers in graphene mimic relativistic particles with zero mass and an effective relativistic speed of $\sim 10^6$m/s [48].

Graphene exhibits a wealth of exceptional electronic properties including a remarkably high mobility of the charge carriers in the room temperature [52], Klein tunneling and Zitterbewegung [53, 54], existence of a non-zero Berry's phase, anomalous quantum Hall effect [55–57], quantum limited intrinsic conductivity [58] and a unique Landau-level structure [59]. Underlying these peculiar electronic properties are its chiral pseudo-relativistic quasiparticles [42]. These properties combined with near-ballistic transport makes graphene a potential material for nanoelectronics, particularly for high-frequency applications such as ultrafast graphene transistors [60].

In addition to its distinctive transport and electronic properties, the optical response of graphene is also unique. The first manifestation of its unusual interaction with light is the visibility of the graphene monolayer. Interestingly, a graphene layer can be seen by the naked eyes, despite being only a single atom thick[1] [48]. For me as the author of this thesis, visibility of a monolayer graphene transferred onto quartz substrate was the first and perhaps, the most impressive experimental observation! Fig. 1.1 shows a photo of a graphene monolayer on a quartz substrate. The photo was taken simply with a cellphone camera! The existence of the graphene monolayer is readily perceivable by looking closely. It also appears colorless to the sight. This observation reveals the **strong and wideband** interaction of graphene with light. In Chapter 2, this effect will be explored thoroughly. It will be shown that the special symmetries existing in the crystalline structure of graphene lead to its strong interaction with light over a broad range of frequencies.

The linear dispersion of the Dirac electrons allows interband optical transitions at all photon energies. This strong dispersion-less interaction, in conjunction with large carrier mobility makes graphene an ideal material platform for integrated optics, photonics and nonlinear optics [34, 50]. It has been demonstrated that graphene can significantly boost the performance of many optoelectronic devices inlcding electro-optical modulators [61–64], photoreceivers [65], planar microcavity-enhanced photodetectors [66], photovoltaic [67], light-emitting devices [68]and finally saturable absorbers and ultrafast lasers [69].

[1] suspended graphene sheet presents $\sim 2.3\%$ broadband interband absorption.

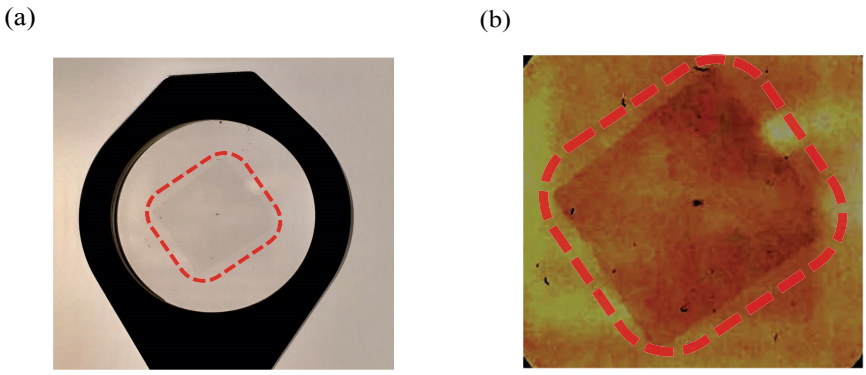


Figure 1.1: Observation of a graphene monolayer transferred onto a quartz substrate. (a) Photo taken by a cellphone camera!. Red square marks region where graphene (the square) is placed. (b) Zoomed photo after image processsing to provide a sharper contrast.

## 1.2 Scope of Thesis, Goals and Objectives

The first objective of the present study is to develop a comprehensive theoretical model that provides explicit expressions for the nonlinear response coefficients of graphene. In the absence of external symmetry-breaking, graphene as a centrosymmetric crystalline structure does not exhibit even-ordered nonlinear effects; the first nonlinear term is the third order term. This thesis presents an original formulation of nonlinear optical response of graphene exposed to continuous electromagnetic radiation. The adopted theory employs semiconductor Bloch equations (SBEs) to model the electron dynamics in the presence of an electromagnetic field.

As mentioned earlier, the charged carriers in graphene obey the relativistic Dirac equation and they possess the property of chirality. Chirality refers to a special electronic state in which the quantum state of the carriers are locked to the direction (and not magnitude) of their linear momentum. It has been demonstrated that all of the unconventional transport properties of graphene noted in Section 1.1.2, can be attributed to this feature of Dirac fermions [42, 70]. It is worth pointing out that, the chirality of the carriers and the Dirac-type dynamics are the robust properties of graphene that are rooted in the special symmetries existing in its crystalline structure and therefore cannot be violated by any moderate perturbation of the graphene's lattice. The impact of this chirality on the optical response of the graphene, despite its importance, has not been investigated in the literature. It will be argued that the chirality of charged carriers leads to a non-resolvable singularity in the nonlinear optical response of graphene obtained from perturbation theory;

In sharp contrast to ordinary semiconductors, in graphene, interband coupling mediated by an electromagnetic field is arbitrarily large in the vicinity of the Dirac point.

In an article published three years ago [71], I *proposed* that the aforementioned singularity can be resolved by introducing band-renormalization due to spin-orbit coupling. The quantum spin Hall effect opens up a gap and respects the symmetries of graphene, simultaneously. 'Although this band gap is very small, graphene as a critical electronic state can be strongly affected by this perturbation' I claimed. However, this claim could not be completely true since spin-orbit coupling can be cancelled out by a Rashba term arising from the substrate that graphene is placed on [72]. Although, several other theoretical models have been published within the last three years [73–75], a self-consistent theoretical model that can resolve the above issue is still lacking. In addition, many experimental studies of the nonlinear optics of graphene have been reported [39, 76–80] and some of their findings are difficult to reconcile with existing theoretical models. The source of the discrepancies between theoretical models and reported experiments has not been conclusively identified [74].

In this thesis, an original and self-consistent theory of light-graphene interaction is presented that can resolve the issues associated with the topologically protected chiral nature of carriers in graphene. Using SBEs to model the electronic dynamics, it will be shown that the charged carriers in the vicinity of the Dirac point undergo a *spontaneous saturation effect*. Here the terminology is not precisely matched to how it is used by condensed matter physicists. In this thesis 'spontaneous' refers to an effect that can be induced by an arbitrarily weak electromagnetic field. The theory is complemented by a many-body study of the carrier relaxation dynamics in graphene. It is demonstrated that the carrier relaxation dynamics is slow around the Dirac point, in turn leading to a more pronounced saturation. As a direct consequence of this effect, the optical response of graphene is essentially non-perturbative. The analysis shows that a perturbative treatment of the nonlinear optics of graphene is problematic in particular at small Fermi levels and large field amplitudes.

The overall result of above interpretations altogether enables me to derive original expressions for the nonlinear response coefficients of graphene including the Kerr coefficient. Ultimately, the Kerr coefficient of graphene is experimentally characterized using the z-scan technique. It is shown that the developed theory can predict the experimental results reasonably well.

The adopted theoretical model serves as the starting point to evaluate the performance of graphene in two distinct categories of nonlinear integrated optical devices; wavelength conversion and all-optical modulation. The performance of a wavelength-conversion device

composed of a plasmonic nanostructure integrated with graphene is numerically examined. The proposed structure is designed and optimized to harness the optical nonlinearity of graphene to generate the third harmonic of an intense near-infrared laser beam. In this particular application, the *instantaneous nonlinearity* of graphene is exploited, thus the use of field enhancement to maximize the light-graphene interaction is the only objective to be optimized.

As the second class of application, the performance of a graphene-cladded silicon photonic crystal nanocavity is experimentally investigated. The operational principle of the proposed device is based on the saturable absorption of graphene in the presence of high intensity illumination. As remarked earlier, the performance of such devices is evaluated based upon the amount of power required to execute modulation, maximum modulation depth and the operational speed (predominantly limited by the intrinsic relaxation time of photoexcited carriers within the nonlinear medium).

The list below summarizes the main objectives of this thesis.

- Develop a novel comprehensive quantum theoretical model to describe the nonlinear optical response of graphene. The theory is semiclassical, that is, the electromagnetic field is treated classically but the electron dynamics are modeled within the framework of quantum mechanics.
- Investigate the impact of chirality of the charge carriers of graphene on its optical response; leading to a new interpretation of light-graphene interaction.
- Experimental characterization of the Kerr coefficient of graphene as a measure of nonlinear optical response.
- Investigate the performance of graphene for optical third-harmonic generation (THG). Propose a graphene-based wavelength-conversion device.
- Experimental Investigation of graphene-integrated silicon photonic crystal cavities for all-optical modulation. This work is intended to evaluate the performance of graphene for future all-optical silicon based technology.

This thesis is comprised of five chapters. The contents of remainder of the thesis are summarized below.

In Chapter 2, a semiclassical theory of light-graphene interaction is developed. Explicit expressions for the linear and nonlinear conductivity tensors are derived based on SBEs.

Three main additive mechanisms contribute to the nonlinear optical response of graphene: pure intraband, pure interband and the interplay between them. For each contribution, explicit response functions are derived. It is shown that the topologically protected chirality of charged carriers leads to a diverging field -induced interband coupling which causes charged carriers at the vicinity of the Dirac point to undergo ultrafast Rabi oscillations. These oscillations occur at a much faster rate than they relax. Therefore, an unconventional optical saturation takes place. The Kerr coefficient of graphene is experimentally characterized using z-scan technique. The measurement results are presented.

In Chapter 3, a general recipe is proposed to design an efficient graphene integrated plasmonic structure for third harmonic generation (THG). Specifically, the design procedure for an integrated graphene-based ultra-violet light generator is presented. In order to enhance the field intensity at the graphene layer, two distinct mechanisms are utilized. A multilayer Bragg structure is used as a Perfect Magnetic Conductor (PMC) to make a constructive interference between the incident and reflected fields at the graphene layer. A periodic array of shaped resonant gold nanoparticles is placed on top of the graphene sheet to enhance the field intensity due to plasmonic resonance at the fundamental frequency. A hybrid and fast numerical method based on scattering matrix of Floquet modes and the Generalized Multipole Technique (GMT) is also proposed to analyze the periodic structure. This numerical method is used to optimize the dimensions of the multilayer structure and boost the nonlinear conversion efficiency by more than $10^6$ times.

In Chapter 4, a new experimental demonstration of all-optical modulation in a graphene-cladded photonic crystal nanocavity is presented. The experimental characterization of the structure is performed using a cross-polarized confocal reflectometry setup. A graphene monolayer is transferred onto a photonic crystal double heterostructure nanocavity. This changes its resonance spectrum . The modulation is executed by an ultrafast pulse laser shining onto the structure which changes the optical absorption of the graphene monolayer through the saturation effect. A relatively strong modulation effect is achieved and this is partly attributed to the ultrafast relaxation dynamics of graphene. Meanwhile, the experimental results indicate that the slow relaxation dynamics caused by the charge injection from the graphene into the silicon cavity can also contribute to the modulation effect.

In Chapter 5, a summary of contributions as well as suggested directions for future work are presented.

# Chapter 2

# Nonlinear Quantum Optical Properties of Graphene

*A Semiclassical Theory*

## 2.1 Introduction

Graphene is a two dimensional arrangement of the carbon atoms sitting in a honeycomb lattice, a seemingly simple lattice structure that nonetheless underlies the special transport and optical properties [48]. The band structure of graphene differs substantially from other condensed matter systems. The effective Hamiltonian describes pseudo-relativistic quasiparticles obeying the $(2+1)$-dimensional Dirac equation. In the context of QED, the electronic excitations introduced by such dynamics can be considered as massless chiral fermions [46].

Graphene exhibits a variety of peculiar properties that are manifestations of the special symmetries of its crystalline structure and relativistic energy spectrum of charged carriers. Symmetries entail several unconventional properties such as the existence of a topologically protected zero-energy state, Berry phase, anomalous quantum Hall effect and Zitterbewegung ('trembling motion') [48, 70, 81]. It is counterintuitive that graphenes conductivity never falls below a minimum value corresponding to the quantum limit of conductance ( i.e. $e^2/\hbar$ ) even at zero temperature and zero carrier concentration. It can be shown that the minimum conductivity is an intrinsic property of the Dirac Fermions inherited by the Dirac quasiparticles in graphene. The Dirac type dynamics strongly suppresses short range

localization effects. In the absence of the localizations effects, the Mott's argument can be invoked to qualitatively explain the physical origin of the *quantum limited conductance*. According to Mott, the mean free path of the charged carriers in metallic systems cannot be shorter than their Broglie wavelength. In graphene the electrons around the Dirac points have diverging wavelength and hence they can freely travel throughout the lattice. As a result, a quantum limited conductivity is anticipated [46]. All these odd properties can also be linked to the chiral behavior of the carriers. In graphene the pseudospin is locked parallel or antiparallel to the direction along which the electron propagates and so the quasiparticles possess the property of chirality [42].

The optical response of graphene is also expected to be influenced by the chiral nature of the carriers and the scale invariance of the band structure in low energy limit. However, despite its importance, a theoretical study on the unconventional optical response of graphene is still lacking. The optical response of graphene in the linear regime has been investigated theoretically and experimentally [82–87]. Graphene as a scale invariant two dimensional chiral electronic system exhibits universal optical response [88]. A simple analysis based on linear response theory shows that an isolated graphene sheet can absorb about 2.3% of the normally incident optical field, which is indeed a huge number for a monolayer atomic structure.

The nonlinear optical response of graphene has been a topic of intensive research in the recent years [39, 73, 89–96]. Treatment of the nonlinear optical response of graphene in the framework of quasiclassical Boltzman equation predicts strong nonlinearity in the terahertz range of frequency, neglecting pair productions and interband transitions [89]. This part of nonlinearity is mainly due to the geometrical properties of band structure rather than its topological aspects [97]. The calculation of optical response of graphene in time domain has been carried out in Ref. [91]. Wrighte *et al.* have performed Fourier analysis of the dirac equation to obtain the optical response of the system for a given incident field [90]. All existing time domain methods proceed primarily at the level of the wavefunction, rather than at the level of the density matrix and thereby suffer from the computational cost and the difficulty resulted from the inclusion of relaxation processes due to impurities and emission , and many-body interactions.

The treatment of optical response of graphene, in a simplistic manner, proceeds from single particle approximation and the equation of motion for density matrix. The formal approach to calculate the optical response of semiconductors, excited by a electromagnetic field, is based on perturbative expansion of the density matrix and taking all possible transitions into account [32,95]. Even at such a reasonably simplistic treatment, the evaluation of nonlinear response coefficients is numerically difficult and does not provide any intuitive insight. To circumvent these difficulties, Semiconductor Bloch Equations (abbreviated as

SBEs) [98] for graphene are employed. The SBEs provide a convenient mathematical tool allowing idenification of the cooperative intraband and interband dynamics. It is shown that, light-graphene interaction can be perceived as the interaction of light and an ensemble of inhomogenously broadened two level systems concurrently evolved by an adiabatic intraband dynamics.

Semiconductor Bloch Equations [99] have extensively been used to calculate the nonlinear optical response of semiconductors [98, 100]. In Ref. [101] the derivation of SBEs for graphene beyond the Dirac cone approximation has been discussed. In Ref. [102] the general treatment of the SBEs for graphene including electron-electron interactions and exciton effects is presented. Using SBEs, the problem of interaction can be treated in a semiclassical manner leading to numerically amenable expressions for arbitrary orders of interaction.

The SBEs introduce an effective dipole (interband dipole matrix element) in the reciprocal space that reveales peculiarities of graphene in terms of its optical response. As a direct consequence of the chirality of the charged carriers, the interband dipole matrix element obtained within the *length gauge* carries a first order singularity at the degeneracy points which is in sharp contrast to ordinary (and other even gapless) semiconductors [71, 103]. The anomalous mathematical structure of the interband dipole matrix element has raised some controversies in treatment of the optical response of graphene [71, 74]. Specifically, the perturbative treatment of the nonlinear optical response has not been trouble free; the higher order optical response coefficients of graphene obtained by means of the perturbation theory inherit a nonresolvable singularity [71]. Although a huge amount of effort has been spent on developing the nonlinear optical response of graphene [73–75], a self-consistent theoretical model, which can resolve the above issue, is still lacking.

In this chapter we present original derivations for the nonlinear optical response of graphene based on a semicassical theory. We will adopt an approach that treats the electrons dynamics in the presence of a moderate intensity electromagnetic field based on SBEs. It will be demonstrated that the higher order nonlinear response of graphene, possesses a singularity due to the topological properties of the band structure and the chiral nature of the charged carriers. We reveal the physical implication of the singularity. Following a many-body analysis, it will be argued that the electromagnetic field causes the charged carriers in the vicinity of the Dirac points undergo ultra-fast Rabi oscillations accompanied with slow relaxation dynamics, which, intriguingly, yields an unconventional saturation effect. The perturbative treatment of the optical response of graphene is revisited to account for the extreme nonlinear interaction in the vicinity of the Dirac points. The theory consistently resolves the aforementioned singularity by excluding the saturated states from the solution domain.

The theoretical predictions have been examined by direct experimentation. The Kerr coefficient of graphene has been measured using the well-known z-scan technique and a reasonable agreement between our theoretical results and our experimental results is achieved.

This chapter is organized as follows. In section. 2.2 the Hamiltonian of graphene within the tight binding approximation is derived. In section. 2.3 we address the question of how the chirality of carriers affects the optical response of graphene and its dependence on the fundamental group symmetries of the problem. Section 2.4 is devoted to constructing the semiclassical model used to treat light-graphene interaction that ends up with graphene Bloch equations. In Section. 2.5 we propose a perturbative (iterative) approach to solve the effective optical Bloch equations and address the issues associted with the chiral dynamics of the carriers in pertubative treatment of the optical response of graphene. In section 2.6, we will proceed to reveal the unconventional saturation effect in graphene. Since nonadiabatic nonlinear interactions are strongly influenced by relaxation dynamics, a full many-body analysis will be performed to accurately find the dephasing and population relaxation. The theory is substantiated by a direct time domain analysis. Section 2.7 is devoted to *semi-perturbative* treatment of the nonlinear optical response of graphene. The numerical and experimetal results are presented in sections 2.8 and 2.9, respectively. We summarize our findings in section 2.10. Concrete derivations are presented in the appendices.

## 2.2 Graphene Hamiltonian and Equations of Motion

Graphene has a honeycomb crystal lattice with two lattice points per elementary cell. They belong to two sublattices A and B where the nearest neighbours of the sites of one of them are sites belonging to the other sublattice (a bipartite lattice). In Fig. 2.1(a) atoms in A and B sublattices are shown by blue and red balls respectively. The Bravais lattice is triangular with the lattice vectors, $\mathbf{a}_1 = a\left(\frac{3}{2}\hat{x} + \frac{\sqrt{3}}{2}\hat{y}\right)$ and $\mathbf{a}_2 = a\left(\frac{3}{2}\hat{x} - \frac{\sqrt{3}}{2}\hat{y}\right)$ [48]. As shown in Fig. 2.1(b) the reciprocal lattice is also hexagonal with rhomboidal unit cell. The high symmetry crystallographic points are presented in Fig. 2.1(b).

We assume that the graphene monolayer (laying on the xy-plane) interacts with a plane wave illuminating graphene in the perpendicular direction. This assumption allows us to use the electric dipole approximation in which the effect of magnetic field is excluded. This approximation is quite accurate for an ideal graphene sheet wherein electrons are strongly bounded and their off-plane dynamics is negligible. The electric field can have an arbitrary time variation containing different harmonics. The dynamical properties of the

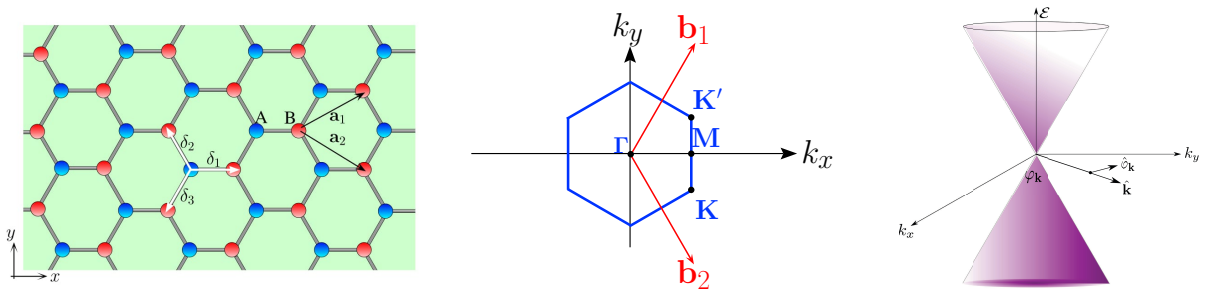


(a) (b) (c)

Figure 2.1: (a) Graphene lattice and (b) its reciprocal lattice formed by $\mathbf{b}_1 = \frac{2\pi}{3a}\left(\hat{x} + \sqrt{3}\hat{y}\right)$ and $\mathbf{b}_2 = \frac{2\pi}{3a}\left(\hat{x} - \sqrt{3}\hat{y}\right)$ , (c) Dirac points $\mathbf{K}'\left(\frac{2\pi}{3a}, \frac{2\pi}{3\sqrt{3}a}\right)$ and $\mathbf{K}\left(\frac{2\pi}{3a}, -\frac{2\pi}{3\sqrt{3}a}\right)$ are shown in the figure .The schematic plot of dispersion relation around the Dirac point.

positively charged ions that constitute the host lattice of the crystal will be neglected in our formulations. The system Hamiltonian for a single graphene sheet interacting with a classical electromagnetic field within the single particle approximation is

$$\hat{H} = \hat{H}_0 + \hat{H}_I \tag{2.1}$$

Where $\hat{H}_0$ governs the dynamics of the electrons with mass $M$ in the presence of the periodic lattice potential $V(\mathbf{r})$

$$\hat{H}_0 = \int d^3\mathbf{r}\hat{\Psi}^\dagger(\mathbf{r})\left\{\frac{\hat{\mathbf{p}}^2}{2M} + V(\mathbf{r})\right\}\hat{\Psi}(\mathbf{r}) \tag{2.2}$$

Where $\hat{\Psi}(\mathbf{r})$ is the field operator. The interaction Hamiltonian in long-wavelength limit (or normal incidence) is rigorously obtained in the *velocity-gauge* by replacing the canonical momentum $\mathbf{p}$ by $\mathbf{p}+e\mathbf{A}$ in $\hat{H}_0$ where $\mathbf{A}$ is the associated vector magnetic potential [100]. In the case of graphene it seems very simple to use this electrodynamics substitution, however it can be shown that neither the calculations are efficient, nor it reveals some interesting physical properties. This will be further detailed in the succeeding sections and a through discussion on the validity of the valocity gauge in the Dirac dynamics is presented in the in Appendix. A. The interaction problem can be recast into the *length gauge*

$$\hat{H}_I = e\mathbf{E}_{in}(t) \cdot \int d^3\mathbf{r}\hat{\Psi}^\dagger(\mathbf{r})\mathbf{r}\hat{\Psi}(\mathbf{r}) \tag{2.3}$$

A common problem with the perturbation theory for solids in the length gauge is the difficult treatment of the position operator $\mathbf{r}$ in view of the extended Bloch states [100].

This is further detailed in the next section. It will be shown that both $\hat{H}_0$ and $\hat{H}_I$ can be treated in the framework of the Tight-Binding (TB) regime. Taking into account the nearest-neighbor hopping with the hopping parameter $\kappa \approx -2.97$eV [104] along $\boldsymbol{\delta}_1$, $\boldsymbol{\delta}_2$ and $\boldsymbol{\delta}_3$ bonds (shown in Fig.2.1) the TB Hamiltonian in the momentum space is

$$\hat{H}_0 = \sum_{\mathbf{k}} E_0 \left( \hat{a}^\dagger_{\mathbf{k}} \hat{a}_{\mathbf{k}} + \hat{b}^\dagger_{\mathbf{k}} \hat{b}_{\mathbf{k}} \right) + \kappa \sum_{\mathbf{k}} \left[ f(\mathbf{k}) \hat{a}^\dagger_{\mathbf{k}} \hat{b}_{\mathbf{k}} + f^*(\mathbf{k}) \hat{b}^\dagger_{\mathbf{k}} a_{\mathbf{k}} \right] \tag{2.4}$$

The operators $\hat{a}_{\mathbf{k}}$ and $\hat{b}_{\mathbf{k}}$ are fermionic annihilation operators on A and B sublattices respectively. $E_0$ is the result of the hopping processes within the sublattices. The first term on the right hand side of the Eq. (2.4) is symmetrically diagonal and does not affect the quasi-particles dynamics. The function $f(\mathbf{k}) = \sum_{i=1}^{3} \exp(i\mathbf{k}.\boldsymbol{\delta}_i)$ carries the symmetry properties of the graphene lattice. The TB Hamiltonian $\hat{H}_0$ becomes diagonal in the conduction and valence basis

$$\hat{\xi}_{\mathbf{k}c} = \frac{1}{\sqrt{2}} \left( e^{-i\alpha_{\mathbf{k}}/2} \hat{a}_{\mathbf{k}} + e^{+i\alpha_{\mathbf{k}}/2} \hat{b}_{\mathbf{k}} \right) \tag{2.5a}$$

$$\hat{\xi}_{\mathbf{k}v} = \frac{1}{\sqrt{2}} \left( e^{-i\alpha_{\mathbf{k}}/2} \hat{a}_{\mathbf{k}} - e^{+i\alpha_{\mathbf{k}}/2} \hat{b}_{\mathbf{k}} \right) \tag{2.5b}$$

where $f(\mathbf{k}) = |f(\mathbf{k})| \exp(i\alpha_{\mathbf{k}})$. This yields the corresponding TB-based band structure

$$E^{c/v}_{\mathbf{k}} = E_0 \pm \kappa \, |f(\mathbf{k})| \tag{2.6}$$

First order expansion of the Hamiltonian around the conical points yields a massless Dirac quasiparticle whose dispersion relation is $E_{\mathbf{k}} = \pm \hbar v_F k$. It is noted that $v_F = -3a\kappa/2\hbar$ is the Fermi velocity which is around $c/300$. Within the band structure picture the effective Hamiltonian is

$$\hat{\mathcal{H}} \approx \sum_{\mathbf{k}} \hbar v_F k \left( \hat{\xi}^\dagger_{\mathbf{k}c} \hat{\xi}_{\mathbf{k}c} - \hat{\xi}^\dagger_{\mathbf{k}v} \hat{\xi}_{\mathbf{k}v} \right) \tag{2.7}$$

where $\hat{\xi}_{\mathbf{k}c}$ and $\hat{\xi}_{\mathbf{k}v}$ are the conduction and valence annihilation operators in the upper and lower energy bands, respectively. As long as the inter-valley scattering is improbable the local behavior of the Hamiltonian around $\mathbf{K}$ and $\mathbf{K}'$ is independent. In this work, the many-body interactions such as electron-electron and electron-phonon interactions will be phenomenologically incorporated into the dynamical equations via relxation coefficients. This assumption allows us to use the single particle picture where the system is adequately described by *atomistic* language. For mathematical convenience the matrix representations are used in the derivation of the equations of motion. A more rigorous treatment of the problem would involve including other band renormalizations such as a modification of

the Fermi velocity (i.e. $v_F$) due to many body columbic interactions [105]. However, the present approach is faithful enough to capture the essential physics.

Assume that the two-component spinors $\begin{pmatrix}1 & 0\end{pmatrix}^T$ and $\begin{pmatrix}0 & 1\end{pmatrix}^T$ are adopted for $A$ and $B$ states respectively. The resulting time-dependent Dirac equation describing low energy excitation around one of the conical points is written as

$$\hat{\mathcal{H}}_{\mathbf{k}} = \hbar v_F \mathbf{k} \cdot \vec{\sigma} \tag{2.8a}$$

$$i\hbar \frac{\partial}{\partial t} \overline{\Psi}_{\mathbf{k}} = \hat{\mathcal{H}}_{\mathbf{k}} \overline{\Psi}_{\mathbf{k}} \tag{2.8b}$$

where $\overline{\Psi}_{\mathbf{k}}$ is a two-component spinor in the momentum space and $\vec{\sigma}$ is made from the Pauli matrices $\vec{\sigma} = \hat{x}\sigma_x + \hat{y}\sigma_y + \hat{z}\sigma_z$ arose form the two sublattices. The optical response of graphene can be studied in a physically transparent way using the equation of motion for the density matrix. In Section. 2.4 we examine the nonlinear optical response of graphene based on the time evolution of the density matrix. Liouville's equation governs the time progress of the density matrix and it yields coupled differential equations. The single particle Liouville's equation in graphene reads

$$i\hbar \frac{\partial}{\partial t} \hat{\rho}_{\mathbf{k}} = [\hat{H}, \hat{\rho}_{\mathbf{k}}] \approx [\hat{\mathcal{H}}_{\mathbf{k}}, \hat{\rho}_{\mathbf{k}}] + [\hat{H}_I, \hat{\rho}_{\mathbf{k}}] \tag{2.9}$$

The first term on the right hand side of Eq. (2.9) is the regular dynamical phase variation. In the next section it will be shown that the second term is closely related to the Berry connection and topological properties of the band structure. This is the point where chiral nature of the carriers and strong optical response of graphene tie up. In the next section, an intuitive clue will be provided in a general formalism of two-band systems.

## 2.3 Two-Band Systems and the Role of Chirality

To illustrate the impact of the chiral nature of the charged carriers on the optical response of graphene and to explore the uniqueness of the graphene in terms of its strong nonlinear interaction with light, the mathematical description of chirality for a general two-level systems is presented. We also address applicability of the reduced TB basis to describe the matrix elements of the interaction Hamiltonian in the length gauge and its connection with chirality of the charged carriers. In the last part of this section, it is shown that, our arguments are general enough and they are independent of the approximation existing in TB calculations. Chirality and its influence on the optical response root in the discrete symmetries existing in the crystalline structure of graphene and inclusion of the many body effects and the other higher order interaction terms do not alter the general conclusion.

### 2.3.1 Two-band systems

A prototypical two-band system might be described by the Hamiltonian expanded in terms of the Pauli matrices as

$$\hat{H} = \varepsilon_0(\mathbf{k})\hat{I} + \varepsilon(\mathbf{k})\vec{u}(\mathbf{k}).\hat{\vec{\sigma}} \tag{2.10}$$

where $\varepsilon_0(\mathbf{k})$ and $\varepsilon(\mathbf{k}) > 0$ are real functions of Bloch wavenumber $\mathbf{k}$. The three-dimensional vector operator $\hat{\vec{\sigma}}$ is made from the Pauli matrices and $\hat{I}$ is a $2 \times 2$ identity matrix. The vector $\vec{u}(\mathbf{k})$ is a three dimensional unit vector and can be represented in terms of the spherical angle variables $\alpha$ and $\beta$

$$u_x(\mathbf{k}) = \sin\beta(\mathbf{k})\cos\alpha(\mathbf{k}) \tag{2.11}$$
$$u_y(\mathbf{k}) = \sin\beta(\mathbf{k})\sin\alpha(\mathbf{k}) \tag{2.12}$$
$$u_z(\mathbf{k}) = \cos\beta(\mathbf{k}) \tag{2.13}$$

One can find the eigenvectors correspond to two energy eigenvalues $E_\pm(\mathbf{k}) = \varepsilon_0(\mathbf{k}) \pm \varepsilon(\mathbf{k})$ of the Hamiltonian as [106]

$$|\mathbf{k},\uparrow\rangle = \begin{bmatrix} \cos\left(\frac{\beta}{2}\right) e^{-i\alpha/2} \\ \sin\left(\frac{\beta}{2}\right) e^{+i\alpha/2} \end{bmatrix} \tag{2.14}$$

$$|\mathbf{k},\downarrow\rangle = \begin{bmatrix} \sin\left(\frac{\beta}{2}\right) e^{-i\alpha/2} \\ -\cos\left(\frac{\beta}{2}\right) e^{+i\alpha/2} \end{bmatrix} \tag{2.15}$$

For a $d$-dimensional electronic system the Bloch momentum $\mathbf{k}$ can be represented by its magnitude $k$ and $d-1$ angle variables in the spherical coordinates, $\{\gamma_1, \gamma_2, \cdots, \gamma_{d-1}\}$. For the sake of brevity all angle variables are conveniently called $\gamma$. For the particular case of graphene the system is two-dimensional and only the azimuthal angle $\varphi_{\mathbf{k}}$ [1] is needed to determine the direction of the Bloch momentum in the reciprocal space. Suppose a prototype Hamiltonian in which $\vec{u}$ is a function of angle variables only, i.e. $\vec{u} = \vec{u}(\gamma)$, with no dependency on $k$, this is known as a *general chiral system* [88]. For such a system $\alpha$ and $\beta$ appearing in Eqs. (2.14) and (2.15) only depend on the angle variables. Equivalently the pseudospin is determined by the direction of the momentum.

According to Eq. (2.8b) it is obvious that the low energy Hamiltonian in graphene describes a scale invariance chiral electronic system. The chiral symmetry of the carriers is not restricted to the TB model but stems from the honeycomb translational symmetry of the crystalline structure.

[1] $\varphi_{\mathbf{k}}$ is the angle of vector $\mathbf{k}$ with respect to the $k_x$ axis shown in Fig. 2.1(c).

### 2.3.2 Position operator: the role of chirality

To examine the importance of chirality in the optical response of graphene, we now turn our attention to the calculation of matrix elements of the interaction Hamiltonian in the length gauge. As mentioned earlier, the calculation of matrix elements of the position operator in different Bloch states is challenging and it has caused some controversies [100, 107]. For the general case of extended Bloch states with spatial dependency of $\Psi_{n\mathbf{k}}(\mathbf{r}) = \langle \mathbf{r}|n,\mathbf{k}\rangle = \exp(i\mathbf{k}.\mathbf{r})u_{n\mathbf{k}}(\mathbf{r})$ where $u_{n\mathbf{k}}$ is the periodic part of the wavefunction, the matrix elements of the position operator are related to Berry connection tensor [107]. It is also shown [107] that $[\hat{\mathbf{r}}, \hat{\rho}_{\mathbf{k}}]$ appeared on the left hand side of Eq. (2.9) can be expressed as

$$[\hat{\mathbf{r}}, \hat{\rho}_{\mathbf{k}}] = -i\nabla_{\mathbf{k}}\hat{\rho}_{\mathbf{k}} + [\overline{\overline{\mathbf{A}}}_{\mathbf{k}}, \hat{\rho}_{\mathbf{k}}] \tag{2.16}$$

where $\overline{\overline{\mathbf{A}}}_{\mathbf{k},nm} = -i\langle u_{n,\mathbf{k}}|\nabla_{\mathbf{k}}|u_{m,\mathbf{k}}\rangle$ is the Berry connection tensor. In order to compute the Berry connection tensor rigorously, the full machinery of Density Function Theory and Wannier interpolation scheme should be used [107]. Introducing maximally localized Wannier basis functions provides a numerically feasible scheme to evaluate the matrix elements. It is straightforward to show that in the proper gauge that the basis functions are expanded around the atomic centers $\mathbf{r}_\alpha$ as

$$\Psi_{n,\mathbf{k}}(\mathbf{r}) = \sum_{\mathbf{R},\alpha} C_{\alpha,n\mathbf{k}} \exp\left[i\mathbf{k}.(\mathbf{R}+\mathbf{r}_\alpha)\right] \phi_\alpha(\mathbf{r}-\mathbf{R}-\mathbf{r}_\alpha)$$

where $\phi_\alpha$s are the localzied wavefunctions. The right hand side of Eq. (2.16) reads

$$[\hat{\mathbf{r}}, \hat{\rho}_{\mathbf{k}}] = -i\nabla_{\mathbf{k}}\hat{\rho}_{\mathbf{k}} + [\overline{\overline{\boldsymbol{\zeta}}}_{\mathbf{k}}, \hat{\rho}_{\mathbf{k}}] \tag{2.17}$$

where $\boldsymbol{\zeta}_{\mathbf{k},nm} = -i\sum_\alpha C_{\alpha,n\mathbf{k}}\nabla_{\mathbf{k}}C_{\alpha,m\mathbf{k}}$ is closely related to the Berry connection tensor. Localization of basis functions is the basic principle that underlines this approximation. Fortunately, for the case of graphene the basis functions are fairly well localized and this approximation works well. It is worth mentioning that both terms appearing on the right hand side of Eq. (2.17) are gauge dependent, but the overall expression is independent of gauge and the specific choice of basis functions. For the particular case of two band chiral systems described in the previous section, the Berry connection exhibits singular behavior at the degeneracy points. Energy eigenstates only depend on the angular variables $\gamma_i$'s. Therefore the gradient operator acting on the angular functions will be

$$\nabla_{\mathbf{k}}C_{\alpha,\mathbf{k}n} = \frac{1}{k}\sum_i \hat{\gamma}_i \frac{1}{h_i(\gamma)}\frac{\partial}{\partial\gamma_i}C_{\alpha,\mathbf{k}n} \tag{2.18}$$

where $kh_i(\gamma)$ and $\hat{\gamma}_i$ are respectively, the Riemann scale function and the unit vector associated with the angle variable $\gamma_i$. The appearance of $1/k$ term in the Liouville equation is the main difference between graphene and an ordinary semiconductor material. It is shown in the next section that this term acts like a dipole in the reciprocal space, playing a significant role in the graphene's nonlinear optical response.

### 2.3.3 Chirality and symmetry

Basically, low energy excitations that capture the universal characteristics of the system are highly influenced by symmetries. Let us focus on the effective Hamiltonian governing electrons dynamics around the Fermi energy level including band renormalizations due to electron-electron interactions. In this thesis we will not plunge into the Landau theory and just symmetry considerations are discussed here. As long as the two Dirac points can be treated as independent entities, first order expansion of the Hamiltonian around the conical points reads

$$\hat{H}^{eff}_{\mathbf{k}} \approx \sum_{i,j} k_i A_{ij} \hat{\sigma}_j + m(\mathbf{k})\hat{\sigma}_z \tag{2.19}$$

where $i$ and $j$ run over $x$ and $y$. The coefficients $A_{ij}$'s are the elements of a $2 \times 2$ constant real matrix. The mass term $m(\mathbf{k})$ can be expanded as $m(\mathbf{k}) = m_0 + k_x m_x + k_y m_y$. Based on the mathematical description of the chirality elucidated above, it is straightforward to show that the necessary and sufficient condition to have a chiral system in low energy limit is $m_0 = 0$, which implies gapless state. It can be shown that the Dirac fermions (gapless property) are topologically protected [97,108]. Two main symmetries characterize the graphene lattice: time reversal and inversion symmetry. The time reversal symmetry exists in the absence of any external magnetic field. The inversion symmetry emerges if the original Hamiltonian is conserved upon inversion with inversion center in the middle of the hexagonal lattice. These symmetries guarantee the *local stability* of the Dirac points [108]. However, a large enough perturbation may open up a gap. This is prevented by the $C_{3v}$ existing in the graphene lattice which guarantees the *global stability* of the Dirac points [108].

In the subsequent sections it will be shown that this chiral behavior leads to a singularity in higher order optical response of graphene. In 2005, Kane and Mele showed that at sufficiently low energy an isolated graphene exhibits a quantum spin Hall effect with an energy gap induced by spin-orbit interaction [109]. The spin-orbit coupling Hamitonian reads [109]

$$\hat{H}_{so} = -\Delta_{so}\hat{\sigma}_z\hat{\tau}_z\hat{s}_z + \lambda_R\left(\hat{\sigma}_x\hat{\tau}_z\hat{s}_y - \hat{\sigma}_y\hat{\tau}_0\hat{s}_x\right) \tag{2.20}$$

where $\hat{\sigma}_i$ , $\hat{\tau}_i$ and $\hat{s}_i$ are Pauli matrices acting on pseudospin, valley index and electron spin respectively. The coefficients $\Delta_{so}$ and $\lambda_R$ are microscopic spin-orbit coupling constant and Rashba coefficient, (as a result of breaking mirror symmetry) respectively. The spin-orbit coupling factor $\Delta_{so}$ can be affected by curvature of the graphene sheet. The reported value for this coefficient for the ideal case of flat defect-free graphene is $\Delta_{so} \approx 1\mu$eV [110]. The Rashba term could be present as a result of symmetry breaking by the substrate that graphene is placed on. The resulting energy gap is $2(\Delta_{so} - \lambda_R)$. Although this small gap can remove the singularity in the optical response of graphene, the interband coupling is still really strong in the vicinity of the Dirac point. It is worth noting that, the band gap openning resulted from the spin-orbit coupling is much smaller than thermal fluctuations in the room temperature (i.e. $k_B T \gg \Delta_{so}$). Moreover, the Rashba term can effectively cancel out the spin-orbit coupling and annihilate the gap. Accordingly, we would safely ignore the spin orbit Hamitonian in the rest of this chapter. The physical implication of the strong interband coupling will be discussed in section 2.6.

## 2.4 Semiconductor Bloch Equations for Graphene

As mentioned in the preceding sections, within the single particle approximation, the density matrix obeys dynamical equations in Schrödinger's picture. The applied field drives the distribution out of equilibrium leading to a nonvanishing induced current. For the specific case of a continuous excitation, the dynamical equations on the density matrix can be recast into the form of the Semiconductor Bloch Equations (SBEs). Based on SBEs the dynamics is governed by a quasiclassical theory with quantum fluctuations superimposed. The quantum corrections to the classical dynamics will be converted to the well known problem of light-atom interaction [32].

The key assumptions in our calculations are (i) the coherent optical excitation should be in the continuous regime and thus, our calculations lie on the border between the classical and the coherent quantum regime (ii) the carriers dynamics are effectively described using the mean field approximation and their collective influence are incorporated into the *reduced dynamical equations* via the relaxation coefficients. We ignore the other many-body induced band renormalizations such as modification of the Fermi velocity due to electron-electron interactions [111]. (iii) Being limited to the photon energies below $\sim$ 2eV the Dirac cone approximation is valid and the excitonic effects are shown to be negligible [112]. (iv) Due to the smallness of the band gap induced by spin-orbit coupling, the dispersion properties of the charged carriers would barely deviate from the massless relativistic dynamics and are that term can be safely neglected. The above assumptions allow

us to proceed primarily within the single particle picture and the higher order many-body corrections will be phenomenologically included following a rigorous time domain analysis.

### 2.4.1 Equations of motion

We proceed from Eq. (2.16) which offers a gauge independent relation and thus we are at liberty to choose any kind of gauge making the mathematical structure simpler. Working in the sublattice (pseudospin) basis and making use of Eq. (2.9) and Eq. (2.17) gives

$$i\hbar\frac{\partial\hat{\rho}_{\mathbf{k}}}{\partial t} = \hbar v_F \mathbf{k}.[\hat{\vec{\sigma}}, \hat{\rho}_{\mathbf{k}}] + ie\mathbf{E}.\nabla_{\mathbf{k}}\hat{\rho}_{\mathbf{k}} \tag{2.21}$$

The $2 \times 2$ pseudospin density matrix $\hat{\rho}_{\mathbf{k}}$ can be expanded in terms of Pauli matrices

$$\hat{\rho}_{\mathbf{k}} = n_{\mathbf{k}}\hat{I} + \vec{m}_{\mathbf{k}} \cdot \hat{\vec{\sigma}} \tag{2.22}$$

On substituting Eq. (2.22) into Eq. (2.21), one obtains decoupled equations for *charge density* $n_{\mathbf{k}}$ and *pseudospin density* $\vec{m}_{\mathbf{k}}$ [42]

$$\frac{\partial n_{\mathbf{k}}}{\partial t} = \frac{e}{\hbar}\mathbf{E}.\nabla_{\mathbf{k}} n_{\mathbf{k}} \tag{2.23}$$

$$\frac{\partial \vec{m}_{\mathbf{k}}}{\partial t} = 2v_F\left(\mathbf{k} \times \vec{m}_{\mathbf{k}}\right) + \frac{e}{\hbar}\mathbf{E}.\nabla_{\mathbf{k}}\vec{m}_{\mathbf{k}} \tag{2.24}$$

The right hand side of Eq. (2.24) is analogous to spin procession in a magnetic field. The same can be set for the pseudospin in the *pseudo-magnetic field* acting in the reciprocal space [42]. This equation encodes a wealth of information about the optical response of graphene including linear and nonlinear response in noninteracting regime. Owing to the linear dispersion relation around the Dirac points, current operator has only paramagnetic component

$$\hat{\vec{\mathcal{J}}}_{\mathbf{k}} = -\frac{e}{\hbar}\frac{\partial\hat{\mathcal{H}}_{\mathbf{k}}}{\partial\mathbf{k}} = -ev_F\hat{\vec{\sigma}} \tag{2.25}$$

and the current density becomes

$$\mathbf{J} = \langle\hat{\vec{\mathcal{J}}}_{\mathbf{k}}\rangle = \mathrm{Tr}\left(\hat{\vec{\mathcal{J}}}_{\mathbf{k}}\hat{\rho}_{\mathbf{k}}\right) = -2ev_F\left(\hat{x}\hat{x} + \hat{y}\hat{y}\right) \cdot \sum_{\mathbf{k}}\vec{m}_{\mathbf{k}} \tag{2.26}$$

Having derived the equations of motion in the sublattice basis, now, we can switch to the energy diagonal basis. To avoid confusion, we use "$\sim$" to denote the matrix representation

of the operators in the valence and conduction basis. In the energy diagonal basis $\begin{pmatrix}1 & 0\end{pmatrix}^T$ and $\begin{pmatrix}0 & 1\end{pmatrix}^T$, stand for the upper and the lower energy levels respectively. In the energy diagonal basis the density matrix and the current operator become:

$$\tilde{\rho}_{\mathbf{k}} = \hat{I} n_{\mathbf{k}} + \vec{m}_{\mathbf{k}} \cdot \left( \hat{\mathbf{k}} \sigma_z + \hat{\varphi}_{\mathbf{k}} \sigma_y - \hat{\mathbf{z}} \sigma_x \right) \tag{2.27}$$

$$\tilde{\vec{\mathcal{J}}}_{\mathbf{k}} = - ev_F \left( \hat{\mathbf{k}} \sigma_z + \hat{\varphi}_{\mathbf{k}} \sigma_y \right) \tag{2.28}$$

Where $\hat{\mathbf{k}}$ and $\hat{\varphi}_{\mathbf{k}}$ are shown in Fig. 2.1(c). In the thermal equilibrium, before switching on the incident field, the density distribution obeys Fermi statistics

$$\langle \hat{\xi}^\dagger_{\mathbf{k}c} \hat{\xi}_{\mathbf{k}c} \rangle_0 = f(\mathcal{E}(\mathbf{k})) \quad , \quad \langle \hat{\xi}^\dagger_{\mathbf{k}v} \hat{\xi}_{\mathbf{k}v} \rangle_0 = f(-\mathcal{E}(\mathbf{k})) \tag{2.29}$$

Where subscript 0 denotes equilibrium state and $\mathcal{E}(\mathbf{k}) = \hbar v_f k$ is the upper energy level. The distribution $f(E)$ is the Fermi distribution function

$$f(E) = \frac{1}{1 + \exp\left(\frac{E-\mu}{K_B T}\right)}$$

where $\mu$ and $T$ are, respectively, the chemical potential associated with the fermi energy level $E_f$ and the temperature.

### 2.4.2 Dynamics of Population Difference and Polarization

In the presence of electromagnetic field, the current operator acquires a finite expectation value. The particle current, can be divided into two distinct parts. The first part is the current resulting from disturbing the distribution of the charged carriers residing on the upper and lower energy levels and the second contribution is due to interference between them. The former is intraband and the latter is the interband current. Following this statement, it will be shown that the optical response of a general two level system depends on the population difference $\mathcal{N}(\mathbf{k}, t)$ and polarization $\mathcal{P}(\mathbf{k}, t)$

$$\mathcal{N}(\mathbf{k}, t) = \langle \hat{\xi}^\dagger_{\mathbf{k}c} \hat{\xi}_{\mathbf{k}c} \rangle - \langle \hat{\xi}^\dagger_{\mathbf{k}v} \hat{\xi}_{\mathbf{k}v} \rangle = 2\hat{\mathbf{k}} \cdot \vec{m} \tag{2.30}$$

$$\mathcal{P}(\mathbf{k}, t) = \langle \hat{\xi}^\dagger_{\mathbf{k}v} \hat{\xi}_{\mathbf{k}c} \rangle = -\hat{\mathbf{z}} \cdot \vec{m} + i\hat{\varphi}_{\mathbf{k}} \cdot \vec{m} \tag{2.31}$$

Taking $\mathcal{N}$ and $\mathcal{P}$ as dynamical variables and using Eq. (2.24), we obtain the equations of motion for the population difference and the polarization.

$$\begin{cases} \dfrac{\partial \mathcal{N}(\mathbf{k},t)}{\partial t} - \frac{e}{\hbar}\mathbf{E}\cdot\nabla_{\mathbf{k}}\mathcal{N}(\mathbf{k},t) = -2\Phi(\mathbf{k},t)\mathrm{Im}\left\{\mathcal{P}(\mathbf{k},t)\right\} \\ \dfrac{\partial \mathcal{P}(\mathbf{k},t)}{\partial t} - \frac{e}{\hbar}\mathbf{E}\cdot\nabla_{\mathbf{k}}\mathcal{P}(\mathbf{k},t) = i\varpi_{\mathbf{k}}\mathcal{P}(\mathbf{k},t) + \frac{i}{2}\Phi(\mathbf{k},t)\mathcal{N}(\mathbf{k},t) \end{cases} \tag{2.32}$$

where $\Phi(\mathbf{k},t)$ is basically the matrix element of the external potential between the upper and lower energy levels for the given Bloch momentum $\mathbf{k}$ describing direct optical transition, since the momentum of the light is assumed to be negligibly small.

$$\Phi(\mathbf{k},t) = \frac{e\mathbf{E}\cdot\hat{\varphi}_{\mathbf{k}}}{\hbar k} \tag{2.33}$$

where the unit vector $\hat{\varphi}_{\mathbf{k}}$ is defined as $\hat{\varphi}_{\mathbf{k}} \triangleq \hat{z}\times\mathbf{k}/k$. The frequency $\hbar\varpi_{\mathbf{k}} = 2\mathcal{E}_{\mathbf{k}}$ is the energy difference between the upper and lower energy levels. The coupled equations given in (2.32) are called semiconductor Bloch equations (SBEs) for graphene. These equations must be solved simultaneously, subject to the initial condition imposed by the Fermi-Dirac distribution before turning on the field.

$$\begin{aligned} &\mathcal{N}(\mathbf{k},-\infty) = \mathcal{N}_{\mathbf{k}}^{eq} = f(\mathcal{E}(\mathbf{k})) - f(-\mathcal{E}(\mathbf{k})) \\ &\mathcal{P}(\mathbf{k},-\infty) = 0 \end{aligned}$$

The left side of the SBEs are essentially similar to the semiclassical Boltzman's transport equation. This part of dynamics is responsible for intraband transitions for a pure graphene, neglecting the effect of collisions and imperfections. A simple way of incorporating the effect of collision into the theory is to use a complex frequency in the spectral domain. The right side of SBEs appear to resemble the problem of two level atomic transition in the presence of an applied electric field. However, the dipole that causes transition has been replaced by $\Phi(\mathbf{k},t)$ in the reciprocal space. The chiral nature of the charged carriers leaves its fingerprint on the appearance of $1/k$ in the effective dipole expression. This singular behavior roots in $1/k$ dependence of $\overline{\overline{\boldsymbol{\zeta}}}_{\mathbf{k}}$ in the energy diagonal basis. The distinctive mathematical structure of the current operator in graphene and other Dirac materials can also reveal the fundamental root of this singularity. In contrast to ordinary semiconductors that in the absence of disorder, the current operator should be fairly well stationary in the energy eigenstates, for the Dirac fermions current operator does not commute with the Hamiltonian. This effect leads to *Zitterbewegung* and pseudodiffusion transport in graphene [113]. It is straightforward to show that the interband coupling at

the wavenumber $\mathbf{k}$ is $\hat{\mathbf{r}}_{cv} \approx \frac{i\hbar}{ev_F}\vec{\mathcal{J}}_{cv}(\mathbf{k})/[\mathcal{E}_c(\mathbf{k}) - \mathcal{E}_v(\mathbf{k})]$. Since the current operator only depends on the angular variables in a typical Dirac material (See Eq. (2.28) for instance), its off-diagonal components are strictly nonzero. As a direct consequence of this exclusive property of the massless Dirac quasiparticles, the interband part of the position operator carries a first order singularity at the accidental degeneracy point. As discussed earlier, this singularity would pose major consequences on the optical response of graphene and other Dirac type materials.

## 2.5 Perturbative Solution of SBEs

As discussed, the SBEs in their original form describe the quasiclassical transport and interband excitation problems simultaneously. To convert the dynamical equations into a more convenient form, we proceed to decouple the transport and interband evolutions. It is worth noting that for a moderate applied field strength, the time evolution due to this moving frame can be considered as an adiabatic evolution in comparison to the interband one. Following this adiabatic argument, the combined intraband and interband dynamics can be split, by introducing a moving frame in the reciprocal space whose movement is governed by the Boltzmann transport equation [71]. The pure classical part of the dynamics drives the distribution function along a trajectory determined by the direction of the electric field. This motion is accompanied by inelastic scattering as well as coulombic interactions among the induced charges. A phenomenological treatment of the overall effect requires invoking an extrinsic fitting factor $\Gamma$ which depends on the quality of the sample. The main disadvantage of this method is, of course, certain lack of rigour, the method is, however less laborious. The time-momentum coordinate in the moving frame is designed by $\{\tau, \mathbf{k}'\}$. The primed frame is then related to original frame by $\{\tau, \mathbf{k}'\} = \{t, \mathbf{k} - \Delta\mathbf{k}(t)\}$ where $\Delta\mathbf{k}$ obeys

$$\frac{\partial \Delta\mathbf{k}}{\partial t} + \Gamma\Delta\mathbf{k} = -\frac{e}{\hbar}\mathbf{E}(t) \tag{2.34}$$

Concurrently, the system evolves by pure interband dynamics as described by the equations resembling the optical Bloch equations for a generic two level problem [32]

$$\frac{\partial \mathcal{N}(\mathbf{k}', \tau)}{\partial \tau} = -\gamma^{(1)}_{\mathbf{k}'}(\mathcal{N}(\mathbf{k}', \tau) - \mathcal{N}^{eq}_{\mathbf{k}'}) - 2\Phi(\mathbf{k}', \tau)\mathrm{Im}\left\{\mathcal{P}(\mathbf{k}', \tau)\right\} \tag{2.35a}$$

$$\frac{\partial \mathcal{P}(\mathbf{k}', \tau)}{\partial \tau} = -\gamma^{(2)}_{\mathbf{k}'}\mathcal{P}(\mathbf{k}', \tau) + i\varpi_{\mathbf{k}'}\mathcal{P}(\mathbf{k}', \tau) + \frac{i}{2}\Phi(\mathbf{k}', \tau)\mathcal{N}(\mathbf{k}', \tau) \tag{2.35b}$$

As remarked ealier, the many-body effects such as electron-electron and electron-phonon interactions are rigorously analyzed within a separate many body theory, detailed in Ref. [114], and their collective influence on the optical response are phenomenologically incorporated into the dynamical equations via the $k$-dependent relaxation coefficients $\gamma_{\mathbf{k}}^{(1)}$ and $\gamma_{\mathbf{k}}^{(2)}$. It can be shown that this approach is accurate enough for the steady state (frequency domain) analysis of the linear and nonlinear optical response of graphene. The methodology is concisely discussed in Appendix B. In compliance with the standard notation of Bloch equations, we introduce $w_{\mathbf{k}}$, $u_{\mathbf{k}}$, $v_{\mathbf{k}}$ as

$$w_{\mathbf{k}'}(t) \triangleq \mathcal{N}(\mathbf{k}', \tau) \tag{2.36a}$$

$$u_{\mathbf{k}'}(t) \triangleq +2\mathrm{Re}\{\mathcal{P}(\mathbf{k}', \tau)\} \tag{2.36b}$$

$$v_{\mathbf{k}'}(t) \triangleq -2\mathrm{Im}\{\mathcal{P}(\mathbf{k}', \tau)\} \tag{2.36c}$$

$w_{\mathbf{k}}$ is population inversion in the moving frame. In Eqs. (2.36b) and (2.36c), the factor of two and the minus sign are used to comply with convention. The functions $\xi_{\mathbf{k}} \triangleq \Phi(\mathbf{k}', \tau)$ and $\omega_{\mathbf{k}} \triangleq \varpi'_{\mathbf{k}}$ are also defined for mathematical convenience and they are the analytical functions of the exciting field. The function $\xi_{\mathbf{k}}$ is the equivalent dipole in the moving frame. This dipole explicitly depends on the exciting field and higher order nonlinear terms also exist due to motion of the primed frame. In adiabatic approximation the dynamical equations (not the excitations) are not directly affected by the moving frame and therefore the time variations of the relxation coefficients as well as $\omega_{\mathbf{k}}$ due to the motion of the frame can be neglected as long as the pump wave intensity is not so large that multiphoton excitations take place.

The coupled Bloch equations can be converted to the well-known optical Bloch equations in the two-level approximation [32]. From now on, we drop the prime in $uvw$-coordinate system.

$$\dot{w}_{\mathbf{k}} = -\gamma_{\mathbf{k}}^{(1)}(w_{\mathbf{k}} - w_{\mathbf{k}}^{eq}) + \xi_{\mathbf{k}} v_{\mathbf{k}} \tag{2.37a}$$

$$\dot{u}_{\mathbf{k}} = \omega_{\mathbf{k}} v_{\mathbf{k}} - \gamma_{\mathbf{k}}^{(2)} u_{\mathbf{k}} \tag{2.37b}$$

$$\dot{v}_{\mathbf{k}} = -\omega_{\mathbf{k}} u_{\mathbf{k}} - \gamma_{\mathbf{k}}^{(2)} v_{\mathbf{k}} - \xi_{\mathbf{k}} w_{\mathbf{k}} \tag{2.37c}$$

where 'dot' denotes time derivative. The function $w_{\mathbf{k}}^{eq}$ is the population difference at equilibrium i.e. $w_{\mathbf{k}}^{eq} = \mathcal{N}_{\mathbf{k}}^{eq}$. For a weak pump field, the inversion $w_{\mathbf{k}}$ tends to relax to $w_{\mathbf{k}}^{eq}$. The coherent terms, on the other hand, are the oscillatory functions of the field. To proceed further, the current response in the reciprocal space must be identified. According to Eq. (2.27) together with Eq. (2.28) the induced current is

$$\mathbf{J} = -2ev_F \sum_{\mathbf{k}} (\hat{\mathbf{k}}\hat{\mathbf{k}} + \hat{\varphi}_{\mathbf{k}}\hat{\varphi}_{\mathbf{k}}) \cdot \vec{m}_{\mathbf{k}} = ev_F \sum_{\mathbf{k}} \left[ -w_{\mathbf{k}-\Delta\mathbf{k}}\hat{\mathbf{k}} + v_{\mathbf{k}-\Delta\mathbf{k}}\hat{\varphi}_{\mathbf{k}} \right] \tag{2.38}$$

Therefore the equation of motion describing the time evolution of $v_{\mathbf{k}}$ provides enough information to model the interband response of graphene. Neglecting the time variations of $\omega_{\mathbf{k}}$ in the adiabatic approximation:

$$\ddot{v}_{\mathbf{k}} + 2\gamma_2 \dot{v}_{\mathbf{k}} + \left(\omega_{\mathbf{k}}^2 + \gamma_2^2\right) v_{\mathbf{k}} = -\gamma_2 \xi_{\mathbf{k}} w_{\mathbf{k}} - \dot{\xi}_{\mathbf{k}} w_{\mathbf{k}} - \xi_{\mathbf{k}} \dot{w}_{\mathbf{k}} \tag{2.39}$$

Since $\omega_{\mathbf{k}}^2$ is much larger than $\gamma_2^2$ , we can drop $\gamma_2^2 v_{\mathbf{k}}$ to obtain the result:

$$\ddot{v}_{\mathbf{k}} + 2\gamma_2 \dot{v}_{\mathbf{k}} + \omega_{\mathbf{k}}^2 v_{\mathbf{k}} = -\gamma_2 \xi_{\mathbf{k}} w_{\mathbf{k}} - \dot{\xi}_{\mathbf{k}} w_{\mathbf{k}} - \xi_{\mathbf{k}} \dot{w}_{\mathbf{k}} \tag{2.40}$$

Eq. (2.40) describes a driven damped harmonic oscillator problem. The master equation (2.40) in conjunction with Eq. (2.37a) describe all linear and nonlinear properties of graphene. The origin of the nonlinear interband response in the moving frame lies in the fact that the coupling to the optical field depends parametrically on the inversion $w_{\mathbf{k}}$. Inversion is driven by the field stength $\xi_{\mathbf{k}}$ as described by Eq. (2.37a) which leads to a pure interband nonlinearity. This set of equations can be solved iteratively. Expanding $v_{\mathbf{k}}$ and $w_{\mathbf{k}}$ into the powers of the exciting field, i.e. $\xi_{\mathbf{k}}$, gives a infinite series that contains the odd powers for $v_{\mathbf{k}}$ and even powers of the field for $w_{\mathbf{k}}$.

$$w_{\mathbf{k}} = w_{\mathbf{k}}^{eq} + \sum_{n=1}^{\infty} W_{\mathbf{k}}^{(2n)} \xi_{\mathbf{k}}^{2n} \tag{2.41a}$$

$$v_{\mathbf{k}} = \sum_{n=1}^{\infty} V_{\mathbf{k}}^{(2n-1)} \xi_{\mathbf{k}}^{2n-1} \tag{2.41b}$$

From now on, the $n$'th order expansion terms $w_{\mathbf{k}}^{(n)}$ and $v_{\mathbf{k}}^{(n)}$ are defined via

$$w_{\mathbf{k}}^{(n)} = W_{\mathbf{k}}^{(n)} \xi_{\mathbf{k}}^{n} \quad , \quad v_{\mathbf{k}}^{(n)} = V_{\mathbf{k}}^{(n)} \xi_{\mathbf{k}}^{n}$$

The iterative procedure can be conveniently carried out defineing the opeartors $\boldsymbol{\mathcal{V}}_{\mathbf{k}}$ and $\boldsymbol{\mathcal{W}}_{\mathbf{k}}$.

$$\boldsymbol{\mathcal{V}}_{\mathbf{k}}(\omega) \triangleq \frac{\gamma_{\mathbf{k}}^{(2)} + i\omega}{\omega^2 - 2i\gamma_{\mathbf{k}}^{(2)}\omega - \varpi_{\mathbf{k}}^2} \frac{e}{\hbar k} \hat{\varphi}_{\mathbf{k}} \tag{2.42a}$$

$$\boldsymbol{\mathcal{W}}_{\mathbf{k}}(\omega) \triangleq \frac{1}{i\omega + \gamma_{\mathbf{k}}^{(1)}} \frac{e}{\hbar k} \hat{\varphi}_{\mathbf{k}} \tag{2.42b}$$

In addition to the pure interband multiphoton process described above, a part of nonlinearity originates from the quasiclassical transport or intraband transitions. As will be

clarified further in section 2.5.2, the frequency mixing effects in graphene arise from the pure intraband, pure interband and interband-intraband transitions. The pure intraband response occurs just because of the change in the the population difference. Using (2.38), the intraband contribution of the current is

$$\mathbf{J}_{intra} = -ev_F \sum_{\mathbf{k}} w^{eq}_{\mathbf{k}-\Delta\mathbf{k}} \hat{\mathbf{k}} \tag{2.43}$$

then, the $n$'th order nonlinearity due to *pure intraband process* can be obtained using Taylor expansion:

$$\mathbf{J}^{(n)}_{intra} = (-1)^{n+1} \frac{ev_F}{n!} \sum_{\mathbf{k}} \hat{\mathbf{k}} \left[\Delta\mathbf{k} \cdot \nabla_{\mathbf{k}}\right]^n \mathcal{N}^{eq}_{\mathbf{k}} \tag{2.44}$$

For the sake of mathematical convenience the derivative operator is represented as

$$\hat{\boldsymbol{\mathcal{D}}}_{\mathbf{k}}(\omega) \triangleq \frac{1}{i\omega + \Gamma} \frac{e}{\hbar} \nabla_{\mathbf{k}} \tag{2.45}$$

where the Drude-like coefficient $1/(i\omega + \Gamma)$ is obtained from equation (2.34). An intuitive symmetry argument shows that in graphene as a centrosymmetric crystal, even orders of nonlinearity do not exist. In the subceeding subsections the derivation of linear and third order conductivity of graphene is discussed.

### 2.5.1 Linear optical response of graphene

Eq. (2.44) for $n = 1$ gives the intraband conductivity tensor in the k-space

$$\overline{\overline{\sigma}}^{(1)}_{intra}(\mathbf{k}, \omega_p) = -ev_F \hat{\mathbf{k}} \hat{\boldsymbol{\mathcal{D}}}_{\mathbf{k}}(\omega_p) \mathcal{N}^{eq}_{\mathbf{k}} \tag{2.46}$$

where we have assumed that the electric field is $\mathbf{E}(t) = \widetilde{\mathbf{E}}_p \exp(i\omega_p t) + c.c$ and $\overline{\overline{\sigma}}^{(1)}_{intra}(\mathbf{k}, \omega_p)$ is defined via

$$\mathbf{J}_{\mathbf{k}} = \overline{\overline{\sigma}}^{(1)}_{intra}(\mathbf{k}, \omega_p) \cdot \mathbf{E}$$

Performing the integration over the reciprocal space, the off-diagonal terms vanish, we arrive at

$$\sigma^{(1)}_{intra}(\omega_p) = \frac{g_s g_v}{4\pi} \frac{e^2}{\hbar^2} \frac{1}{(i\omega_p + \Gamma)} \int_0^{+\infty} \mathrm{d}\mathcal{E}\mathcal{E} \left[\frac{\partial f(\mathcal{E})}{\partial \mathcal{E}} - \frac{\partial f(-\mathcal{E})}{\partial \mathcal{E}}\right] \tag{2.47}$$

where $g_s$ and $g_v$ are spin and valley degeneracy factors respectively. This equation can be simplified to a close form expression for the linear intraband conductivity

$$\sigma^{(1)}_{intra}(\omega_p) = \frac{e^2}{\hbar} \frac{g_s g_v}{4\pi} \frac{k_B T}{\hbar(i\omega_p + \Gamma)} \left[\frac{\mu}{k_B T} + 2\ln\left(1 + e^{-\mu/K_B T}\right)\right] \tag{2.48}$$

The interband linear optical response of graphene can be obtained using the master equation (2.40). Linear optical response is a single photon process and unlike higher order terms it can be obtained independently for interband and intraband contributions. The first order solution of the Eq. (2.40) can be derived by replacing $w_{\mathbf{k}}$ and $\dot{w}_{\mathbf{k}}$ with $w_{\mathbf{k}}^{eq}$ and 0 respectively

$$\overline{\overline{\sigma}}_{inter}(\mathbf{k},\omega_p) = ev_F\hat{\varphi}_{\mathbf{k}}\boldsymbol{\mathcal{V}}_{\mathbf{k}}(\omega_p)\mathcal{N}_{\mathbf{k}}^{eq} \tag{2.49}$$

Integrating over the reciprocal space and including the density of states gives

$$\sigma_{inter}^{(1)}(\omega_p) = \frac{e^2}{\hbar}\frac{g_s g_v}{4\pi}\int_0^{+\infty} \mathrm{d}\mathcal{E}\frac{(\gamma_2 + i\omega_p)}{\omega_p^2 - 2i\gamma_2\omega_p - \varpi_{\mathbf{k}}^2}\left[f(\mathcal{E}) - f(-\mathcal{E})\right] \tag{2.50}$$

Eqs. (2.48) and (2.50) are identical to the results obtained from linear response theory and Kubo formulation [82].

### 2.5.2 Third order frequency mixing in graphene

Graphene as a centrosymmetric crystal does not exhibit second order nonlinearity and therefore the first nonlinear term is the third order one. In fact, to induce an optically biased second order response, translation symmetry must be broken. From what has been discussed so far, we know that the $\varphi_{\mathbf{k}}$ dependence of the $n$'th order optical conductivity tensor in the reciprocal space, i.e. $\overline{\overline{\sigma}}_{\mathbf{k}}^{(n)}$, appears as $\overline{\overline{T}}_n(\varphi_{\mathbf{k}}) = \hat{\alpha}_1\hat{\alpha}_2\cdots\hat{\alpha}_{n+1}$ where $\hat{\alpha}_i$ can be either $\hat{\mathbf{k}}$ or $\hat{\varphi}_{\mathbf{k}}$. It is straightforward to show that $\int_0^{2\pi}\overline{\overline{T}}_n(\varphi_{\mathbf{k}})\mathrm{d}\varphi_{\mathbf{k}}$ vanishes when $n$ is an even integer. Throughout this section we assume that three complex fields with a time dependence of $e^{i\omega_p t}$, $e^{i\omega_q t}$ and $e^{i\omega_r t}$ are mixing through the third-order conductivity of graphene. As mentioned earlier, the third-order optical response can be interpreted as a three-photon process and different terms contribute to the third-order conductivity tensor namelya pure intraband term,a pure interband term and the combination of the both. The distinct photon processes contributing to the third-order optics of graphene are schematically shown in Fig. 2.2. The intraband dynamics cause the quasiparticles to travel along the trajectory determined by the direction of the electric field at the graphene plane. The quasiclassical Boltzman-like dynamics are schematically pictured by displacement of the entire distribution of the quasiparticles over the reciprocal space. The interband contributions are also shown by the two level transition of the quasiparticles predominantly around the zero detuning region. The adopted mathematical structure would allow us to find the conductivity tensors associated with the six processes shown in Fig. 2.2.

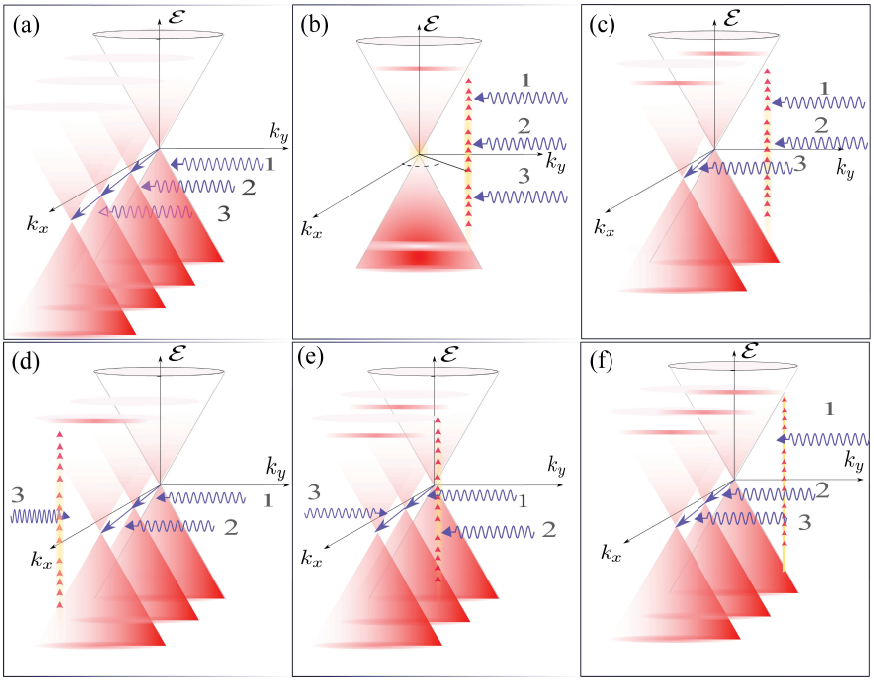


Figure 2.2: Schematic representation of different three-photon processes contributing to the third-order nonlinear optics of graphene. The intraband type of dynamics are displayed by displacement of the distribution and the interband dynamics are shown by two-level transitions. (a) Pure intraband (b) Pure interband (c) Interband-Interband-Intraband (d) Intraband-Intraband-Interband (e) Intraband-Interband-Intraband (f) Interband-Intraband-Intraband.

### Pure intraband third-order nonlinearity

The pure intraband contribution is fundamentally part of the third-order nonlinearity which occurs exclusively due to the Boltzman-like transport. The third-order intraband prcoess is schematically displayed in Fig. 2.2a. Equation (2.44) determines the nonlinear contribution of the third-order intraband evolution as

$$\overline{\overline{\mathcal{I}}}^{(3)}_{\mathbf{k},1}(\omega_p,\omega_q,\omega_r) = -ev_F\mathcal{P}_I\left\{\ \hat{\mathbf{k}}\hat{\boldsymbol{\mathcal{D}}}_{\mathbf{k}}(\omega_r)\hat{\boldsymbol{\mathcal{D}}}_{\mathbf{k}}(\omega_q)\hat{\boldsymbol{\mathcal{D}}}_{\mathbf{k}}(\omega_p)\mathcal{N}^{eq}_{\mathbf{k}}\ \right\} \tag{2.51}$$

Where the normalized gradient operator $\hat{\boldsymbol{\mathcal{D}}}_{\mathbf{k}}$ was introduced in Eq.(2.45). The subscript '1' is used to identify the intraband contribution and the superscript '(3)' refers to the third-order effect. Here we have made use of the intrinsic permutation operator $\mathcal{P}_I$; all possible permutations of the input frequencies $\omega_p$, $\omega_q$ and $\omega_r$, should be summed over. The

overal intraband conductivity tensor is then obtained as

$$\overline{\overline{\sigma}}^{(3)}_{intra}(\omega_p,\omega_q,\omega_r)=\sum_{\mathbf{k}}\overline{\overline{\mathcal{I}}}^{(3)}_{\mathbf{k},1} \tag{2.52}$$

**Pure interband third-order nonlinearity**

Pure interband third-order nonlinearity can be obtained using the master equations (2.40) and (2.37a) in the moving frame. Power expansion of the inversion and the polarization in terms of the exciting field as Eqs. (2.41a) and (2.41b) gives $v^{(3)}_{\mathbf{k}}$. Assuming that the first photon $\omega_p$ provides time variation for $v^{(1)}_{\mathbf{k}}(\omega_p)$, the first nonzero oscillatory component of $w_{\mathbf{k}}$ as well as the third harmonic of $v^{(3)}_{\mathbf{k}}$ can be found from the following equations

$$\dot{w}^{(2)}_{\mathbf{k}}+\gamma_1 w^{(2)}_{\mathbf{k}} = \xi_{\mathbf{k}}(\omega_q)v^{(1)}_{\mathbf{k}}(\omega_p) \tag{2.53}$$

$$\ddot{v}^{(3)}_{\mathbf{k}}+2\gamma_2\dot{v}^{(3)}_{\mathbf{k}}+\omega^2_{\mathbf{k}}v^{(3)}_{\mathbf{k}} = -\gamma_2\xi_{\mathbf{k}}(\omega_r)w^{(2)}_{\mathbf{k}}-\dot{\xi}_{\mathbf{k}}(\omega_r)w^{(2)}_{\mathbf{k}}-\xi_{\mathbf{k}}(\omega_r)\dot{w}^{(2)}_{\mathbf{k}} \tag{2.54}$$

These equations can be solved simultaneously to find the contribution of the interband dynamics associated with Bloch index $\mathbf{k}$ to the third-order optical nonlinearity. Making use of the operators $\boldsymbol{\mathcal{V}}_{\mathbf{k}}$ and $\boldsymbol{\mathcal{W}}_{\mathbf{k}}$ allows a compact solution as

$$\overline{\overline{\mathcal{I}}}^{(3)}_{\mathbf{k},2}(\omega_p,\omega_q,\omega_r)=-ev_F\mathcal{P}_I\left\{\hat{\varphi}_{\mathbf{k}}\boldsymbol{\mathcal{V}}_{\mathbf{k}}(\omega_p+\omega_q+\omega_r)\boldsymbol{\mathcal{W}}_{\mathbf{k}}(\omega_p+\omega_q)\boldsymbol{\mathcal{V}}_{\mathbf{k}}(\omega_p)\mathcal{N}^{eq}_{\mathbf{k}}\right\} \tag{2.55}$$

Performing the integration in the reciprocal space and applying the permutation operator yields the final expression for the interband conductivity tensor. The interband conductivity tensor is then obtained as

$$\overline{\overline{\sigma}}^{(3)}_{inter}(\omega_p,\omega_q,\omega_r)=\sum_{\mathbf{k}}\overline{\overline{\mathcal{I}}}^{(3)}_{\mathbf{k},2} \tag{2.56}$$

where the summation goes over all quantum states. This term is obviously singular at the origin.

**Interband-intraband third-order nonlinearity**

The master equations together with the notion of a moving frame lead to four possible combinations of the inter- and intraband dynamics shown in Fig. 2.2c-f.

- **Interband-Interband-Intraband:** According to Fig. 2.2c, the interband dynamics modify the population difference through a non-parametric transition. The third photon (which is actually the probing photon!) causes an intraband transition. The master equations (2.40) and (2.37a) yield the modified population accomplished via two subsequent photon processes.

$$\dot{w}_{\mathbf{k}}^{(2)} + \gamma_1 w_{\mathbf{k}}^{(2)} = \xi_{\mathbf{k}}(\omega_q) v_{\mathbf{k}}^{(1)}(\omega_p)$$

  The third process causes the modified population to move over the reciprocal space and creates an intraband current described by equation (2.43). The tensor associated with this process reads

$$\overline{\overline{\mathcal{I}}}_{\mathbf{k},3}^{(3)}(\omega_p, \omega_q, \omega_r) = -ev_F \mathcal{P}_I \left\{ \hat{\mathbf{k}} \hat{\boldsymbol{\mathcal{D}}}_{\mathbf{k}}(\omega_r) \boldsymbol{\mathcal{W}}_{\mathbf{k}}(\omega_p + \omega_q) \boldsymbol{\mathcal{V}}_{\mathbf{k}}(\omega_p) \mathcal{N}_{\mathbf{k}}^{eq} \right\} \tag{2.57}$$

- **Intraband-Intraband-Interband:** Following two subsequent intraband transitions at the frequencies of $\omega_p$ and $\omega_q$, the population difference oscillates at the sum frequency $\omega_p + \omega_q$. The third photon probes the graphene whose quasiparticles are oscillating over the reciprocal space and the current is induced due to interband transition. This process is sketched in Fig. 2.2d and mathematically is encoded by $\overline{\overline{\mathcal{I}}}_{\mathbf{k},4}^{(3)}$.

$$\overline{\overline{\mathcal{I}}}_{\mathbf{k},4}^{(3)}(\omega_p, \omega_q, \omega_r) = -ev_F \mathcal{P}_I \left\{ \hat{\varphi}_{\mathbf{k}} \boldsymbol{\mathcal{V}}_{\mathbf{k}}(\omega_p + \omega_q + \omega_r) \hat{\boldsymbol{\mathcal{D}}}_{\mathbf{k}}(\omega_q) \hat{\boldsymbol{\mathcal{D}}}_{\mathbf{k}}(\omega_p) \mathcal{N}_{\mathbf{k}}^{eq} \right\} \tag{2.58}$$

- **Intraband-Interband-Intraband:** Fig. 2.2e displays the ordering of the processes. Following an intraband transition, the population difference oscillates at frequency $\omega_p$. The second process is interband which creates a coherence (polarization) at the frequency of $\omega_p + \omega_q$. The induced polarization is driven by an additional intraband transition to create a current at the frequency of $\omega_p + \omega_q + \omega_r$. Although the last transition is intraband, the induced current is of interband nature and is modulated by the moving frame.

$$\overline{\overline{\mathcal{I}}}_{\mathbf{k},5}^{(3)}(\omega_p, \omega_q, \omega_r) = -ev_F \mathcal{P}_I \left\{ \hat{\varphi}_{\mathbf{k}} \hat{\boldsymbol{\mathcal{D}}}_{\mathbf{k}}(\omega_r) \boldsymbol{\mathcal{V}}_{\mathbf{k}}(\omega_p + \omega_q) \hat{\boldsymbol{\mathcal{D}}}_{\mathbf{k}}(\omega_p) \mathcal{N}_{\mathbf{k}}^{eq} \right\} \tag{2.59}$$

- **Interband-Intraband-Intraband:** An interband transition caused by the first photon creates the polarization oscillating at the frequency $\omega_p$. Due to the Boltzman-like transport, the induced polarization is modulated by two consecutive harmonics $\omega_q$

and $\omega_r$. The induced current has an interband nature and is shown in Fig. 2.2f. The overall dynamics are encoded by $\overline{\overline{\mathcal{I}}}^{(3)}_{\mathbf{k},6}$.

$$\overline{\overline{\mathcal{I}}}^{(3)}_{\mathbf{k},6}(\omega_p,\omega_q,\omega_r) = -ev_F\mathcal{P}_I\left\{\hat{\varphi}_{\mathbf{k}}\hat{\boldsymbol{\mathcal{D}}}_{\mathbf{k}}(\omega_r)\hat{\boldsymbol{\mathcal{D}}}_{\mathbf{k}}(\omega_q)\boldsymbol{\mathcal{V}}_{\mathbf{k}}(\omega_p)\mathcal{N}^{eq}_{\mathbf{k}}\right\} \tag{2.60}$$

The overal intraband-interband conductivity tensor is then obtained as

$$\overline{\overline{\sigma}}^{(3)}_{intra-inter}(\omega_p,\omega_q,\omega_r) = \sum_{l=3}^{6}\sum_{\mathbf{k}}\overline{\overline{\mathcal{I}}}^{(3)}_{\mathbf{k},l} \tag{2.61}$$

## 2.6 Spontaneous Optical Saturation of Graphene

As remarked earlier, the diverging field-induced interband coupling around the Dirac point is expected to significantly influence the optical response of graphene. Since the interband coupling is really pronounced around the degeneracy point, the intraband dynamics can be safely treated as independent in the vicinity of the degenercy point. As a result, graphene can be thought as an ensemble of two level systems over the reciprocal space with the effective dipole moment described by $\Phi(\mathbf{k},t)$. We expect that the two level systems will undergo ultra-fast Rabi oscillations which are dominantly damped by many body interactions including electron-electron and electron-phonon scatterings. The decay terms drive the two level systems labeled by Bloch index $\mathbf{k}$ into an equilibrium state after a time $1/\gamma^{(2)}_{\mathbf{k}}$. Since around the Dirac point the interband coupling is strong (equivalent to highly intense illumination), the effective field leaves the two-level systems in a statistical mixture of the ground and excited states with equal weight and absorption quenching takes place. We name the nearly zero population difference around the Dirac point caused even by an arbitrarily weak electromagnetic radiation as the *spontaneous saturation* effect. This interpretation leads to the proposal that the optics of graphene is essentially nonparametric and nonperturbative.

The saturation behavior discussed above can be best comprehended by capturing the steady state solution of the Bloch equations. In order to do so, we adopt steady state ansatz within the rotating frame approximation [115]. We define $\mathcal{N}(\mathbf{k},t) \approx \widetilde{\mathcal{N}}^{st}_{\mathbf{k}}$ and $\mathcal{P}(\mathbf{k},t) \approx \widetilde{\mathcal{P}}^{st}_{\mathbf{k}}e^{i\omega t}$ where the tilde $\sim$ designates the stationary part of the population difference and polarization with vanishing time derivatives. The steady state solution of the SBEs yields

the optically modified population difference and polarization

$$\widetilde{\mathcal{N}}_{\mathbf{k}}^{st}(I_0) = \mathcal{N}_{\mathbf{k}}^{eq} \frac{\gamma_{\mathbf{k}}^{(1)}}{\gamma_{\mathbf{k}}^{(1)} + \gamma_{\mathbf{k}}^{(2)} \left|\mathcal{L}_{\mathbf{k}}(\omega)\right|^2 \left|\widetilde{\Phi}_{\mathbf{k}}\right|^2} \tag{2.62a}$$

$$\widetilde{\mathcal{P}}_{\mathbf{k}}^{st}(I_0) = \frac{i}{2} \mathcal{L}_{\mathbf{k}}(\omega) \widetilde{\mathcal{N}}_{\mathbf{k}}^{st} \widetilde{\Phi}_{\mathbf{k}} \tag{2.62b}$$

where $\widetilde{\Phi}_{\mathbf{k}} = e\mathbf{E}_0.\hat{\varphi}_{\mathbf{k}}/\hbar k$ is the complex phasor associated with $\Phi(\mathbf{k}, t)$. Since the steady state solution depends on the field magnitude via $|\widetilde{\Phi}_{\mathbf{k}}|^2$ in the denominator of the Eq. (2.62a), the overall solution is function of the intensity $I_0 = 2\varepsilon_0 c \left|\mathbf{E}_0\right|^2$ ($c$ is the speed of light and $\varepsilon_0$ is the permitivity). The complex Lorentzian $\mathcal{L}_{\mathbf{k}}(\omega)$ is abbreviated as

$$\mathcal{L}_{\mathbf{k}}(\omega) \triangleq \frac{1}{\gamma_{\mathbf{k}}^{(2)} + i\Delta_{\mathbf{k}}} \tag{2.63}$$

Here $\Delta_{\mathbf{k}} = \omega - \varpi_{\mathbf{k}}$ denotes the detuning of the two level system at $\mathbf{k}$ with respect to the excitation. Equation (2.62a) decodes a wealth of information about saturation effects including the spontaneous saturation discussed above. Particularly, the regions of the k-space where the population $\mathcal{N}_{\mathbf{k}}$ cannot be Taylor expanded in terms of the powers of the field $\widetilde{\Phi}$, are the saturated regions. Non-validity of the geometric expansion implies that the perturbative expansion no longer be valid. This saturation behavior basically occurs in all two level systems at sufficiently high field intensities. However, due to the singularity of the interband coupling in graphene, there is always a region around the Dirac point where graphene is saturated. Following this argument, the saturation threshold $E_{\mathbf{k}}^{sat}$ can be obtained as a function of $\mathbf{k}$ and the relaxation coefficients as

$$eE_{\mathbf{k}}^{sat} = \hbar k \sqrt{\Delta_{\mathbf{k}}^2 \frac{\gamma_{\mathbf{k}}^{(1)}}{\gamma_{\mathbf{k}}^{(2)}} + \gamma_{\mathbf{k}}^{(1)} \gamma_{\mathbf{k}}^{(2)}} \tag{2.64}$$

For the given electric field amplitude $E_0$, at any region of the k-space where $E_0 > E_{\mathbf{k}}^{sat}$, the perturbative expansion is not valid and the population difference is significantly modified by the optical illumination. Obviously, at the Dirac point the saturation threshold is zero and hence graphene gets spontaneously saturated. Equation (2.64) identifies two independent mechanisms contributing in the saturation effects. Around the Dirac point the overall expression is dominated by the off-tuned term i.e. $eE_{\mathbf{k}}^{sat} \approx \hbar k \left|\Delta_{\mathbf{k}}\right| \sqrt{\gamma_{\mathbf{k}}^{(1)}/\gamma_{\mathbf{k}}^{(2)}}$. This term determines the saturation region at the origin. The second term, however, would lead to an ordinary saturation effect over the optical transition region where $\Delta_{\mathbf{k}} \sim 0$ which in turn yields $eE_{\mathbf{k}}^{sat} \approx \hbar k \sqrt{\gamma_{\mathbf{k}}^{(1)} \gamma_{\mathbf{k}}^{(2)}}$.

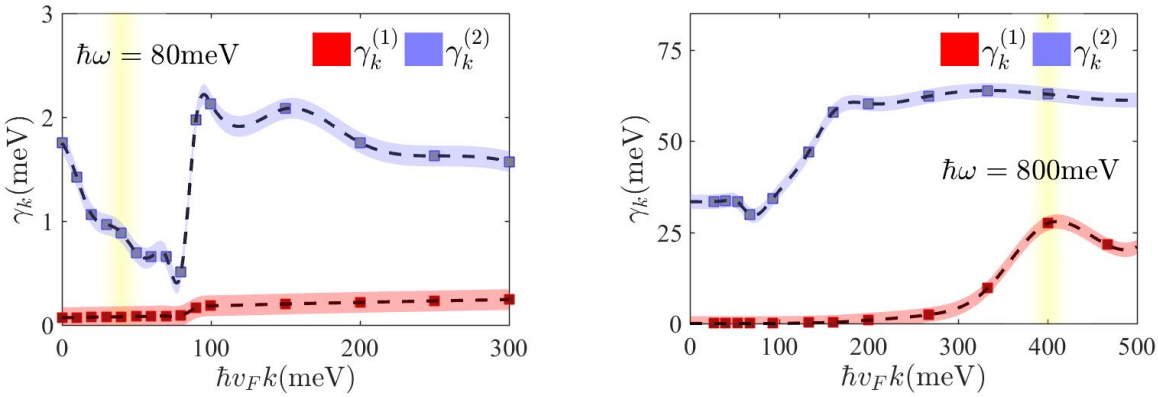


Figure 2.3: k-dependent relaxation coefficients $\gamma_{\mathbf{k}}^{(1)}$ and $\gamma_{\mathbf{k}}^{(2)}$ for an undoped graphene. The results are obtained from full many body calculations. Yellow shaded region shows the region with zero detuning (optical excitation is $\hbar\omega \sim 800$meV)

The saturation threshold strictly depends on the effective relaxation coefficients and therefore relaxation dynamics play a decisive role in saturation behavior. A full many-body calculation has been performed in order for extracting effective relaxation coefficients. We have employed the microscopic theory that encompasses carrier-carrier as well as carrier-phonon scattering channels and takes into account all relevant relaxation paths including interband and intraband and even inter-valley processes [114]. Both diagonal and off diagonal many-particle dephasings have been considered in our calculations. The full dynamics has been examined by a relatively long but sharp-edged pulse excitation. In order to extract the effective relaxation coefficients $\gamma_{\mathbf{k}}^{(1)}$ and $\gamma_{\mathbf{k}}^{(2)}$, the time decay of the population difference and polarization has been observed over time at different points in the k-space. Fig. 2.3 shows the results of our calculations. It is quite interesting that $\gamma_{\mathbf{k}}^{(1)}$ tends to be zero in the vicinity of the Dirac point which causes an even more pronounced saturation effect around the origin.

Having achieved all necessary ingredients , the peculiar saturation mechanism in graphene can be genuinely resolved by time domain analysis of the graphene Bloch equations. The finite difference time domain technique is employed to watch the temporal dynamics. The time steps are appropriately selected to assure numerical stability. Although the ultra-fast and transient response may not be accurately captured by the effective dynamics described by the coupled equations (2.35a) and (2.35b), since the steady state response is the only

matter of interest, analysis offers sufficiently reliable results. For the sake of comparison, the analysis has been performed for two distinct continuous excitations with the energy of $\hbar\omega = 80$meV (THz range) and $\hbar\omega = 800$meV (infrared) respectively. In both cases, the electric field is linearly polarized along $\hat{y}$ direction with the magnitude of $E_0 = 10^6$V/m. Graphene is assumed to be undoped (i.e. $\mu \approx 0$) and is initially held at room temperature. It can be shown that, in the steady state regime, the population difference contains even harmonics of excitation with a dominant non-oscillatory part. The polarization, in contrast, would be oscillatory with odd harmonics. The relative change in the stationary component of the population difference due to the optical excitation as well as the induced polarization oscillating at the first harmonics are illustrated in Fig. 2.4. To distill the steady state components, we perform Fourier analysis within a time window that the transient response has already died out. We have found perfect agreement between the results shown in Fig. 2.4 and Eqs. (2.62a)-(2.62b).

As expected, time-domain analysis also reveals the unconventional saturation region in graphene. Fig. 2.4 illustrates a well-pronounced modified population difference around the Dirac point due to the optical excitation. We observe that this effect is more conspicuous for low energy excitations; reduced detuning yields weaker saturation threshold. It is worth noting that for moderate field intensities (like this example), the completed saturated region might be small. The region of the reciprocal space where the self-coupling is significant, nevertheless, is considerably well extended in the vicinity of the Dirac point. This effect together with nonzero polarization induced aound the origin lead to an unconventional *Kerr like* nonlinearity in graphene. An exhaustive analysis of this effect will be presented in the next section.

To gain insight into the macroscopic impact of the spontaneous saturation effect, let us consider the example of nonlinear spectroscopy in which monolayer graphene is subjected to the simultaneous application of a pump and probe laser beam. The frequency of the pump and probe are $\omega_c$ and $\omega_p$, respectively, and the intensity of the pump laser is denoted by $I_c$. The intraband absorption profile of the probe field is obtained by plugging the steady state population difference $\mathcal{N}_{\mathbf{k}}^{st}(I_c)$ into the linear response theory. The corresponding intraband linear conductivity tensor in the presence of the pump $I_c$ reads

$$\overline{\overline{\Sigma}}_{intra}\Big|_{I_c}(\omega_p) \approx \frac{e^2 v_F g_s g_v D}{i\omega_p + \Gamma} \iint_{\mathrm{RBZ}} \mathrm{d}^2\mathbf{k}\hat{\mathbf{k}}\nabla_{\mathbf{k}}\widetilde{\mathcal{N}}_{\mathbf{k}}^{st}(I_c) \tag{2.65}$$

where $g_s$ and $g_v$ are the spin and valley degeneracy factors, respectively, and $D = 1/(2\pi)^2$ is the density of the states in the reciprocal space. The integral goes over the reduced reciprocal space where the Dirac dispersion is valid (RBZ abbreviates Reduced Brillouin Zone). A more rigorous treatment, would involve including additional contributions acounting

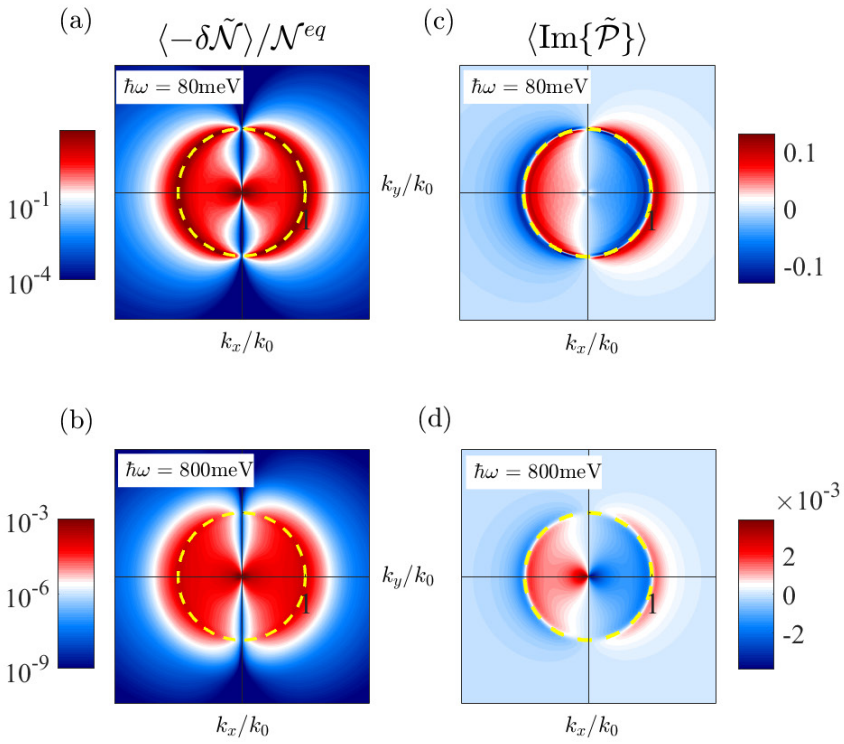


Figure 2.4: Contour plots of the time-resolved steady state population difference ($\delta\mathcal{N} = \mathcal{N}(\mathbf{k}, t) - \mathcal{N}^{eq}_{\mathbf{k}}$) and polarization of an undopted graphene for two distinct excitations, $\hbar\omega = 80\text{meV}, 800\text{meV}$. k-space is normalized to $k_0 = \omega/2v_F$. Yellow dotted lines display the optical excitation with zero interband detuning. For the both excitations the field amplitude is $\mathbf{E}_0 = 10^6\text{V/m}\hat{y}$.

for the nonlinear frequency mixing due to pure intraband process. However, the above formulation is adequately accurate for large enough pumpe frequencies. The interband conductivity consists of two contributions namely incoherent and coherent terms [116]. Similar to the intraband part, the incoherent contribution simply results from reduction of the population difference over the reciprocal space. The coherent term, however, enters due to population pulsation at the beat frequency $\omega_c - \omega_p$. It is argued that the coherent term involves interference between the pump and probe fields [116]. The population pulsation followed by absorption of a second photon from the pump field, mathematically acts as an additional *complex* contribution to the population difference denoted by $\delta\mathcal{N}^{puls}$. The

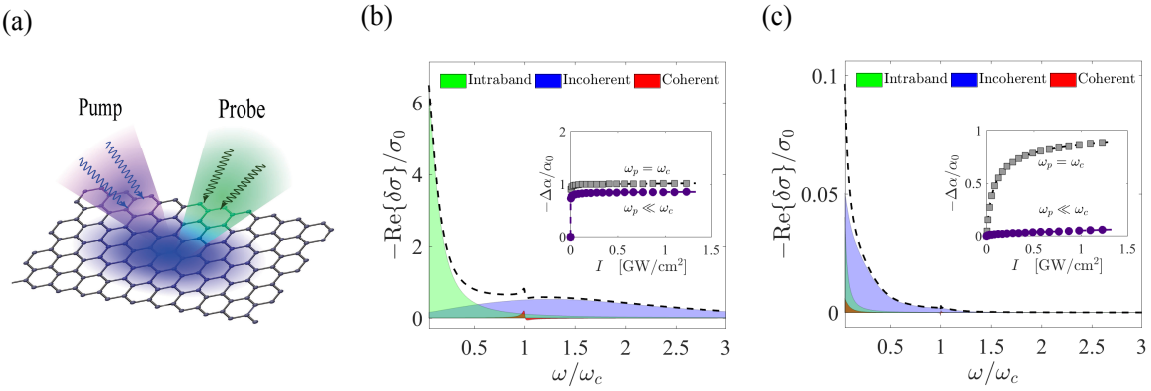


Figure 2.5: Change to the diagonal element of the conductivity at the probe frequency $\omega_p$ ($\delta\sigma(\omega_p)$) due to the presence of the pump field at the frequency of (a) $\hbar\omega_c = 80$meV and (b) $\hbar\omega_c = 800$meV . The conductivity is normalized to $\sigma_0 = e^2/4\hbar$. Variations of the absorption coefficient of graphene (normalized to its intrinsic value) versus the pump intensity for the two frequences of the pump field are shown in the insets of the figures.

overall pump induced interband conductivity tensor is

$$\begin{aligned}\overline{\overline{\Sigma}}_{inter}\Big|_{I_c}(\omega_p) &= -\frac{e^2}{\hbar}v_F g_s g_v D\iint_{\mathrm{RBZ}}\mathrm{d}^2\mathbf{k}\left\{\hat{\varphi}_{\mathbf{k}}\hat{\varphi}_{\mathbf{k}}\frac{1}{k}\mathcal{L}_{\mathbf{k}}(\omega_p)\left[\widetilde{\mathcal{N}}^{st}_{\mathbf{k}}(I_c)+\delta\mathcal{N}^{puls}_{\mathbf{k}}(I_c)\right]\right\}\\ &= \overline{\overline{\Sigma}}_{incoh}+\overline{\overline{\Sigma}}_{coh}\end{aligned} \tag{2.66}$$

where

$$\delta\mathcal{N}^{puls}_{\mathbf{k}}(I_c) = -\widetilde{\mathcal{N}}^{st}_{\mathbf{k}}(I_c)\frac{\left[\mathcal{L}_{\mathbf{k}}(\omega_p)+\mathcal{L}^*_{\mathbf{k}}(\omega_c)\right]\left|\widetilde{\Phi}^c_{\mathbf{k}}\right|^2}{2\gamma^{(1)}_{\mathbf{k}}-2i(\omega_c-\omega_p)+\left[\mathcal{L}_{\mathbf{k}}(\omega_p)+\mathcal{L}^*_{\mathbf{k}}(2\omega_c-\omega_p)\right]\left|\widetilde{\Phi}^c_{\mathbf{k}}\right|^2} \tag{2.67}$$

The validity of the theory requires that the coherence length of the pump laser be much larger than the wavelength of the probe field.

Following the previous example, Fig. 2.5 displays the relative change to the real part of the diagonal element of the overall conductivity tensor due to the pump fields described earlier. Given the absorption coefficient defined as the relative change in the intensity as light passes through monolayer graphene $\alpha = -\Delta I/I$, this coefficient is roughly calculated as $\alpha \approx \mathrm{Re}\{\sigma\}/4\varepsilon_0 c$. The relative change to the absorption coefficient for low frequency probing and probing at the same frequency of the pump field are shown in the insets of Figs. 2.5b and 2.5c. The low frequency modulation is caused by virtue of the spontaneous

saturation effect and is quite pronounced for low frequency pumping. It is quite interesting that sufficiently strong optical excitation can render a graphene monolayer quite transparent at low frequencies.

## 2.7 Semi-perturbative Nonlinear Optics of Graphene

In the previous section, it was argued that the topologically protected large interband coupling at the Dirac point gives rise to spontaneous optical saturation. Since that effect essentially occurs for even arbitrarily weak field intensities, the full machinery of the perturbation theory should fail to predict the optical response of graphene. Specifically, the nonlinear optical response needs to be treated carefully to account for the extreme nonlinear behavior of the quasiparticles in the vicinity of degeneracy points. One might legitimately argue that, according to Eq. (2.64), for moderately intense illuminations only the few number of quasiparticles belonging to the relatively small saturated region would undergo saturation and thereby its impact should be negligible. Although, the argument is valid for the linear part of the optical response, the nonlinear optics of graphene can be highly influenced by this phenomenon. Inside the saturated region, due to optically induced Pauli blocking, the Bloch quasiparticles basically stop interacting with light. However, as will be shown in the following, an extreme nonlinear optical interaction over the boundary of the saturated region takes place and it would leave its finger print as a finite contribution to the overall nonlinear optical response of graphene.

As detailed in section 2.5, the perturbative treatment of the optical response of graphene would lead to a nonresolvable singularity in its higher order nonlinear coefficients. We can now acknowledge that the singularity is the manifestation of the unconventional saturation effect and it can be removed by excluding the saturated states from the solution domain.

In spite of invalidity of the perturbation theory in the optics of graphene, derivation of the nonlinear coefficients is still favorable, particularly, for predicting the nonlinear frequency mixing effects when several frequency components coexist. Striving to obtain the nonlinear coefficients, we can safely remove the saturated region from the perturbative expansion. The saturated states would still influence the overal response by specifying the domain of integeration over the reciprocal space. This is the point where the extreme nonlinear process at the vicinity of the Dirac point and nonlinear response tie up.

Let us focus on the region of the k-space where perturbation analysis is still valid. It is argued in section 2.5.2 and references [71, 74, 75] that the nonlinear frequency mixing in graphene can be decomposed to the additive contributions namely pure interband , pure

intraband and interplay between them. Obviously the pure interband term is singular at the origin. Based on the above argument, the conductivity tensor associated with each contribution is then obtained as

$$\overline{\overline{\sigma}}_{l}^{(3)}(\omega_p,\omega_q,\omega_r) = g_s g_v D \iint_{|\mathbf{k}|>K_{sat}} \mathrm{d}^2\mathbf{k} \quad \overline{\overline{\mathcal{I}}}_{\mathbf{k},l}^{(3)}(\omega_p,\omega_q,\omega_r) \tag{2.68}$$

where $K_{sat}$ is the radius (with respect to the Dirac point) of the saturated region over the k-space and is obtained from Eq. (2.64)

$$\hbar v_F K_{sat} \approx \frac{1}{2}\hbar\omega - \sqrt{(\frac{1}{2}\hbar\omega)^2 - 2\hbar v_F e E_0 \sqrt{\frac{\gamma^{(2)}}{\gamma^{(1)}}}} \tag{2.69}$$

Here $\gamma^{(1)}$ and $\gamma^{(2)}$ are the phenomenological relaxation coefficients and $E_0$ is the magnitude of the largest electric field component (most often a pump field) participating in the nonlinear process and $\omega$ is its frequency. The above approximation holds as long as $\hbar\omega \gg \hbar v_F K_{sat}$ which is readily satisfied in most optical excitations. Since the integration domain and accordingly the nonlinear coefficients depend on the field magnitude, the solution is called *semi-perturbative*. However, as will be exemplified in the following, this dependence is small enough to think of the coefficients as the third order nonlinear conductivity tenors.

In order to gain insight into the intensity dependence of the nonlinear response coefficients obtained from the semi-perturbative approach as well as to examine equation (2.69), we compare the *Kerr-like* nonlinear response encoded by $\left|\sigma^{(3)}(\omega,\omega,-\omega)\right|$ with the results of nonperturbative solution of SBEs (detailed in Appendix C). The blue shaded regions display the nonpertubative solution and the black dotted curves are the results of semi-perturbative approach. First, owing to the spontaneous saturation effect, there is a noticeable field dependence of the Kerr-like response for lower Fermi energies. As the Fermi energy becomes larger, the optically induced Pauli blocking fades as the low energy Fermions are already Pauli blocked. There is perfect agreement between the two approaches. However, in the saturated states displayed by the red shaded regions, the semi-perturbation theory expectedly breaks down and it cannot follow the analytical solutions. It is worth pointing out that we have observed significant dependence of the results on $K_{sat}$ and therefore exact exclusion of the stuated region is required to achieve accurate results. The theoretical estimations for the different semi-perturbative nonlinear response coefficients including the third harmonic and Kerr coefficients will be deliberated in the next section.

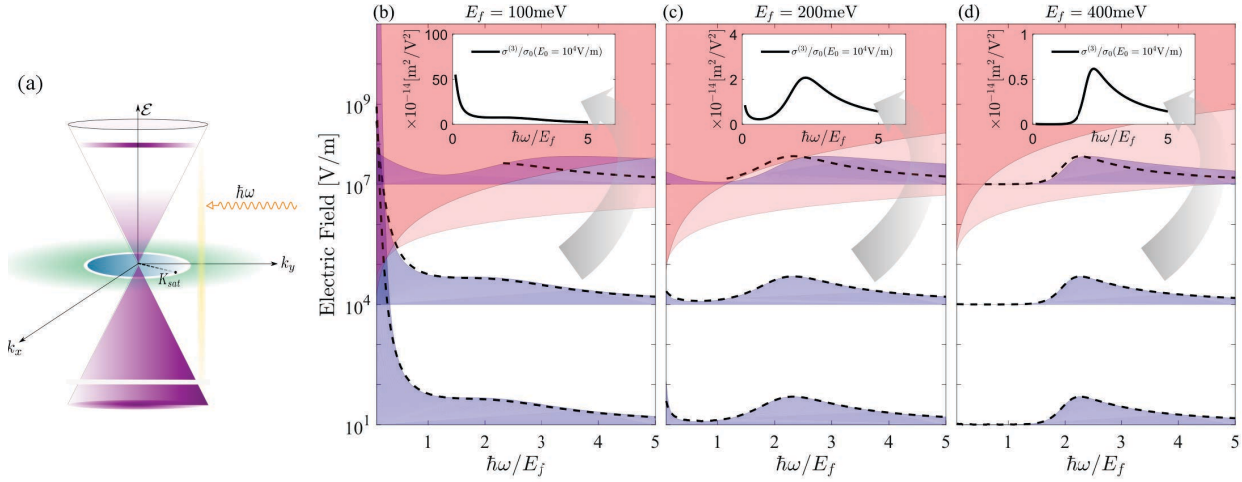


Figure 2.6: Kerr-type nonlineraity of graphene obtained based the analytical approach outlined in Appendix C (blue shaded regions) and semi-pertubative approach (i.e. $\sigma^{(3)}(\omega, \omega, -\omega)$, black dotted curves). The two distinctive red shaded regions are the saturation regions which are separately taking place due to 1. zero-detuning and 2. strong interband coupling in the vicinity of the Dirac points. Results for different fermi levels are displayed with different scales. Actual scales are presented in the insets.

## 2.8 Nonlinear Response Coefficients of Graphene

The nonlinear optical behavior of graphene has been experimentally investigated by several groups [39, 76, 77]. Four-wave mixing experiment [76] and Z-scan technique [77–79] have been among the most common methods to measure the nonlinear response of graphene. The results of the experiments confirm that graphene has an exceptionally high third-order susceptibility over a wide range of frequency. Depending on the measurement method and the sample quality, various research groups have reported different values for the bulk susceptibility and nonlinear refractive index of graphene. Despite the discrepancies between the different measurement results, the published experimental reports unanimously demonstrate that the nonlinear response of graphene is relatively strong [94]. The experimental characterization of the nonlinear optical response of graphene will be deliberated in the next section.

The theoretical predictions for the linear and nonlinear optical response of graphene are shown in Figs. 2.7 and 2.8. In our calculations, the unknown parameters are selected according to the experimental results. As is extensively discussed in Appendix B, the phe-

nomenological intraband scattering rate $\Gamma$ and two-level interband relaxation coefficients ($\gamma_1$ and $\gamma_2$) depend on the frequency, temperature and even quality of the sample. A full theoretical investigation of the possible origins of the relaxation coefficients is given in Refs. [114, 117, 118]. According to the experimental results reported in [86, 119], the relaxation coefficients are typically around tens of meV ($\Gamma, \gamma_{1,2} \sim 10$meV). To highlight the resonant features of the linear and nonlinear response, it is assumed that graphene is held at the temperature of $T \approx 0$K. It is also assumed that the Fermi energy level is around 200meV. The energy of the incoming photon(s) are normalized to the Fermi energy. According to the general conclusion made in the previous section, for such relatively high fermi energy level, the perturbation theory is fairly valid and the spontaneouss saturation effect can be neglected. This assumption allow us to retain the meaning of the nonlinear coefficient as usual.

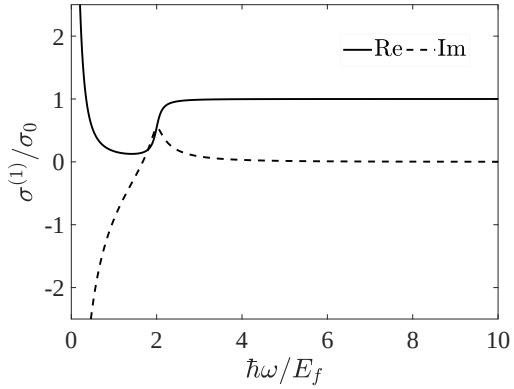


Figure 2.7: Linear optical conductivity of graphene for normally incident plane wave. The parameter $\sigma_0 = e^2/(4\hbar)$ is the universal optical conductivity.

The linear optical conductivity of graphene is shown in Fig. 2.7. It is observed that the optical absorption of graphene is universal and independent of the frequency for the photon energies of $\hbar\omega >\sim 2E_f$. The universal behavior of the optical conductivity in graphene can be explained by the two-dimensionality and the invariance of the condensed matter system [88, 120]. However, the dispersionless character of the absorption spectral is not topologically protected and even the inclusion of the higher order terms -such as triangular warping [42]- can deviate it from the universally flat response.

Fig. 2.8 shows the frequency dependence of the third order conductivity of graphene. To glean some insight into the dependence of the nonlinear coefficients on the phenomenological interband relaxation coefficients , the results are presented for a variety of the relaxation

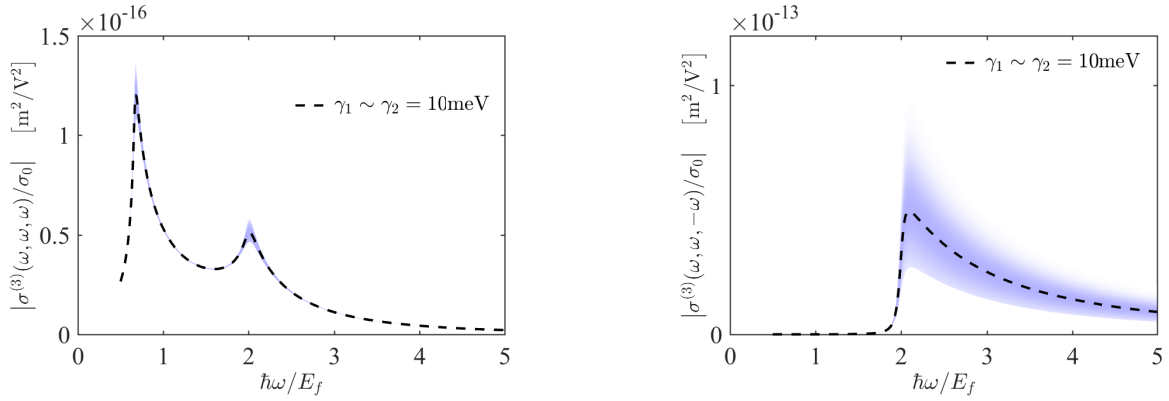


Figure 2.8: Third order conductivity of graphene normalized to $\sigma_0 = e^2/4\hbar$ (a) $\sigma^{(3)}_{xxxx}(\omega,\omega,\omega)$ and (b) $\sigma^{(3)}_{xxxx}(\omega,\omega,-\omega)$. Blue shaded regions describe the variations of the coefficients due to the uncertainties in relaxation coefficients.

coefficients from few to tens of meV. It can be shown that the third order conductivity tensor is mainly dominated by the interband transitions and Rabi-type oscillations determine their frequency dependence for high-energy photons. The frequency variation of the $\sigma^{(3)}_{xxxx}(\omega,\omega,\omega)$ which is responsible for the third harmonic generation is shown in Fig. 2.8(a). The resonant features of this response can be explained based on the Rabi oscillations in the reciprocal space. The integrand in Eq. (2.56) for $\omega_{p,q,r} = \omega$ possesses four simple poles at $\Omega_{\mathbf{k}} \approx \pm\omega, \pm\omega/3$. In the absence of Pauli blocking , i.e. for $\hbar\Omega_{\mathbf{k}} >\sim 2E_f$, the interband transitions take place. The overall response is the superposition of the broadened resonances in the reciprocal space. The resonances around the $\hbar\omega \sim 2E_f$ are stronger leading to appearing of the peaks around $\hbar\omega \sim \frac{2}{3}E_f$ and $\hbar\omega \sim 2E_f$.

The theoretical prediction of $\sigma^{(3)}_{xxxx}(\omega,\omega,-\omega)$ is also plotted in Fig. 2.8(b). This part of the nonlinearity contributes in the nonlinear refractive index. This component of the nonlinear response exhibits resonant behavior around $\hbar\omega \sim 2E_f$. The nature of this resonant behavior can be explained by looking at the imaginary of the integrand in Eq. (2.56). The integrand for $\omega_{p,q,r} = \omega,\omega,-\omega$ has two second order poles at $\Omega_{\mathbf{k}} \approx \pm\omega$ . The amplitude of the absorption for such poles is roughly proportional to the slop of population difference. Those resonances are significantly stronger around the Fermi energy level where the population difference abruptly changes.

The equivalent third order bulk susceptibility of graphene is related to the third order

surface dynamic conductivity via

$$\chi^{(3)}(\omega_p, \omega_q, \omega_r) = \frac{\sigma^{(3)}_{xxxx}(\omega_p, \omega_q, \omega_r)}{i(\omega_p + \omega_q + \omega_r) d_{gr} \varepsilon_0} \tag{2.70}$$

where $d_{gr}$ is the equivalent thickness of graphene which is typically around $d \approx 3\mathring{A}$ [76, 94] and $\varepsilon_0$ is the free space permittivity. Obviously for the case of graphene, the definition of the nonlinear bulk susceptibility is ambiguous due to the arbitrariness in the definition of the thickness of the two-dimensional structure. In the Kerr-type nonlinear response, the dependence of the complex refractive index $n$ on the intensity of light $I$ is given by

$$n = n_0 + (n_2 - ik_2) I \tag{2.71}$$

Where $I = 2\epsilon_0 \mathrm{Re}\{n_0\} c \left|\mathbf{E}\right|^2$ ($c$ is the speed of light). The nonlinear coefficient $n_2$ is related to the bulk susceptibility $\chi^{(3)}(\omega, \omega, -\omega)$ as [121]

$$n_2 - ik_2 = \frac{3}{4\epsilon_0 c \left|n_0\right|^2} \chi^{(3)}(\omega, \omega, -\omega) \left[1 - i \frac{\mathrm{Im}\{n_0\}}{\mathrm{Re}\{n_0\}}\right] \tag{2.72}$$

It is easy to show that for the case of graphene this expression is merely independent of the particular choice of $d_{gr}$ and it introduces an intrinsic parameter. Fig. 2.9 displays our theoretical prediction for the real and imaginary parts of the Kerr coefficient $n_2 - ik_2$ at the room temperature.

Fig. 2.9 shows that over a wide range of frequency and far from the resonances, the nonlinear coefficient is around $n_2 \sim 10^{-8}\mathrm{cm}^2\mathrm{W}^{-1}$. The predicted value is reasonably close to the experimental results reported in the next section. This curve also indicates that the Kerr nonlinearity of graphene is relatively strong compared to the other known nonlinear semiconductors such as GaAs, AlGaAs and Ge. More specifically, the nonlinear Kerr coefficient of GaAs and AlGaAs in the near-infrared range, have been reported $-1.5 \times 10^{-12}\mathrm{cm}^2\mathrm{W}^{-1}$ and $1.12 \times 10^{-12}\mathrm{cm}^2\mathrm{W}^{-1}$ respectively [122].The Kerr coefficient of Ge in the far-infrared range has been reported to be around $1.5 \times 10^{-12}\mathrm{cm}^2\mathrm{W}^{-1}$ [122].

It is quite interesting that nonlinear Kerr coefficient of graphene can be tuned by changing the Fermi energy level and strong Kerr type nonlinearity can be achieved in appropriately gated graphene monolayer and chiral multilayer graphene.

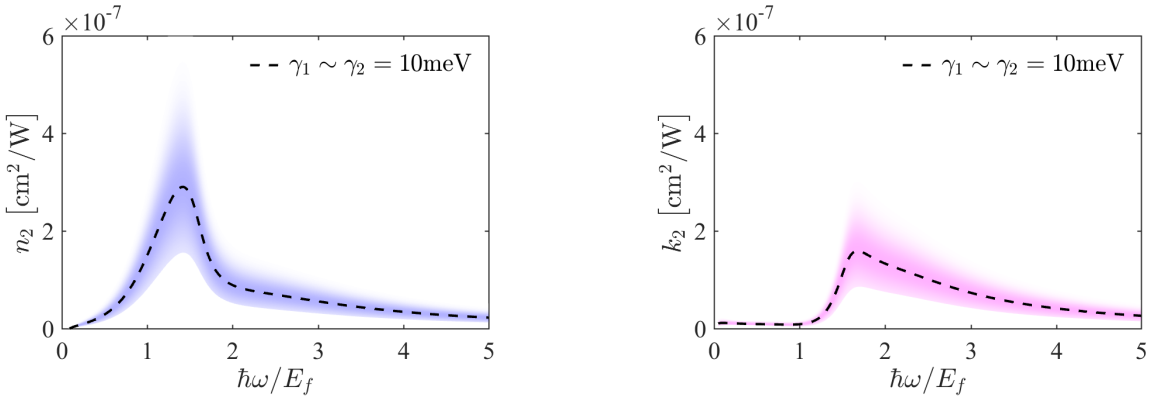


Figure 2.9: Kerr nonlinear coefficient of graphene [i.e. $n_2 - ik_2$ defined in Eq. (2.71)] at $T = 300\text{K}$. (a) nonlinear refractive index $n_2$ (b) nonlinear absorption $k_2$. Over a wide range of frequency the Kerr coefficient is around $\sim 10^{-8}\text{cm}^2\text{W}^{-1}$. Shaded regions describe the variation of the coefficients due to uncertainties in the relaxation coefficients.

## 2.9 Z-Scan Characterization of the Nonlinear Refractive Index of Graphene

In section 2.8, the estimated numerical values for the nonlinear optical coefficients of graphene were presented based on the theoretical model that has been developed in this chapter. Among the nonlinear coefficients, the Kerr-type nonlinearity can be conveniently yet precisely measured using the so-called *z-scan technique*. The z-scan technique was first reported in 1989 by Sheikh-Bahaei and his colleagues to measure the sign and magnitude of the nonlinear refractive index of thin materials [123, 124]. The operational principle of the z-scan technique is based on the correction of phase and amplitude distortions during beam propagation through a Kerr nonlinear medium.

Within the last decade, several attempts have been made to experimentally characterize the nonlinear response of graphene in general and the Kerr coefficient in particular [39, 76, 77, 77–80]. Reported values for the Kerr coefficient of graphene are listed in Table 2.1. Apart from highly probable experimental errors, the discrepancies between the various experimental reports might have multiple origins. Specifically, graphene on different substrates does not necessarily retain all of its original properties. For instance, a graphene monolayer transferred over $SiO_2$ usually suffers from unavoidable phonon induced scatterings effects. Depending on the quality of the sample under test —with different dop-

Table 2.1: Reported experimental values for the Kerr coefficient of graphene.

| $n_2[\text{cm}^2/\text{W}]$ | Sample | Method | Experimental Parameters | Ref. |
|---|---|---|---|---|
| $\sim +1 \times 10^{-7}$ | CVD graphene transferred onto quartz | Z-scan | $\lambda$ = 1550nm ,$\tau_{pulse} \sim$ 3.8ps | [77] |
| $\sim +1.4 \times 10^{-7}$ | CVD graphene transferred onto quartz | Z-scan | $\lambda$ = 1562nm ,$\tau_{pulse} \sim$ 1.4ps | [80] |
| $\sim +1.4 \times 10^{-9}$ | CVD graphene transferred onto quartz | Z-scan | $\lambda$ = 733nm ,$\tau_{pulse} \sim$ 100fs | [78] |
| $\sim -2 \times 10^{-8}$ | CVD graphene transferred onto quartz | Z-scan | $\lambda$ = 1550nm , $\tau_{pulse} \sim$ 3.8ps | [79] |
| $\sim -1.07 \times 10^{-9}$ | CVD graphene transferred onto quartz | Optical Kerr effect method coupled to optical heterodyne detection (OHD-OKE) | $\lambda$ = 1600nm , $\tau_{pulse} \sim$ 180fs | [79] |

ing levels– experimental results might vary. Moreover, different experimental methods used to probe a sample would significantly affect the results.

With consideration of the above facts, a robust theoretical model would be expected to predict both the orders of magnitudes as well as the trends connected with actual physical phenomena. In the following sections, the experimental results obtained from the z-scan experiment are presented. The wavelength dependence of the Kerr coefficient is investigated and discussed. Ultimately, a reasonable agreement is achieved between the experimental results and the theoretical model developed in this chapter.

### 2.9.1 Z-Scan Technique: Operational Principles

One of the processes resulting from the intensity dependent refractive index is the self-focusing (or defocusing) effect as light travels through a Kerr type nonlinear material.

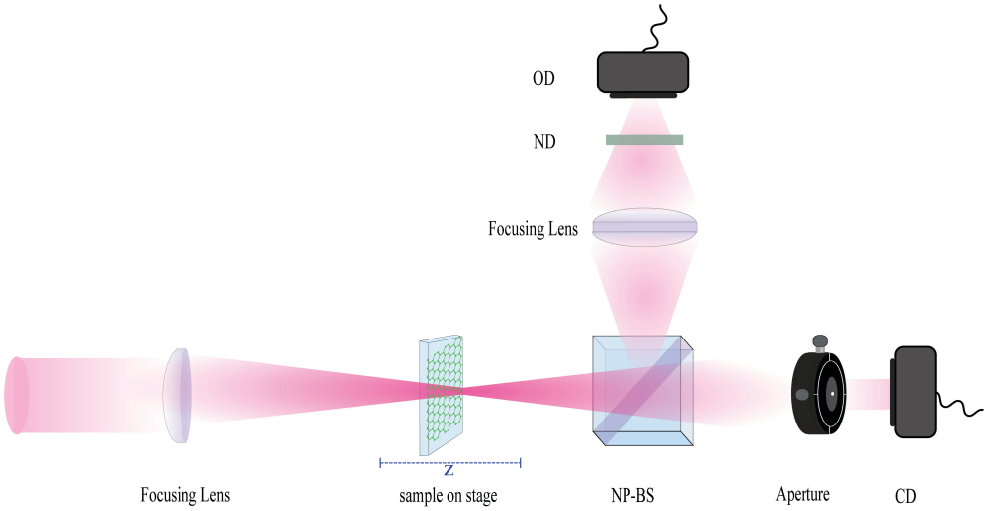


Figure 2.10: Optical set-up used for the Z-scan measurement. The high power laser beam is guided to the first focusing lens where the beam is focused and the sample is translated through the focal plane. The transmitted beam is split into two with a 50:50 beam splitter (NP-BS) into the open aperture detector (OD), and the closed aperture detector (CD) through the pinhole. To avoid any damage to the detector a Natural Density filter (ND) is used in front of the OD.

At sufficiently high field intensities, such that the nonlinear effects become dominant, a Gaussian beam spatially modulates the refractive index profile as a result of the intensity dependent refractive index. The modulated profile essentially acts like a lens so that the wavefronts are deformed and light is focused (assuming a positive nonlinear index $n_2$) or defocused (for a negative nonlinear index) . In addition to the phase distortion effect that predominately originates from the real part of the Kerr coefficient, the medium tends to become transparent under high intensity illuminations and amplitude distortion takes place. The phase and amplitude distortion effects are captured by the closed- and open-aperture z-scan configurations, respectively. The measurement setup is schematically shown in Fig. 2.10.

The analysis follows the changes in the incident beam as it enters and propagates through the sample, and then follows the free space propagation of the modified beam to the aperture and detector plane. Let us assume that a Gaussian beam shines on a thin Kerr-type material (graphene for instance) and the material is placed perpendicular to the propagation direction of the beam. In a high intensity regime (that the absorption of thin material fades away), the beam acquires an additional phase correction $\Delta\Phi(x, y)$

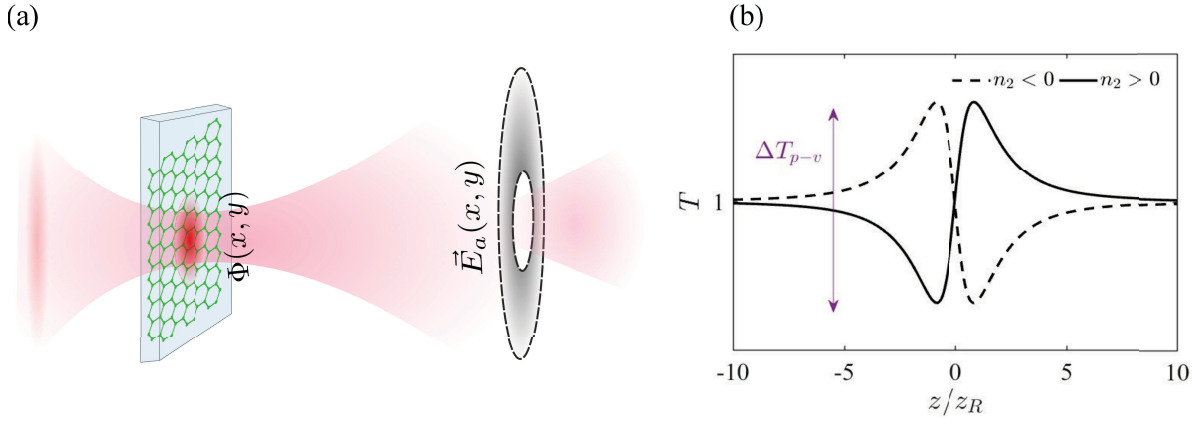


Figure 2.11: (a) Schematics of beam propagation and coupling to the detector. (b) Normalzied transmission profile.

due to the spatially modulated refractive index in the transvers direction (See Fig. 2.11). A full numerical solution for Gaussian beam propagation through a Kerr-type nonlinear medium is complicated and out of scope for this thesis. Here, only the results of the calculation are presented. A detailed breakdown of the technique can be found in the original references [123, 124].

As schematically shown in Fig. 2.11, the phase correction introduced by the Kerr medium causes the beam to deviate from its original form.The phase and amplitude of the beam as it propagates through the sample can be obtained from the paraxial wave approximation. Once the amplitude and the phase of the beam exiting the sample are known, the field distribution at the far-field aperture can be calculated using diffraction theory (Huygens principle). One of the most convenient approaches is to invoke Gaussian wave expansion. The electric field at the exit plane is decomposed into a summation of Gaussian beams through the Gabor expansion technique [125]. The propagation of the individual Gaussian components can then be readily carried out.

In a practical measurement setup, the aperture is placed in the far field region so that its distance from the focal point is much larger than the Rayleigh Length of the focused beam ($z_R$). Taking $z = 0$ as the focal plane, a geometry-independent normalised transmittance is [123]

$$T(z, \Delta\Phi_0) \approx 1 - \frac{4\Delta\Phi_0(z/z_R)}{[(z/z_R)^2 + 9][(z/z_R)^2 + 1]} \tag{2.73}$$

where $\Delta\Phi_0$ is the on-axis phase shift at the focal plane and is defined as $\Delta\Phi_0 \triangleq kn_2I(x =$

$0, y = 0)L_{eff}$. The parameter $k$ is the wavenumber and the length $L_{eff}$ is the effective interaction length of the sample defined as

$$L_{eff} \triangleq \frac{1 - \exp(-\alpha L)}{\alpha} \tag{2.74}$$

where $\alpha$ is the linear absorption coefficient. In the case of graphene it can be shown that the effective interaction length is equivalent to the hypothetical thickness $d_{gr}$ that has been selected for graphene. This equation can be fit to normalised Z-scan data to obtain an estimation for $\Delta\Phi_0$. After some algebaric steps, it can be shown that the peak-valley separation is [123]

$$\Delta T_{p-v} \approx \frac{8\,|z_{pv}/z_R|}{[(z_{pv}/z_R)^2 + 9][(z_{pv}/z_R)^2 + 1]}\Delta\Phi_0 \approx 0.406\Delta\Phi_0 \tag{2.75}$$

The above equation can be conveniently used to find the projected Kerr coefficient.

### 2.9.2 Experimental Results

The z-scan experiment was performed to characterize the Kerr coefficient of a monolayer graphene transferred over a thin quartz substrate. The quartz layer is fairly transparent and its nonlinear behavior negligible [126]. The former fact allows us to assume that the beam profile is minimally impacted by the multiple reflections from the interfaces, and the latter implies that the self-focusing effect is merely attributable to the graphene. To confirm that the self-focusing effect is exclusively originating from the graphene's nonlinearity, we also conducted a similar experiment on a bare quartz sample. An ultrafast tunable laser (PART: *Coherent Chameleon Vision S*) with a pulse duration of $\sim$ 100fs and a repetition rate of 80MHz was used as the source. The experiment was performed for multiple wavelengths from 700nm to 1050nm.

The z-scan profiles for the closed- and open-aperture configurations are displayed in Fig. 2.12. It is obvious from Fig. 2.12(b) that the bare quartz sample does not prompt any self-focusing effect and the Kerr nonlinearity is caused by the graphene layer. In agreement with the theory, the valley-peak configuration confirms that the graphene sample has a positive Kerr coefficient.

The projected Kerr coefficient of graphene (i.e. $n_2$) versus wavelength as well as the theoretical prediction are shown in Fig. 2.13. The yellow shaded region displays the Kerr coefficient predicted by the theory with all uncertainties included. The uncertainties are due to the unknown values for the relaxation parameters as well as the Fermi energy level.

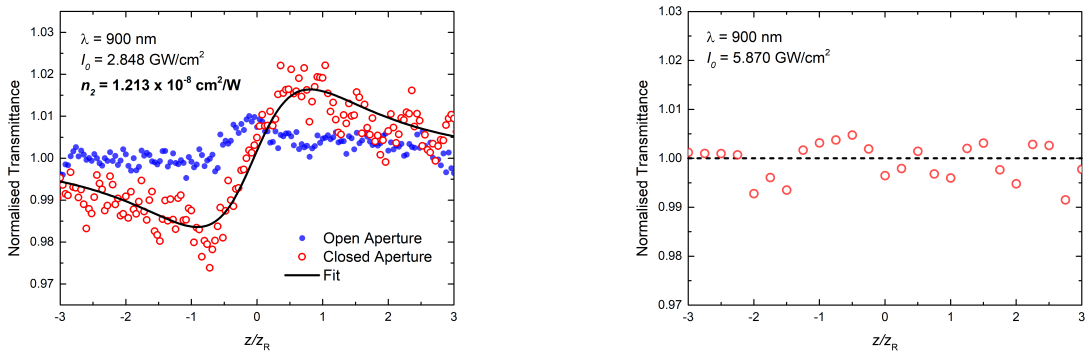


(a) (b)

Figure 2.12: Z-scan profile for the wavelength $\lambda = 900$meV. The $z = 0$ location corresponds to the beam waist. (a) Graphene covered quartz substrate (b) Bare quartz substrate.

Since graphene is absorptive over the entire wavelength range, the Fermi level should be much smaller than the energy of the photons, i.e. $E_f \ll$ 600meV. The relaxation coefficients varry between a few mev to tens of mev . A nonlinear optimization technique wa employed to find the best fitted values for the unknown parameters. As shown in the figure, the relaxation parameters $\gamma_1, \gamma_2 \approx 10$meV can perfectly explain the experimental results. Assuming $E_f \ll \hbar\omega$, a slight dependence of the Kerr coefficient on the Fermi energy level is observed.

The adopted theoretical model can qualitatively explain the spectral behavior of the Kerr coefficient. It is observed that the Kerr coefficient **quadratically** increases as the wavelength increases. Since the Fermi energy level is small compared to the energy of the photons, the frequency dependence of the linear optical response of graphene can be assumed to be negligibly small. Therefore, the third-order interband optical nonlinearity is responsible for the wavelength dependence of the Kerr coefficient. The physical processes that give rise to the nonlinear refractive index and the accompanying nonlinear absorption include ultrafast bound electronic processes, excited state processes where the response times are dictated by the characteristic formation and decay times of the optically induced excited states. It was argued in section 2.5 that in graphene, Kerr-type nonlinearity over the optical range of frequency is predominantly caused by the self-coupling effect. Due to the ultrafast Rabi oscillations at the zero detuning region (i.e. $\Delta_{\mathbf{k}} \approx 0$) the steady state population difference is modified significantly by the intense illuminating field. One can speculate that the asymptotic frequency dependence of the Kerr coefficient can be gleaned

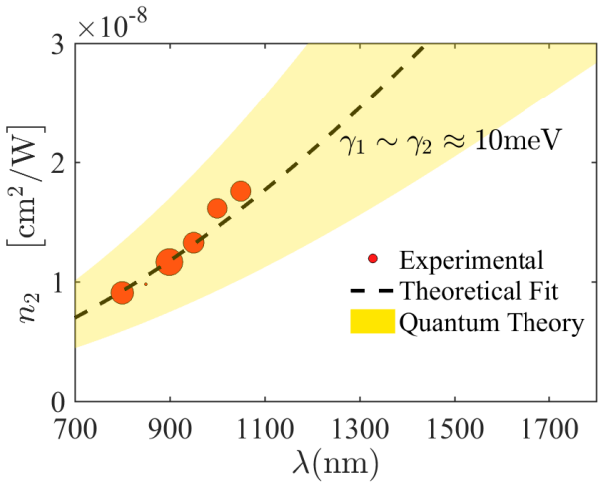


Figure 2.13: Wavelength-dependence of the Kerr coefficient of graphene from experimental results and the adopted quantum theory. Yellow shaded region is obtained from quantum theory for $\sim$ 1meV $< \gamma_1, \gamma_2 <\sim$ 20meV. A perfect theoretical fit is achieved by setting the relaxation coefficient to be 10meV.

from the steady state inversion around the zero detuning region as

$$\widetilde{\mathcal{N}}_{\mathbf{k}}^{st} = \mathcal{N}_{\mathbf{k}}^{eq} \frac{\gamma^{(1)}}{\gamma^{(1)} + \gamma^{(2)} \left|\mathcal{L}_{\mathbf{k}}(\omega)\right|^2 \left|\widetilde{\Phi}_{\mathbf{k}}\right|^2}\Bigg|_{\Delta_{\mathbf{k}} \approx 0} \approx \mathcal{N}_{\mathbf{k}}^{eq} \left[1 - \frac{1}{\gamma^{(1)}\gamma^{(2)}} \left|\widetilde{\Phi}_{\mathbf{k}}\right|^2\right] \tag{2.76}$$

where $\mathcal{L}_{\mathbf{k}}(\omega) = 1/(\gamma^{(2)} + i\Delta_{\mathbf{k}})$. As discussed in the previous section, the spontaneous saturation effect can be safely neglected over the optical range of frequency for moderately doped graphene. The corresponding steady state polarization is obtained from Eq. (2.62b). The induced nonlinear interband current is then calcuated as (see Appendix C)

$$\mathbf{J}_{NL}(\omega) = -\frac{e^2}{\hbar} v_F g_s g_v D \iint_{\mathrm{RBZ}} \mathrm{d}^2\mathbf{k} \left\{ \hat{\varphi}_{\mathbf{k}} (\hat{\varphi}_{\mathbf{k}} \cdot \mathbf{E}) \frac{1}{k} \mathcal{L}_{\mathbf{k}}(\omega) \left[\widetilde{\mathcal{N}}_{\mathbf{k}}^{st} - \mathcal{N}_{\mathbf{k}}^{eq}\right] \right\} \tag{2.77}$$

$$\sim \beta \frac{e^2}{\hbar} g_s g_v D \frac{1}{\gamma^{(1)}\gamma^{(2)}} \left|\frac{e}{\hbar k}\mathbf{E}_0\right|^2 \mathcal{N}_{\mathbf{k}}^{eq}\Big|_{k=K_0} \mathbf{E}_0 \tag{2.78}$$

where $2\hbar v_F K_0 = \hbar\omega$ determines the zero detuning circle around the Dirac point. The dimesionless parameter $\beta \sim \pi$ accounts for the angular integration. Since the population

difference $\mathcal{N}_{\mathbf{k}}^{eq}$ is almost constant for $\hbar\omega \gg E_f$, the $1/K_0^2$ term in the above equation dictates the frequency dependnece of the Kerr type nonlinearity. Obviously, the nonlinear current is quadraticly proportional to the wavelength as $\mathbf{J}_{NL}(\omega) \precsim \omega^{-2} \propto \lambda^2$. It is noted that the quadratic spectral dependence of the Kerr coefficient reflects the peculiar linear dispersion of the quasiparticles.

## 2.10 Summary

A semiclassical theory of light-graphene interaction in linear and nonlinear regimes has been detailed. Focusing on the scale-invariancy and chiral character of Bloch quasi-particles in graphene, the Semiconductor Bloch Equations (SBEs) were formulated. The advantage of SBEs is two-fold: first they provide a convenient mathematical scheme leading to the analytical expressions for different contributions of the linear and the nonlinear optical response of graphene. Second, SBEs encode the topological properties of the band structure in an effective dipole expression appearing in the equations.

The topologically protected chiral nature of the charged carriers in graphene entails the diverging interband optical coupling (i.e. large effective dipole) in the vicinity of the Dirac point. The treatment of the unconventional interband coupling has been a source of controversy in the nonlinear optics of graphene to date. A physically consistent explanation that could resolve this issue has been proposed. It was deliberated how the large interband coupling gives rise to ultra-fast Rabi oscillations which excite the quasiparticles at such a rate that there is insufficient time for them to decay back to the ground state and optical saturation takes place. Since this saturation can be instigated by even arbitrary weak field intensities, the effect was considered a spontaneous saturation effect. The theory was substantiated by a direct time domain analysis of the graphene Bloch equations.

Since the saturation effects are highly influenced by the relaxation dynamics, an accurate evaluation of the relaxation coefficients is crucial to genuinely capture the essential physics. A full many body analysis was performed , which combined all relaxation mechanisms including electron-electron and electron-phonon interactions to extract the effective relaxation coefficients. It was concluded that the carrier relaxation dynamics are quite slow for low energy quasiparticles which in turn yields more pronounced saturation effect around the Dirac point. The practical implications of this effect was examined via the example of pump-probe spectroscopy and it was concluded that the unconventional saturation effect is expected to be readily observed in such experiments.

Owing to the spontaneous saturation effect, the perturbation approach to the development of the optical response of graphene should be revisited. Specifically, perturbation the-

ory collapses in describing the nonlinear optical interactions within the saturated regions. Therefore, exclusion of the saturated states is required to find the nonlinear coefficients.

Using SBEs, the problem of the interaction can then be decomposed into the quasi-calssical Boltzman transport and the interband time evolution. The nonlinear parts of the optical response can be classified as pure intraband, pure interband and a combination of the two. Introducing a novel mathematical framework, analytical expressions for different contributions of the conductivity tensors have been derived for the first time.

The third order susceptibility and nonlinear refractive index were calculated. It was shown that our prediction for the Kerr nonlinear coefficient for graphene is in reasonably good agreement with the experimentally obtained results. It has been demonstrated that Kerr nonlinear coefficient of graphene can be tuned by changing the Fermi energy level and relatively strong Kerr nonlinearity can be attained in a gated graphene monolayer.

The measurement results for the Kerr coefficient of CVD-grown graphene (transferred onto quartz) was presented. The spectral dependence of the nonlinear refractive index of graphene was measured using z-scan technique. It was shown that the experiment results can be perfectly explained by the theory developed in this chapter. The findings from the present study should be instrumental in instigating similar explorations for other Dirac and Weyl semimetals.

The applications of the noticeably strong nonlinearity of graphene in two practical structures are discussed in the succeeding chapters.

# Chapter 3

# Graphene-Integrated Plasmonic Structure for Optical Third Harmonic Generation

*Tuning the Color of Gold.*

## 3.1 Introduction

Nonlinear up-conversion of the visible and near infrared light to the higher harmonics has been the topic of intense research in recent years [127]- [128]. Applications are diverse and encompass many areas ranging from photonics and laser technology to biomedical imaging and sensing [129]- [131]. The conventional up-conversion techniques rely on the phase matching of the intense electromagnetic fields in bulk nonlinear crystals. The bulk nonlinear structures take advantage of the phase matching to efficiently utilize the cascaded nonlinear processes and accumulation of nonlinear interactions within a long propagation path [32]. The guided-wave frequency mixing methods essentially suffer from an excessive amount of absorption loss that limits the conversion efficiency. In order to perform nonlinear operations in a highly integrated fashion with low power consumption, one would require to hire effective mechanisms to enhance the field intensity inside the nonlinear medium. Recent rapid advancements in nanofabrication technologies have widened the realm of possibilities in nanophotonics, nonlinear and sub-wavelength optics. Realizing nonlinear optics in sub-wavelength scale paves the way for low cost integrated photonics [132]. The ultra-high-Q photonic crystal nanocavities [133]- [134] and nanostructured

materials are examples of such structures. Specifically, the plasmonic plasmonic metasurfaces offer very small mode volume guaranteeing highly enhanced field intensity [132]. The region of nonlinear interaction nonetheless is limited to the mode extend. That hinders the efficient adoption of the bulk nonlinear mediums for frequency mixing applications. To circumvent this issue, the integration of artificial quantum materials such as highly nonlinear multiple-quantum-well semiconductor heterostructures and plasmonic nanostructures made of noble metals has been proposed recently [135]- [136]. In this chater, we propose the integration of the plasmonic metasurfaces and graphene [137] to perform nonlinear frequency mixing.

As extensively discussed in the previous chapter, the symmetries of the graphene lattice entail significantly strong nonlinear optical properties that might make graphene a compelling candidate for integrated nonlinear optics. This is an endeavor to explore the possibility of utilizing graphene in future integrated nonlinear optical devices. Beside the relatively strong optical nonlinearity of graphene, there are several advantages in using graphene over the conventional alternatives for nonlinear optics. Though some metals may also exhibit strong nonlinearity, they are generally opaque and highly refractive [138]. Unlike metals, graphene is almost transparent maintaining optical structures intact. Integrability and ease of fabrication are also among the reasons why graphene has already ignited extensive interest in the optoelectronics and even quantum optics.

In the wavelength conversion device proposed in this chapter, graphene acts as the nonlinear medium. The centrosymmetry of the graphene lattice prevents even-ordered nonlinear processes and hence the first nonlinear term is the third order term [139]. Accordingly the structure is designed for third harmonic generation (THG).

The main objective of this chapter is twofold. First, a design methodology for an efficient plasmonic graphene-based third harmonic generator is proposed. As a particular example, we focus on a frequency tripler converting an optical beam in the near infrared wavelengths ($\sim$ 800nm) to its third harmonic at UV range of frequency. Second, a fast hybrid numerical method is introduced to analyze and optimize the dimensions of the structure.

The proposed structure is composed of a graphene layer transfered over a multilayer structure. A periodic array of shaped gold nanoparticles, designed to be resonant around the wavelength of 800nm, is positioned on top of the graphene sheet. The dimensions of the multilayer structure and nanoparticles are optimized to tune the plasmonic resonance frequency and maximize the enhancement factor both at the fundamental frequency and its third harmonics. The multilayer structure is designed to act as a Bragg mirror which provides an additional enhancement of the field intensity due to the reflection from the

band gap medium.

The numerical method introduced in this chapter is used to analyze and to optimize the dimensions of the structure for maximum conversion efficiency over a wide range of frequency. The numerical method combines the Floquet mode analysis and the Generalized Multipole Technique (GMT) [140] to develop a circuit model for the entire structure. The circuit model can be widely used in the fast analysis and optimization of many nanostructured layered media. Exploiting the fast solver, we will drastically enhance the third harmonic conversion efficiency by many orders of magnitude exceeding the amounts of enhancement reported in the literature so far [141]. Furthermore, the circuit model developed in this chapter, provides a convenient tool for the nonlinear analysis of similar plasmonic structures.

This chapter is organized as follows. The quantum theory of third order frequency mixing in graphene is outlined in Section 3.2. We present the operation principles of the structure and design considerations in Section 3.3. Section 3.4 is devoted to the numerical analysis and optimization of the wavelength conversion device. The numerical results are discussed in Section 3.5. The conclusions will be drawn in the last section.

## 3.2 Optical Third Harmonic Generation in Graphene

In the model adopted in this chapter, we use the nonlinear response coefficients derived in chapter 2 . Using the conductivity tensors the induced surface current at the third harmonic is obtained in terms of the electric field at the fundamental frequency. The three additive tensors constituting the third order conductivity tensor $\overline{\overline{\sigma}}^{(3)}(\omega_p, \omega_q, \omega_r)$ are

$$\overline{\overline{\sigma}}^{(3)}_{intra}(\omega_p, \omega_q, \omega_r) = \sigma_1^{(3)}(\omega_p, \omega_q, \omega_r)\overline{\overline{T}}_1 \tag{3.1a}$$

$$\overline{\overline{\sigma}}^{(3)}_{inter}(\omega_p, \omega_q, \omega_r) = \sigma_2^{(3)}(\omega_p, \omega_q, \omega_r)\overline{\overline{T}}_2 \tag{3.1b}$$

$$\overline{\overline{\sigma}}^{(3)}_{intra-inter}(\omega_p, \omega_q, \omega_r) = \sigma_3^{(3)}(\omega_p, \omega_q, \omega_r)\overline{\overline{T}}_3 \tag{3.1c}$$

where the tensors $\overline{\overline{T}}_1$, $\overline{\overline{T}}_2$ and $\overline{\overline{T}}_3$ as well as explicit expressions for the scalars $\sigma_i^{(3)}$'s are given section 2.5.2 . The tensor $\overline{\overline{\sigma}}^{(3)}$ is the summation of the three tensors displayed above.

$$\overline{\overline{\sigma}}^{(3)}(\omega_p, \omega_q, \omega_r) = \overline{\overline{\sigma}}^{(3)}_{intra} + \overline{\overline{\sigma}}^{(3)}_{inter} + \overline{\overline{\sigma}}^{(3)}_{intra-inter} \tag{3.2}$$

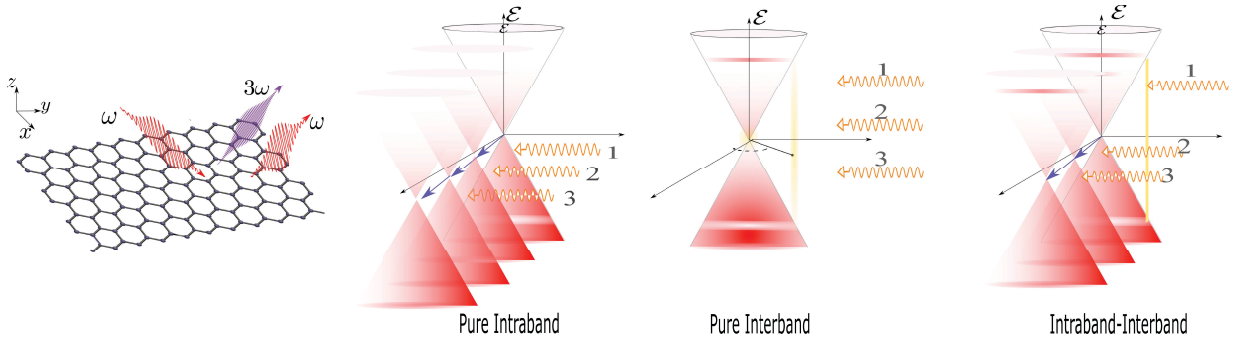


Figure 3.1: schematics of the relevant three-photon processes for optical third harmonic generation

The induced surface current over the graphene layer at the third harmonic of $\omega_0$ is then calculated as

$$\mathbf{J}(3\omega_0+\delta) = \iint \mathrm{d}\delta_1\mathrm{d}\delta_2 \overline{\overline{\sigma}}^{(3)}(\omega_0+\delta_1,\omega_0+\delta_2,\omega_0+\delta-\delta_1-\delta_2)\mathbf{E}(\omega_0+\delta_1)\mathbf{E}(\omega_0+\delta_2)\mathbf{E}(\omega_0+\delta-\delta_1-\delta_2) \tag{3.3}$$

where we have assumed that the field at the fundamental frequency has a finite bandwidth centered around $\omega_0$.

The schematics of the distinct three-photon processes are shown in Fig. 3.1. As disuceed in the previous chapter, the intraband evolution of the quasiparticles is attributed to the classical motion of the fermionic distribution in the reciprocal space and can be described based on the semiclassical Boltzman's equation [99]. In contrary, for the pure interband part, the three-photon process has only quantum origin and can be interpreted as the absorption of three successive photons in a two-level atomic system. The last contribution arises due to the cooperative intraband and interband transitions as schematically depicted in Fig. 3.1. As elucidated in the previous chapter, six possible combinations of intraband and interband dynamics can contribut in the third order frequency mixing in graphene. However, due to the fact that structure is designed to be functional in the optical range of frequency, only three relevant terms ahve domaninat impact. For moderately doped graphene, the pure interband term plays the dominant role in the optical range of frequency and is the main reason behind the resonant behavior of the third order conductivity around $2E_F = \hbar\omega$ and $2E_F = 3\hbar\omega$. The impact of relaxation rate $\gamma$ on the third order conductivity is also shown in Fig. 3.2(a). We set $\gamma = 10$meV (the relaxation time

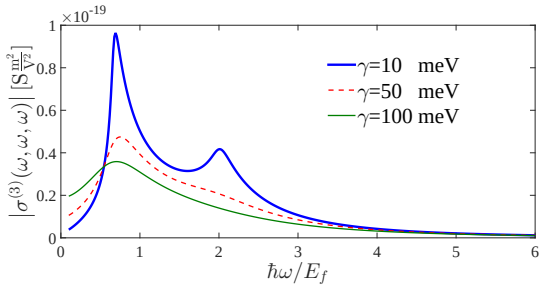


(a)

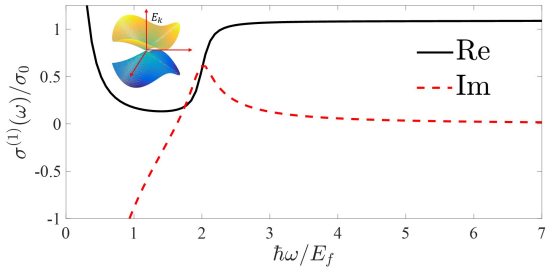


(b)

Figure 3.2: (a) Magnitude of the third order conductivity of graphene as a function of the normalized frequency for $\gamma = 10\text{meV} \equiv 65\text{fs}$, $\gamma = 50\text{meV} \equiv 13\text{fs}$ and $\gamma = 100\text{meV} \equiv 6.5\text{fs}$. (b) Linear optical conductivity of graphene beyond the Dirac cone approximation. The conductivity is normalized to $\sigma_0 = e^2/4\hbar$. For higher frequeinces the absorption is not flat.

of $\tau = 65\text{fs}$) throughout this work. In order to take advantage of the resonant third order nonlinear interaction for maximum conversion efficiency, the Fermi energy level should be tuned to either $2E_F = \hbar\omega$ or $2E_F = 3\hbar\omega$ (where $\omega$ is the fundamental frequency). In the optical range of frequency, the second resonance condition requires very large gate voltage level which is hardly achievable in practice. As a result, the Fermi energy level should be tuned to $2E_F = \hbar\omega_0$ where $\omega_0$ is the center frequency of pump signal.

It is worth mentioning that the tensors $\overline{\overline{T}}_1$, $\overline{\overline{T}}_2$ and $\overline{\overline{T}}_3$ are derived based on the group symmetries of the graphene lattice and they are independent of any quantum theory adopted. For instance, the pure interband term which plays the dominant role, carries the hexagonal symmetry of the graphene lattice [71, 73]. As a result, the spatial distribution of the induced current at the third harmonic and the way it radiates is determined by the symmetries of the lattice. However the multiplicative factors $\sigma_i$'s do depend on the special quantum theory employed.

The linear conductivity of the graphene layer for normal illumination is plotted in Fig. 3.2(b). In the subsequent sections, we would need to use the linear conductivity of graphene in the pump frequency (fundamental frequency) and its third harmonic. The linear optical response of graphene to the third harmonic photons is obtained beyond the Dirac cone approximation. Due to the deviation from the Dirac type dynamics, the absorption spectral of graphene is slightly slopped at higher frequencies. The details of analysis are given in the Appendix A.

## 3.3 Structure and Design Methodology

The schematic of the proposed structure is shown in Fig. 3.3. The periodic array of the gold nanoparticles is placed above the graphene sheet. Graphene is transfered over a multilayer structure. Throughout this chapter, the lateral period of the nanoparticle array in $x$ and $y$ are designated by $W$ and $L$ respectively. The multilayers structure is made of the alternative layers of sapphire and UV fused silica. These materials have been selected due to their nearly flat refractive index over a wide range of frequency from near infrared to UV. The refractive index of sapphire is $n_> \approx 1.8$ and UV fused silica has the refractive index of $n_< \approx 1.4$. It is assumed that the structure is illuminated from the top by a focused laser beam, whose spectral range is centered around the wavelength of $\sim 800$nm. The third harmonic field is captured from the top as well. The multilayer structure is composed of twelve layers. As will be detailed, for properly selected $L$ and $W$, one would need to just optimize the dimensions of the first few layers to maximize the enhancement of the field intensity at the graphene layer. The rest of the multilayer is simply a quarter-wave Bragg mirror. We would optimize the thicknesses of the first five layers and the dimensions of the nanoparticles to maximize the conversion efficiency.

The structure employs two mechanisms to enhance the field intensity at the graphene layer and improve the radiation efficiency of the third harmonic: plasmonic resonance and reflection from the multilayer structure. Although the plasmonic resonance can significantly enhance the field intensity inside and around the nanoparticles, the field does not necessarily interact with graphene in an efficient manner. The graphene sheet laid on $xy$-plane can only interact with the transverse components of the total electric field. In order to change the polarization of the total resonant field to make the complete interaction possible, a *quasi PMC* boundary condition below the graphene sheet is required. A PMC boundary condition guarantees efficient interaction of the resonant field with the graphene sheet. It would also create one more enhancement factor due to the constructive interference of reflected field from the PMC mirror and the total field generated by the

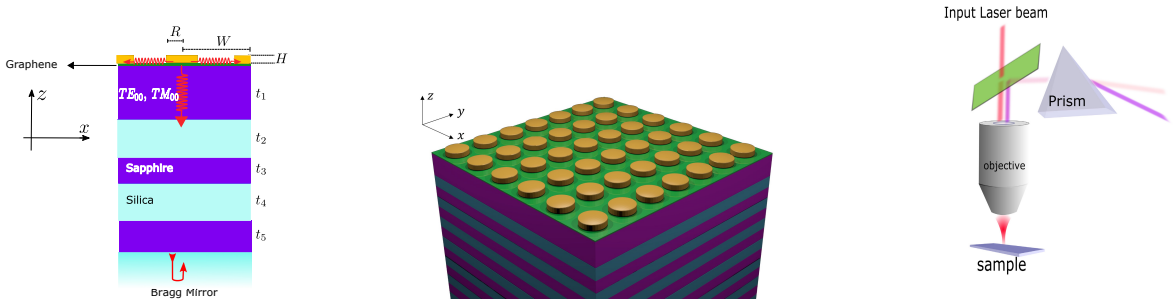


Figure 3.3: Proposed structure for third harmonic generation. Graphene is transferred over a multilayer structure. The multilayer structure is made of the alternative layers of sapphire and fused silica. $R$ is the radius of the nano-disks and $H$ is their height. The inter-particle separations in the $x$ and $y$ directions are $W$ and $L$ respectively.

nanoparticles. The multilayer structure proposed here aims to accomplish these desirable properties.

The multilayer structure is composed of two parts: a quarter-wave Bragg mirror and five layers on the top. The Bragg mirror is intended to completely reflect back the electromagnetic field both at the fundamental frequency and its third harmonic. The top five layers are carefully designed to provide an appropriate amount of phase shift to fulfil the PMC boundary condition just below the graphene sheet. Owing to the plasmonic resonance, the field induced at the fundamental frequency is highly localized around the nanoparticles. The localized field can be expanded in terms of the $\mathrm{TE}^z$ and $\mathrm{TM}^z$ Floquet modes. The transverse wave number associated with the $\mathrm{TE}^z_{mn}$ and $\mathrm{TM}^z_{mn}$ is

$$\mathbf{k}_{mn} = m\frac{2\pi}{W}\hat{x} + n\frac{2\pi}{L}\hat{y} \tag{3.4}$$

where $m$ and $n$ are integeres. The Bragg mirror underneath the structure is made of 7 quarter wave layers of sapphire and UV fused silica that ensures complete reflection for normally incident waves corresponding to $m, n = 0$ Floquet modes (i.e. $\mathrm{TE}^z_{00}$ and $\mathrm{TM}^z_{00}$ modes) . In order to suppress the other Floquet modes, we should select $L, W < \lambda_0$ where $\lambda_0$ is the wavelength of the illuminating field. That would guarantee that the higher order Floquet modes are evanescent in the vertical direction and they are extended only within the first few layers. As more details to be outlined in the subsequent sections, the conversion efficiency can be further improved if the Bragg mirror works at the third harmonic as well. To do so, we select $L = W = 250\mathrm{nm} <\sim \lambda_0/3$. The Bragg condition

at the third harmonic is already satisfied as the thicknesses of the layers are chosen to be $3\frac{\lambda/3}{4}$.

In order to tune the resonance of the nanoparticles to the fundamental frequency, the shape of the nanoparticles should be appropriately tailored. Based on so-called *coupled dipole approximation*, each particle can be modeled by a dipole of quasi-static polarizability $\overline{\overline{\alpha}}$ [142]. Using quasi-static interpretations, the resonance behavior of the nanoparticles can be controlled by changing their relative dimensions and the effective dielectric constant of the medium(s) surrounding the particles. Specifically, freely standing gold nanoparticles whose shape and dimensions can be fabricated using the state-of-the-art technology, are barely resonant in the near infrared range and hence the nanoparticles' surface should be placed next to a dielectric media or alternatively coated by a dielectric layer. This effect reveals another advantage of the multilayer structure in tuning the plasmonic resonance frequency. It is noted that the resonance frequency is merely influenced by the first few layers in the proximity of the nanoparticles. This can be understood based on the quasi-static models describing the plasmonic resonance in the nanoparticles made of noble metals [142]. Having studied the electrostatic polarizability of different geometries, it has been demonstrated in Ref. [143] that resonance frequency of gold nanoparticles can be moved toward the near infrared range by breaking the 3D symmetry of the nanoparticles. Moreover, existence of the sharp edges over the nanoparticles causes an additional enhancement of the electric field at the geometric singularities. As a result, disk shape nanoparticles are selected for plasmonic enhancement around the wavelength of interest. The dimensions of the nanoparticles are designed to be resonant in the presence of the multilayer structure illustrated in Fig. 3.3. In accordance with the aforementioned design considerations of the multilayer structure, in this design step, we can assume that the thickness of the first layer is $\lambda/2$ and the other layers are simply quarter wave. The dimensions of the nanoparticles were then optimized by trial and error in the presence of multilayer structure through use of ANSYS HFSS (finite element solver). Following this recipe for the specific case of 800-UV convertor, we came up with disk shape nanoparticles with the radius of $R = 55$nm and the height of $H = 20$nm.

## 3.4 Hybrid Numerical Technique in the Analysis of the Plasmonic Structure

Because of the strong localization of the electromagnetic field in plasmonic structures, the analysis of such structures are computationally expensive and therefore selecting a suitable numerical method for field computation is crucial. The commercial numerical

solvers based on domain discretization such as Finite Element Method (FEM) and the Finite Difference Time-Domain (FDTD), would require a huge computational resource to model highly localized fields. Alternatively, the existing boundary-discretization methods such as Multiple Multipole method have provided faster solutions for the plasmonic problems [29]. However, their scope of applicability is usually limited to the certain class of the problems where the solution domain contains few inhomogeneities [144]. Beside the issues listed above, the plasmonic structure integrated with two-dimensional materials such as graphene must be analyzed in the spatial spectral domain [145]. The spectral domain response of two-dimensional materials depends on the direction and polarization of the plane wave illuminating the layer. Here we present a hybrid method which combines the advantage of the boundary discretization methods in analyzing the plasmonic structure and the plane wave expansion method in the analysis of the graphene part and the multilayer structure. More specifically, the proposed method combines Floquet mode expansion and Generalized Multiple Technique (GMT) [29] to present a circuit model for the entire the structure. The circuit model is proved to be very efficient for linear optimization of the problem as well as nonlinear analysis of the structure.

The scattering matrix method (network representation) has been widely used before in the analysis of interconnecting separated characterized system blocks. Ref. [146] applies a similar method for fast analysis of multilayer periodic structures such as FSS and phased arrays. The application of the Fourier modal methods and generalized scattering matrix formulation in the fast and rigorous modal analysis of linear optical structures has been thoroughly investigated in Ref. [147].

### 3.4.1 Scattering Matrix Description of the Plasmonic Structure

A complete network description of the plasmonic structure can be obtained by the Floquet mode decomposition of electromagnetic fields. The structure is assumed to be sliced in the distinct cross sections separating its *semi-planar* ingredients as shown in Fig. 3.4. At an arbitrary cross section $z = z_0$ the tangential components of the electric field are expanded in terms of the Floquet mode.

$$\mathbf{E}_t(x, y, z_0) = (\hat{x}\hat{x} + \hat{y}\hat{y}) \cdot \mathbf{E}(x, y, z_0) = \sum_{i,mn} V_{mn}^{(i)}(z_0) \left(\delta_{i1}\hat{\kappa}_{mn} + \delta_{i2}\hat{\xi}_{mn}\right) \exp(-j\mathbf{k}_{mn} \cdot \boldsymbol{\rho}) \quad (3.5)$$

Where $V_{mn}^{(i=1)}$ and $V_{mn}^{(i=2)}$ are the Floquet mode expansion coefficients for the TM and TE modes respectively. The unit vectors $\hat{\kappa}_{mn}$ and $\hat{\xi}_{mn}$ are defined as

$$\hat{\kappa}_{mn} \triangleq \frac{\mathbf{k}_{mn}}{|\mathbf{k}_{mn}|} \quad , \quad \hat{\xi}_{mn} \triangleq \hat{z} \times \hat{\kappa}_{mn} \tag{3.6}$$

In the scattering matrix formulation, every Floquet mode constitutes a hypothetical port. Moreover, the graphene layer and the nanoparticles array both contain two accessible channels corresponding to the upper and lower cross sections. Obviously, the accessible channels contain all the hypothetical Floquet ports contributing in the field expansion at each cross section. Analogous to incident and reflected waves in waveguide terminology, modes occur in pairs of incoming and scattered Floquet modes at each cross section. The scattering matrix establishes a linear relation between incident and scattered Floquet modes appearing in the channels of the semi-planar parts. The scattering matrix of the multilayer structure, the graphene layer and the nanoparticle array are designated by $\overline{S}_M$ , $\overline{S}_G$ and $\overline{S}_M$ respectively.

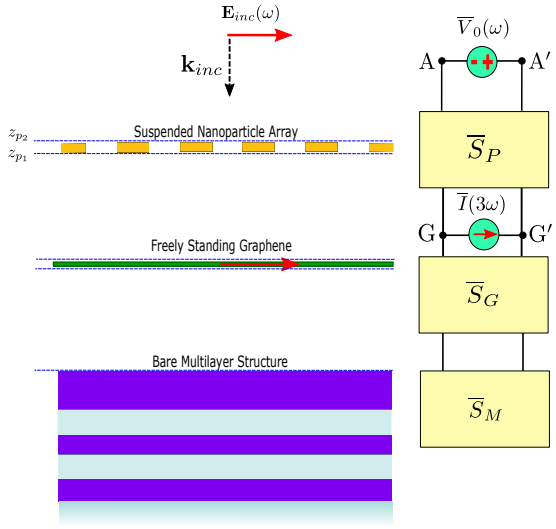


Figure 3.4: Network representation of the plasmonic structure.

As noted below equation (3.5), every Floquet mode is labeled by the index $mn$ representing the lateral variation of the mode and the polarization index $i$. The TM and TE Floquet modes are compactly shown by $i = 1$ and $i = 2$ respectively. In the scattering matrix formulation, the Floquet mode indices $mn, i$ are designated by the collective index

$\alpha$. We also use the index $p$ to show the channel number for the two-channel networks shown in Fig. 3.4. For mathematical convenience, the index $\gamma$ collectively includes $\alpha$ and $p$. The calculation of the scattering matrices $\overline{S}_M$ , $\overline{S}_G$ and $\overline{S}_M$ is detailed in Appendix D. As mentioned earlier, we have used GMT method to construct the scattering matrix associated with nanoparticle array suspended in free space. The computational considerations are briefly discussed in Appendix E.

### 3.4.2 Nonlinear Analysis and Third Harmonic Generation

In the presence of a nonlinear medium subjected to an intense electromagnetic field, the polarization of the medium develops new harmonics further to the fundamental frequency $\omega_0$. The nonlinear optical response of the entire structure can be described by means of the nonlinear wave equation in time domain [32].

$$\nabla \times \nabla \times \vec{E}(\mathbf{r},t) + \mu_0\varepsilon_0 \frac{\partial^2 \vec{E}(\mathbf{r},t)}{\partial t^2} = -\mu_0 \frac{\partial^2 \vec{P}_L(\mathbf{r},t)}{\partial t^2} - \mu_0 \frac{\partial^2 \vec{P}_{NL}(\mathbf{r},t)}{\partial t^2} \tag{3.7}$$

Where $\vec{P}_L$ and $\vec{P}_{NL}$ are the linear and nonlinear polarization vectors respectively. The linear polarization can be obviously merged to the left side of the wave equation. The nonlinear term $\vec{P}_{NL}$, however, acts as a source term which appears on the right side of the wave equation. The nonlinear analysis can be carried out in the frequency domain by separating the harmonics induced in the structure. For the electric field $\mathbf{E}_n$ oscillating at the angular frequency $\omega_n = n\omega_0$, we have

$$\nabla \times \nabla \times \mathbf{E}_n(\omega_n) - \varepsilon_r(\mathbf{r},\omega_n)\omega_n^2\mu_0\varepsilon_0\mathbf{E}_n(\omega_n) = -j\omega_n\mu_0\mathbf{J}_{NL}(\omega_n) \tag{3.8}$$

where $\mathbf{J}_{NL}(\omega_n)$ is the nonlinear current oscillating at the n'th harmonic. The treatment of the nonlinear wave equation is usually complicated due to the coupling of the different nonlinear interactions [32]. For the plasmonic structure described in this chapter the higher order couplings can be safely neglected as the accumulative nonlinear interactions do not occur and as a result the nonlinear currents are only coupled to the linear electric field. This assumption allows us to have independent analysis for the harmonics contributing in the nonlinear response of the system. The nonlinear induced current at the third harmonic is then treated as an impressed current source radiating in the presence of the structure.

The circuit model developed here can be used to find the field radiated by the impressed source caused by the nonlinear interaction. The linear analysis of the structure is first performed to find the induced electric field at the fundamental frequency. The nonlinear

current oscillating at the third harmonic at the graphene layer is then obtained from equation (3.3). At the third harmonic, the current $\mathbf{J}(3\omega_0)$ is modeled by an impressed current source in the linear equivalent network as shown in Fig. 3.4. The plane wave decomposition should be applied to find the vector $\overline{I}$ containing the modal coefficients of the current source.

$$\overline{I}^{(\alpha)}(3\omega) = \left(\delta_{i1}\hat{\kappa}_{mn} + \delta_{i2}\hat{\xi}_{mn}\right) \cdot \frac{1}{WL} \iint_{\text{unit cell}} \mathbf{J}(3\omega) \exp(+j\mathbf{k}_{mn}.\boldsymbol{\rho}) \mathrm{d}s \tag{3.9}$$

We have shown in our calculations that the nonlinear contribution of the gold metasurface in THG can be neglected. Owing to the strong optical nonlinearity of the graphene layer compared to that of gold, as well as, extreme localization of the electric field intensity over the PMC mirror, the third harmonic power is dominated by nonlinear contribution of the graphene layer. According to experimental results reported in Refs. [148]- [149], the third harmonic optical susceptibility of gold is out of the resonance over the near infrared range and the maximum value reported for that quantity is around $\chi^{(3)}_{gold}(\omega,\omega,\omega) \sim 7.71 \times 10^{-19}\mathrm{m}^2/\mathrm{V}^2$ [149]. A full wave calculation has been performed and proved that the strength of *the effective third harmonic dipole* induced over gold nanoparticles per unit cell is at least 2 orders of magnitude smaller than that of graphene. In order to make a sensible comparison, the equivalent surface third order conductivity of the gold nanoparticles defined as $\sigma^{(3)}_{gold} \approx j3\omega H\varepsilon_0\chi^{(3)}_{gold}$ has been calculated. This parameter has the value of $\sigma^{(3)}_{gold} \sim 2.3 \times 10^{-22}\mathrm{Sm}^2/\mathrm{V}^2$ which is 2 orders of magnitude smaller than the third order nonlinear conductivity of graphene around its resonance (see Fig. 3.2(a)). This rough comparison is fairly valide due to the very small thickness of the gold nanoparticles.

## 3.5 Results

Having designed the geometry of the nanoparticles as well as their separation, we can now proceed to optimize the thicknesses of the layers constituting the PMC mirror. This can be accomplished using the equivalent network shown in Fig. 3.4. In order to maximize the conversion efficiency, we use the *Differentiated Meta Particle Swarm Optimization* (DMPSO) with democratic implementation in evolution of particles [150]. The optimizer adjusts the thicknesses of the first five layers (i.e. $t_1, \cdots, t_5$) and accordingly changes the scattering matrix $\overline{S}_M$ to maximize the first order enhancement factor $g^{(1)}(\lambda)$ defined as

$$g^{(1)}(\lambda) = \frac{\iint_{\text{unit cell}} \mathrm{d}x\mathrm{d}y \left|\mathbf{E}(x,y,z=0)\right|^2}{WL\left|E_0(\omega)\right|^2} \tag{3.10}$$

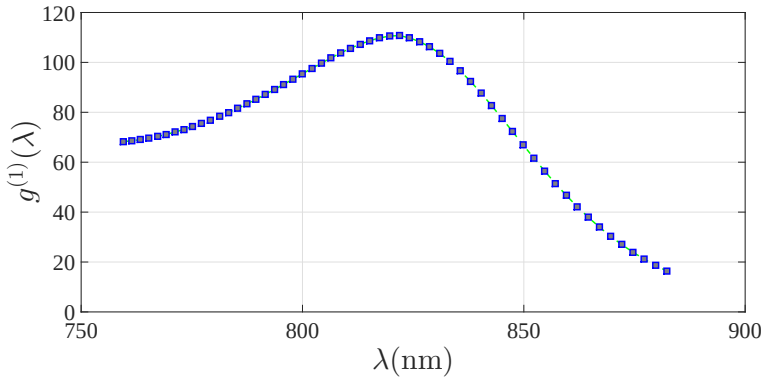


Figure 3.5: First order enhacement factor $g^{(1)}(\lambda)$ defined in equation (3.10).

where $\mathbf{E}(x, y, z = 0)$ is the electric field induced over the graphene layer at the fundamental frequency (wavelength of $\lambda$) and $E_0$ is the amplitude of the incident electric field illuminating the structure. As discussed in Section 3.3 , keeping the thicknesses $t_i$'s around integer multiples of $\lambda_i/4$ (where $\lambda_i$ is the wavelength at the fundamental frequency inside the i'th layer), guarantees dual-band performance of the PMC mirror at both fundamental wavelength $\lambda_0$ and its third harmonics $\lambda_0/3$. Accordingly, the optimizer finely adjusts $t_1$ around $\lambda_1/2$ and the other $t_i$'s around the quarter wave $\lambda_i/4$. In order to accelerate the optimization procedure, only a few number of Floquet modes are used to construct the scattering matrices. We pick up 25 Floquet modes with the indices $m, n = -2, \cdots, 2$ for both TE and TM polarizations. The values listed in table 3.1 were obtained after optimization for the thicknesses of the layers.

| $t_1$ | $t_2$ | $t_3$ | $t_4$ | $t_5$ | $t_i$ $(i > 5)$ |
|---|---|---|---|---|---|
| 220nm | 143nm | 105nm | 137nm | 123nm | $\lambda_i/4$ |

Table 3.1: Optimized thicknesses of the layers constituting the multilayer structure shown Fig. 3.3.

The resulted first order enhancement factor is shown is Fig. 3.5. The fast solver facilitates optimization of the structure and as a result the remarkable amount of plasmonic enhancement is achieved. The field distribution at the graphene layer as well as over the

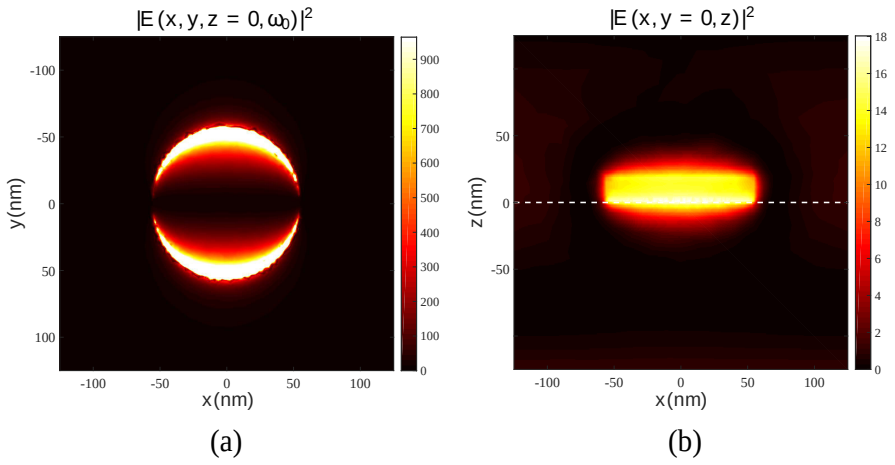


Figure 3.6: Linear electric field distribution at the frequnecy of $\omega_0$ obtained from FEM solver (a) at the graphene layer (b) over a vertical cross section ( $y = 0$ palne). The white dotted line shows the location of the graphene layer. The color map shows the squared magnitude of the induced electric field normalized to incident electric field.

vertical cross section are depicted in Fig. 3.6(a). The plasmon resonance leads to the high intensity of the field inside the nanoparticle as shown in Fig. 3.6(b).

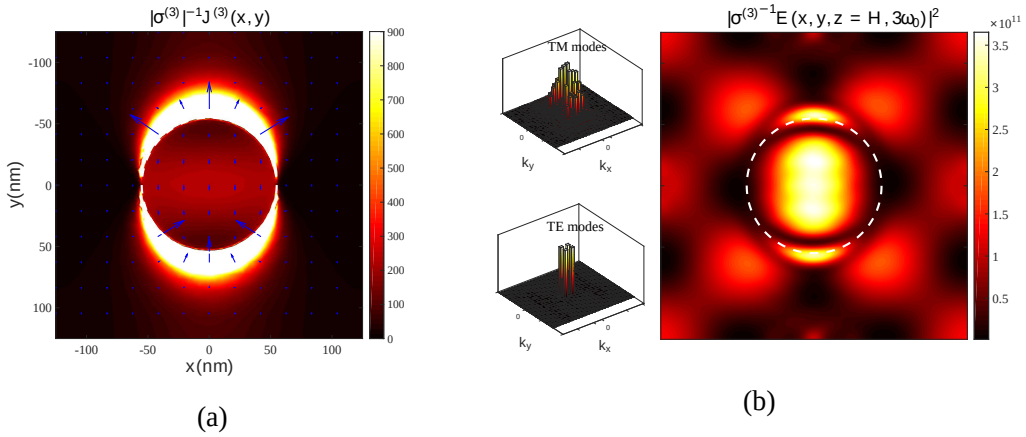


Figure 3.7: (a) Normalized current distribution oscillating at the angular frequency of $3\omega_0$. (b) Normalized electric field distribution on top of the nanoparticles and its modal coefficients. Current amplitude and the corresponding electric field are normalized to $\sigma^{(3)}(\omega, \omega, \omega)$ and it is assumed that the incident field has the magnitude of unity.

The field distribution at the fundamental frequency is plugged into equation (3.3) to find the third harmonic current induced on the graphene layer as the nonlinear medium. The normalized third harmonic current distribution is displayed in Fig. 3.7. This current acts as an impressed source radiating in the presence of the structure. The radiating field can then be obtained by calculating the field distribution on top of the nanoparticle array. This field distribution acts as a Huygens source and it corresponds to the voltage across the $AA'$ nodes in the equivalent network shown in Fig. 3.4. The field distribution and its spectral components obtained from the equivalent network are depicted in Fig. 3.7. Since the dimensions of the unit cell are chosen to be $W, L < \lambda_0/3$, among all the Floquet modes appearing in the modal expansion of the wave front, only the modes corresponding to $m = n = 0$ contribute to radiation and all other modes are evanescent.

The overall enhancement of the third harmonic power with respect to that of a bare graphene layer (i.e. the absence of the structure) is shown in Fig. 3.8. The dimensionless third order enhancement factor $g^{(3)}(\lambda)$ is defined as

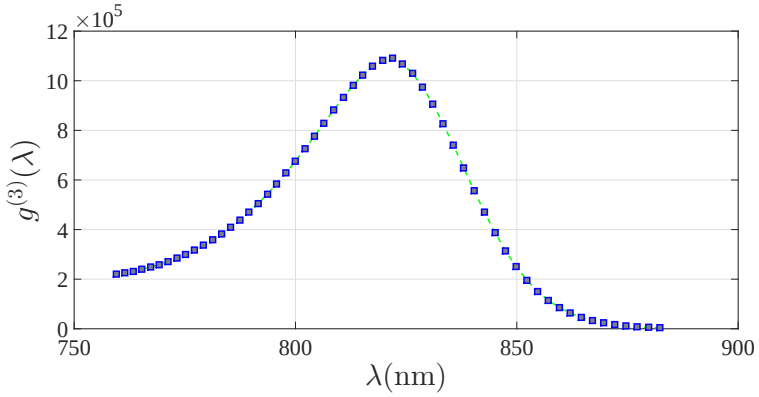


Figure 3.8: Dimensionless third order enhancement factor $g^{(3)}(\lambda)$ defined in equation (3.11).

$$g^{(3)}(\lambda) = \frac{P^{rad}(3\omega)}{P_0^{rad}(3\omega)} \tag{3.11}$$

where $\omega$ is the angular frequency corresponding to the wavelength $\lambda$. The powers $P^{rad}(3\omega)$ and $P_0^{rad}(3\omega)$ are the radiated powers at the third harmonics for the present structure and a bare graphene layer respectively. The power $P^{rad}(3\omega)$ has been calculated via the numerical method proposed in Section 3.4.

The significantly high amount of enhancement $g^{(3)}(\lambda) \sim 10^6$ achieved, makes third harmonic generation possible. The performance of the designed structure in the presence

of a femto-second laser pulse is also examined. The laser has the repetition rate of 86MHz, the centeral wavelength of 820nm and the pulse duration of $\tau = 150$fs. The input power launched to the set-up is assumed to be 1W with the focused spot size of $\sim 15\mu\text{m} \times 15\mu\text{m}$. The input signal in time domain and the third harmonic signal detected in the far field are shown in Fig. 3.9(a). As a result of the intensity-dependent conversion efficiency, the third-order pulse is narrower than the incident pulse. It is assumed that the graphene is biased to the Fermi energy level of $E_{F_0} \sim 700\text{meV} \sim \pi\hbar c/\lambda_0$ where $\lambda_0$ is the centeral wavelength of the laser (i.e. 820nm). The third harmonic output power is predicted to be $P_{out} \sim 1\mu W$ which corresponds to the the conversion efficiency of $\eta = 0.0001\%$. The amount of the third harmonic conversion efficiency is quite significant and is comparable to the most efficient subwavelength-scale frequency up-conversion experiments reported recently [151]. It is worth noting that the third harmonic power is proportional to the input (pump) power cubed (i.e. $P_{out} \propto P_{in}^3$) before the graphene layer get saturated and therefore, the conversion efficiency can be further enhanced for a larger pump power.

The dependence of the conversion efficiency with respect to the Fermi energy level of the graphene layer is shown in Fig. 3.9(b). As expected, the conversion efficiency is maximum when the graphene monolayer is biased to the Fermi energy level of $E_{F_0}$ corresponding to the resonance condition at the central wavelength. Because of the other quantum resonance in the nonlinear response of graphene, another peak at the Fermi energy level of $3E_{F_0}$ is expected. The suppression of the linear absorption of the graphene layer for the Fermi levels higher than $E_{F_0}$ also yields significantly higher conversion efficiency. However, as mentioned earlier, the Fermi energy level of $3E_{F_0}$ is too large to be realized. Fig. 3.9(b) displays the variations of the conversion efficiency within a reasonable range of Fermi energy level. The details of calculations are presented in Appendix F.

## 3.6 Conclusion

A design methodology for an efficient graphene based integrated plasmonic structure that enables third harmonic generation has been established in this chapter. More specifically, it has been shown that the nonlinear optical properties of graphene can be efficiently utilized for harmonic generation in a plasmonic structure made of a periodic array of shaped gold nanoparticles integrated with a multilayer topology. The gold nanoparticles provide extreme localization of the electromagnetic fields. The interaction of the plasmonic modes with the graphene is engineered by means of a multilayer structure. The multilayer structure has been designed to act as a dual-band PMC mirror working at the fundamental frequency and its third harmonic.

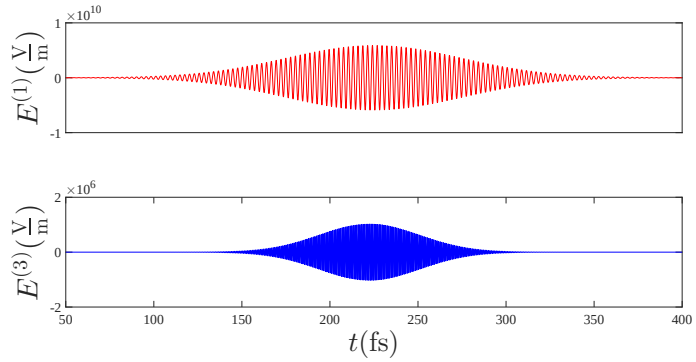


(a)

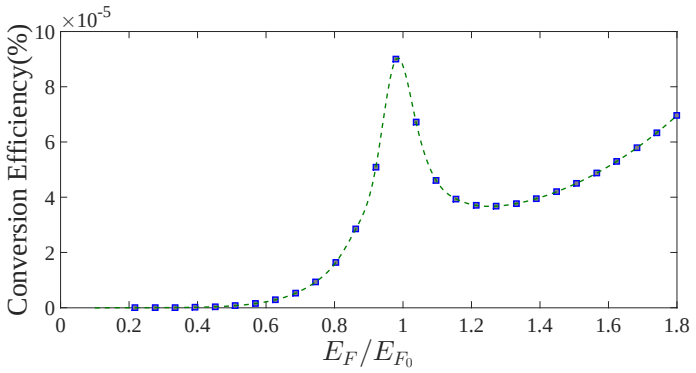


(b)

Figure 3.9: (a) Time variation of the pulse laser illuminating the graphene layer ($E^{(1)}$) at low temperature ($T \sim 0K$) and the third harmonic signal ($E^{(3)}$) detected in the far field (radiated field) (b) variations of the overall conversion efficiency with respect to the graphene's Fermi energy level normalized to resonant Fermi level $E_{F_0} = \hbar\omega_0/2$. The frequency $\omega_0 \equiv 820$nm is the central frequency of the laser beam. The pump power is 1W.

A novel hybrid numerical method combining the plane wave expansion and the Generalized Multipole Technique (GMT) to analyze and to optimize the structure wa proposed. The numerical method presents a circuit model for the structure. The circuit model allows us to separately optimize the distinct part of structure.

Applying this design procedure for a near infrared -UV converter as well as optimizing the structure through the circuit model developed here, the overall enhancement factor of $\sim 10^6$ over a wide range of frequency was achieved.

# Chapter 4

# Hybrid Graphene-Silicon Photonic Crystal Nanocavities for All-Optical Modulation

*Observing Nonlinear Optical Phenomena Through a Nano-Magnifier!*

## 4.1 Introduction

All-optical signal processing at nanoscale has become an emerging paradigm within the past few decades. Silicon is known as a noble material for integrated photonics [3, 133, 152]. However, despite of unprecedented successes in the development of silicon-based integrated photonics technology, the poor nonlinearity of silicon hinders the adoption of monolithic silicon devices for all-optical signal processing [10]. Apart from its weak optical nonlinearity, the band structure of silicon does not guarantee ultrafast recovery time in the presence of intense optical illuminations [14]. Future technology promises resource-efficient and ultra-high speed performance; all-optical schemes solely based on silicon may not be able to compete with their electronic and electro-optic counterparts.

Graphene and potentially the other two-dimensional (2D) materials can complement to silicon photonic technology by adding a substantial amount of nonlinearity over a wide spectral range [20–22, 34]. As discussed within the preceding chapters, owing to the reduced dimensionality and symmetries existing in its crystalline structure, graphene exhibits relatively strong optical nonlinearity. This strong optical nonlinearity is accompanied by

ultrafast electron dynamics as well as optical tunability. Although light-graphene interaction is relatively strong given its single atomic thickness, sophisticated field enhancement mechanisms are definitely required to exploit the exclusive nonlinear optical properties of graphene. The nascent practice of transferring graphene onto many optical structures, has already shown great promise for the efficient exploitation of graphene's unique optical properties. For instance, by incorporating a graphene layer along a high-Q photonic crystal nanocavity, a variety of nonlinear optical functionalities can be achieved [34, 38].

Among all functions required for integrated photonic circuits, the crucial role of optical modulation in optical signal processing is topmost [21]. The key figures of merit used to evaluate the performance of modulators are speed, operation band, insertion loss and power consumption [22]. Of these, modulation speed is considered as a decisive factor in efforts to meet the growing demand for information capacity.

According to the operational mechanism, optical modulators are classified into electro-optic, all-optical, magneto-optic, thermo-optic and so on [21]. Since the optical response of graphene can be tuned by applying a gate voltage, the development of electro-optical modulators based on graphene has been targeted by several groups [61–64]. Various schemes have been proposed to date, including graphene integrated waveguides as well as resonant structures whose optical transmissions are controlled by a gate voltage. The most distinctive performance feature of reported graphene modulators is their extremely broad operation band. Although graphene-based electro-optical modulators demonstrate competitive performance when compared with the state-of-the-art optical modulation platforms, their operational speed is limited by the RC time constant associated with the charge buildup on the graphene sheet [21, 64]. This electrical bottleneck on the modulation rate can be circumvented by an all-optical scheme [21].

All-optical modulation schemes employ a nonlinear material–whose optical properties vary under high intensity illumination– to control or redirect the flow of a beam of light that carries information. Borrowing the concept of pump-probe spectroscopy, a switch light (most often ultrafast pulses) changes the optical properties of the nonlinear material. The impact of the change on optical absorption or the refractive index of the nonlinear medium can be *augmented* through a resonant structure that provides high enough optical confinement. The majority of all-optical modulation devices exploit third-order optical processes including the saturable absorption or Kerr effect to optically control the flow of the signal beam.

While all-optical modulators and switches based on monolithic silicon technology have been demonstrated in different configurations [14, 153, 154], these devices require the use of extremely high-powered control beams to achieve high modulation depths. Although this

issue can be alleviated using ultra-high-Q resonant structures, limitations in the speed of such devices would remain an obstacle. The use of an ultra-high-Q structure will impose further limitations on the speed of the device due to the relatively long life-time of the photons stored inside the cavity. Several silicon-based all-optical modulators have been proposed [153, 154]. A typical value for operational speed of such a device is hundreds of picosecond [154]. Graphene's natural ability to function as a robust saturable absorber, via the phenomenon known as optically induced Pauli blocking, would render it possible to perform ultrafast all-optical modulation in hybrid graphene-silicon structures.

The innate flexibility of graphene has been exploited in Ref. [155] to wrap a graphene monolayer over a microfiber for all-optical modulation based on the saturable absorption of graphene. The operational principle of the proposed device is based on the absorption of light by the graphene layer. The absorption loss of the graphene is controlled by a high intensity pulse which in turn modulates the intensity of the *signal light* being guided by the microfiber. The experimental results demonstrate the superior performance of the device over the aforementioned electro-optical modulators in terms of operational speed. Response times of $\sim 2.2$ps have been reported; these are only limited by the intrinsic carrier relaxation time of graphene. However, the maximum modulation depth is limited to 38%. Since the fiber-based modulator proposed in Ref. [155], essentially takes advantage of guided modes and not resonant modes, no additional limitation is imposed by the life time of the photons being transmitted by the fiber. However, the poor performance of the device in terms of modulation depth effectively negates its ability to meet one of the key objectives of all-optical operations. Using optical Kerr effect instead of saturable absorption has been proposed recently [156]. S. Yu *et al.* demonstrated all-optical modulation in a graphene-cladded microfiber integerated with a Mach-Zehnder interferometer structure [156]. In the proposed device, the *signal* and *control* light pass through the graphene-cladded microfiber. The signal undergoes phase modulation caused by the optical Kerr effect in graphene. The phase-modulated signal light interferes with another path of light in the Mach-Zehnder interferometer to realize amplitude modulation. However, since the graphene layer is still lossy over the operational band, the structure suffers from an excessive amount of loss. There is always a trade off between overall transmission and modulation depth in guided based structures. To circumvent this issue resonant-based structures are proposed in this thesis.

This chapter presents the experimental demonstration of strong optical modulation effects in a graphene-cladded photonic crystal slab structure. The all-optical modulator that is being experimentally explored, is schematically illustrated in Fig. 4.1. The photonic crystal nanocavity was fabricated over a silicon membrane and a graphene monolayer was directly (without any spacer) transferred onto the cavity region. The cavity was formed by

displacing the holes around a line-defect waveguide. The resonance frequency of the cavity in the absence of the graphene was designed to be around $\lambda \sim 1550$nm. The considerations regarding the design of the photonic crystal nanocavity are extensively discussed in section 4.2. As is displayed in Fig. 4.1, a high intensity beam impinging on the cavity from the free space (shown in red) acts as the control beam. The control beam contains a train of ultrafast pulses of wavelength around $\lambda \approx 1064$nm. The operational principle is based on changing the resonance properties of the cavity in the presence of the graphene and by "deactivating the graphene monolayer " through saturable absorption. The pulse train is intended to control the transmission properties of a signal (shown by blue shading) guided through the line-defect waveguide.

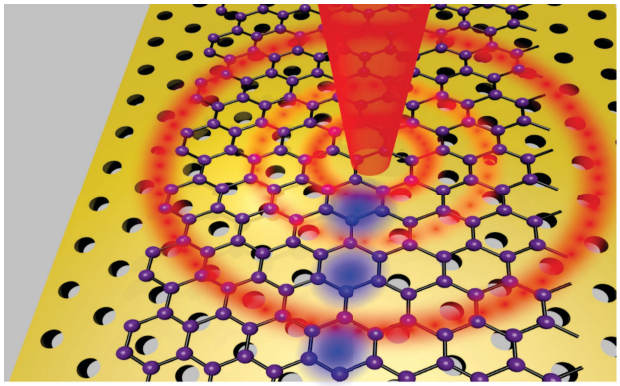

Figure 4.1: Schematic of proposed resonant-based graphene-cladded photonic crystal slab structure. All-Optical amplitude modulation in graphene-cladded photonic crystal heterostructure nanocavity. The red beam contains a train of ultrafast pulses that control resonance properties of a photonic crystal nanocavity.

The main focus of this chapter is twofold: First, the performance of the graphene-cladded photonic crystal structure (as a prototype for all-optical modulation) will be experimentally investigated. As the operational speed of the device is dictated by the relaxation dynamics of the graphene-silicon heterostructure, experimental exploration of the operational speed will be crucial. The experimental results demonstrate that graphene-silicon heterostructures offer both ultrafast and slow relaxation dynamics. The ultra-fast relaxation mechanisms originate from the carrier dynamics in graphene and the slow part of the dynamics stems from the charge injection into the silicon layer. Experimental exploration of the relaxation processes constitutes the second focus of this chapter. It will be argued that graphene-silicon heterostructures are an effective configuration for photoinduced doping in graphene.

This chapter is organized as follows. Section 4.2 is devoted to the design considerations of the photonic crystal structure used in the experiments.The experimental setup used to characterize the photonic crystal structures and the operational principles are discussed in Section 4.3. Section 4.4 presents the experimental results indicating strong all-optical modulation in graphene integrated photonic crystal nanocavities. The findings are summarized in Section 4.5.

## 4.2 Design of Photonic Crystal Double Heterostructure Nanocavity

Photonic crystal optical cavities are usually created by introducing a small defect or periodically modulated refractive index profile in either one, two or three dimensions [157]. The linear properties of photonic crystals including such defects have been extensively studied both theoretically and experimentally [158–160]. In particular, a defected periodic array of holes perforating an optically thin dielectric slab has been shown to be preferable for graphene integrated nonlinear optics. Apart from the ease of fabrication, a periodic array of holes supports *TE-like* modes in which the electric field tends to lie in the plane of the slab [157]. This type of polarization is desirable to enhance the light-graphene interaction. In such structures, the light is confined within the defect regions by combining the action of the Bragg reflections from the photonic bandgap structure within the plane of the slab and the total internal reflections in the vertical direction. Design of such optimal microcavities to enhance light-graphene interaction constitute the main focus of this section. The design of the photonic crystal slab structure is essentially a two-step process. First the slab dimensions are properly selected. Second, a strategic approach for formation of a high-Q cavity is taken. The design rule employed to realize the photonic crystal nanocavity is borrowed from Ref. [161].

### 4.2.1 Design of Photonic Crystal Slab

As mentioned above, TE-like modes are preferable for graphene-slab integration. The topology of photonic crystal slab structures is most often inspired by their two-dimensional counterparts. Imagine that the structure is infinitely extended along the third axis. An intuitive argument conceived based upon the variational principle implies that a complete bandgap for TE modes would exist in a 2D photonic crystal with circular holes perforating a dielectric medium. In such a structure, the holes are arranged in a hexagonal lattcie with

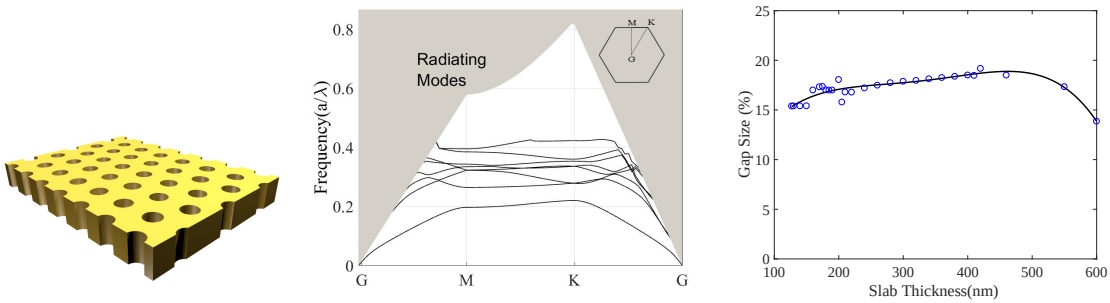


(a) (b) (c)

Figure 4.2: **Simulation:**(a) Photonic crystal slab and (b) its TE band structure. Shaded regions show the radiating modes. (c) Design curve to optimize the slab thickness ($a$ = 410nm).

the lattice vectors $\mathbf{a}_1 = a\hat{\mathbf{x}}$ and $\mathbf{a}_2 = a\left(\frac{\sqrt{3}}{2}\hat{\mathbf{x}} + \frac{1}{2}\hat{\mathbf{y}}\right)$ (where $|\mathbf{a}_1| = |\mathbf{a}_2| = a$). Seeking for the maximum bandgap size, the holes' radii for a silicon substrate are usually selected to be around $r \sim 0.3a$.

Borrowing the in-plane lattice topology from the two-dimensional bandgap structure designed for TE operation, it is possible to optimize the slab thickness. The photonic crystal slab is schematically depicted in Figs. 4.2(a). The existence of the optimal thickness can be intuitively understood by considering two extreme limits. If the slab is too thin, then it will provide only a weak perturbation on the background dielectric constant leading to weakly guided states, if they are guided at all. For a too thick slab, on the other hand, the higher order modes can be excited simply with little energy barrier. For a tall slab the fundamental mode is that of an infinite two dimensional structure, however, higher order modes can be pulled down by adding horizontal nodal planes [162]. Such modes will lie slightly above the low-lying mode, preventing any gap.

Using the variational principle, one can postulate that the optimal thickness will be on the order of half of the two-dimensional gap-bottom wavelength [162]. A rough estimate for the slab thickness is then obtained as

$$h \approx \frac{\pi c}{\sqrt{\varepsilon_{r,TE}^{eff}}\omega_{gap-bottom}} \tag{4.1}$$

where $\varepsilon_{r,T}^{eff}$ denotes the effective dielectric constant. Since the TE modes tend to confine within the slab region, the effective dielectric constant is fairly close to that of silicon.

The operational wavelength is intended to be around $\lambda_0 \sim 1550$nm and therefore the slab thickness should not be far from $h \sim 220$nm.

The band structure of the photonic crystal slab structure is plotted in Fig. 4.2(b). Clearly a band gap exists outside of radiation continuum. By selecting $a \approx 410$nm and $r \approx 108$nm, the designed operational wavelength would lie in the mid-gap region. It is worth pointing out that, due to technology limitations, the slab thickness cannot be arbitrarily selected. For instance, the commonly available silicon cores that are closest to the thickness required for the structure proposed here are 210nm or 260nm thick. Moreover, when localizing states in a resonance cavity, longer decay times can sometimes be achieved by using slightly thicker slabs [162]. In fact for thicker slabs the frequency is pulled down to where the density of the radiating modes is lower (the density of the radiating modes is proportional to $\omega^2$). Fig. 4.2(c) displays the variations of the gap size[1] versus the slab thickness[2]. The robustness of the gap size, provides more freedom to meet technology-imposed constraints as well as to further optimize the structure.

### 4.2.2 Photonic Crystal Double Heterostructure Nanocavity

High Q photonic crystal nanocavities are considered as hands-on solutions that enable nonlinear optics at the integrated level. Nonlinear effects obviously depend on the electric field strength inside the cavity. Field enhancement in the nanocavities is achieved essentially by squeezing the light inside the cavity as well as extending the lifetime of the photons stored in the cavity. Consequently, the field amplitude in the cavity should be inversely proportional to the mode volume $V_c$ and directly proportional to the photons' lifetime $\tau \sim Q/\omega_0$ (over which time the field builds up in the cavity). Unlike in other resonant structures, in a photonic crystal nanocavity, the mode volume is usually around $(\lambda/n)^3$ (n is the refractive index of the material constituting the slab structure ) and it is barely affected by the topology of the structure. The quality factor on the other hand, can be optimized to achieve highly narrow band operations. Recent extensive studies have demonstrated that a variety of architectures can minimize the radiation decay and maximize the quality factor of photonic crystal defected structures [160, 163].

As discussed above the photonic crystal cavities trap photons by exploiting two mechanisms ; total internal reflection (abbreviated as TIR) in the vertical direction and the Bragg reflection in the transverse direction. The Q of a cavity is determined by the energy loss per cycle versus the energy stored. Neglecting the absorption loss of the material

[1]Gap size is defined as the bandgap frequency length normalized by the center frequency.

[2]the band structure is analyzed using 'Crystal Wave' band solver

constituting the cavity, Q is thus determined by the reflection loss at the interface between the interior and exterior of the cavity. It is apparent that, fulfilment of the TIR condition in the vertical direction is crucial in designing high-Q cavities. To minimize any radiation leakage, abrupt changes in the field distribution over the cavity region must be avoided. Several strategies have been proposed to optimize the quality factor including the formation of a cavity by removing and displacing the holes and more recently width modulation of line-defect. The approach introduced in Ref. [161] has been taken in this thesis. The reason for this choice is twofold. First, the proposed structure has been shown to be less sensitive to fabrication imperfections [164]. The widely-employed linear three-hole defect cavities (known as L3 cavities) [165] are expected to be highly influenced by fabrication tolerances . Due to the experimental characterization method emaplyed in this work, the resonance wavelength in particular should be within a reasonable range. Second, it can be shown that the proposed design significantly increases the coupling strength of the optical mode to the graphene sheet compared to a conventional L3 cavity [165].

The proposed design for photonic crystal double-heterostructure nanocavity is shown in Fig. 4.3. The slab structure is composed of a triangular lattice structure with a line defect formed by missing a row of the air holes. The line defect supports waveguide modes within the bandgap. The cavity mode is formed by a slight change in the lattice constant over the cavity region. The labels I and II shown in Fig. 4.3 designate the original lattice (lattice constant $a$) and the deformed lattice (with the lattice constant $a'$), respectively. The presence of the cavity mode can be grasped by observing the bandgap structure associated with each region. The green shaded parts in Fig. 4.3(a) are the transmission part of the spectrum where a waveguide mode exists and photons can travel through the line defect. The red shaded parts indicate the mode gap region where transmission is forbidden. By deforming the lattice, the transmission and mode gap regions are slightly misaligned (with respect to the bandgap structure in region I) so that within a small part of spectrum a guided mode is supported by the deformed lattice and not by the original lattice. The mode is thus confined within a small region. By selecting $a = 410$nm and $a' = 420$nm, the resonance wavelength is expected to be around $\lambda \sim 1550$nm.

The proposed design offers optimum performance when the silicon layer (the photonic crystal slab) is suspended over air. However, since this thesis intends only to demonstrate the modulation effect discussed earlier, a structure composed of the device layer and a thick layer of $SiO_2$ underneath the silicon slab would be adequate for this purpose. The fabrication of such a device is of course less laborious and still provides the advantage of robustness of design with respect to fabrication imperfections. However, a significant degradation of the quality factor is expected. The structure has been simulated by a three

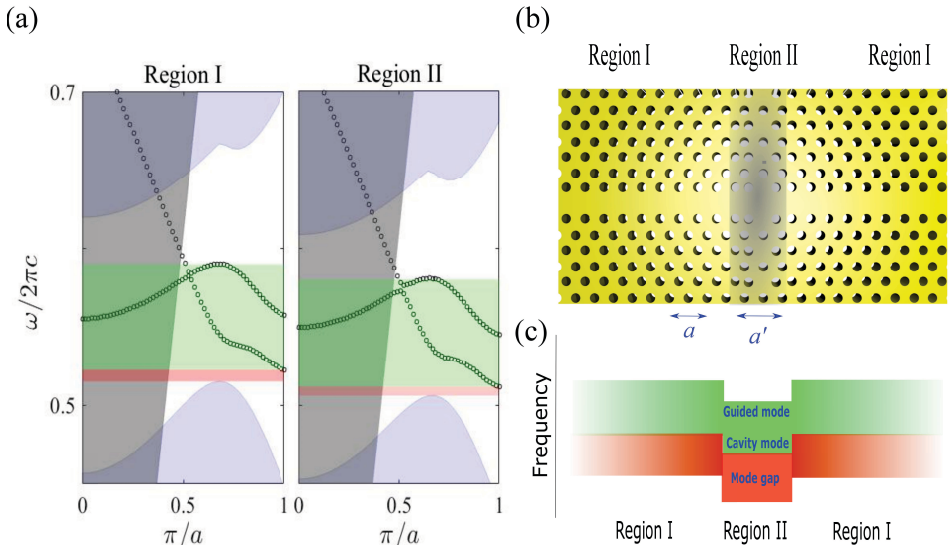


Figure 4.3: Design of double-heterostructure PHC nanocavity (a) **Simulation:** Band structure associated with the two lattices. Dark shaded region display the radiating modes inside the light cone. Dotted lines show the guided modes. Green shaded parts allow transmission through the guided modes and the red shaded regions are mode gap region where no guided modes exist. (b) Photonic crystal double heterostructure nanocavity formed by joining two lattice configurations. (c) Schematics of the band diagram along the waveguide direction.

dimensional (3D) FDTD solver[3] to find the resonane frequency, qulaity fcator and the mode shape. This was accomplished by exciting the cavity with two perpendicular small dipoles placed at the center of the cavity. The dipoles generate circularly polarized electromagnetic radiation with an almost uniform pattern. The electromagnetic field is recorded by two perpendicular sensors inside the cavity. Fig. 4.4 represents the response of the system in the spectral domain around the resonance frequency. The response peak takes place at the resonance frequency and its linewidth determines the quality factor. The resonance wavelength is $\lambda_0 = 1.579\mu$m and the corresponding Q factor is around $Q_0 \approx 6500$. The field intensity long after the other low-Q modes have died out is shown in the inset of Fig. 4.4. To gain insight into the impact of the $SiO_2$ layer, an analysis was performed for a photonic crystal membrane (without a supporting $SiO_2$ layer). As expected the quality factor of the membrane is significantly larger $Q_{\text{membrane}} \approx 1 \times 10^5$ and the resonance wavelength is $\lambda_{\text{membrane}} = 1.55\mu$m.

[3]Photon D, Crystal Wave module

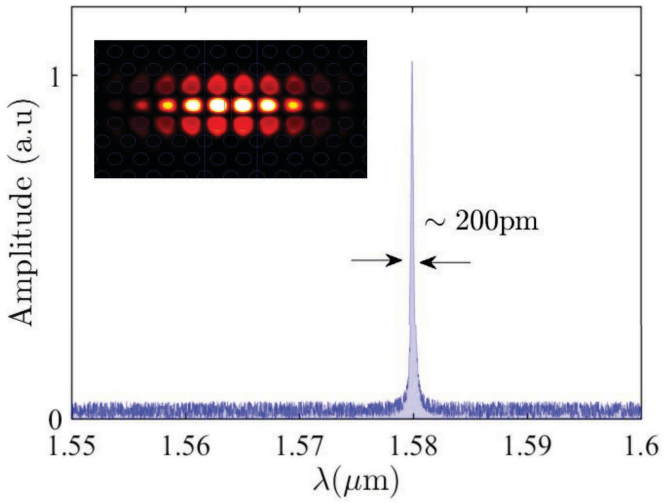


Figure 4.4: **Simulation Results:** Response of the double heterostructure nanocavity in the spectral domain around the resonance frequency. The mode shape is shown in the inset. The quality factor is $Q \approx \lambda/\Delta\lambda \approx 6500$ where $\Delta\lambda \approx 200$pm is the resonance linewidth.

The reason for this cavity having such a high quality factor can be intuitively understood as follows. The original line defect (in the absence of modulation) theoretically has ideal guided modes in the PhC without out-of-plane radiation loss. The guided mode is located outside of the radiation continuum. If we terminate this waveguide to form a cavity, this termination normally causes a large perturbation in the original mode profile, which results in a significant radiation loss for the cavity modes. With a mode-gap-cavity design (i.e. exploiting the band gap in waveguide modes) , the waveguide is not terminated but slightly modified to create a local modulation of the gap position. In this sense the mode is localized around the corresponding guided mode with minimum perturbation in k space and as a result the radiation loss is minimized.

### 4.2.3 Graphene-Cladded Photonic Crystal Double Heterostructure Nanocavity

Having designed the photonic crystal nanocavity, we can now proceed to investigate the resonance characteristics of the graphene-integrated photonic crystal nanocavity. Graphene is transferred onto the photonic crystal slab. The interaction of light and graphene obviously takes place through coupling with the localized mode in the photonic crystal nanocavity.

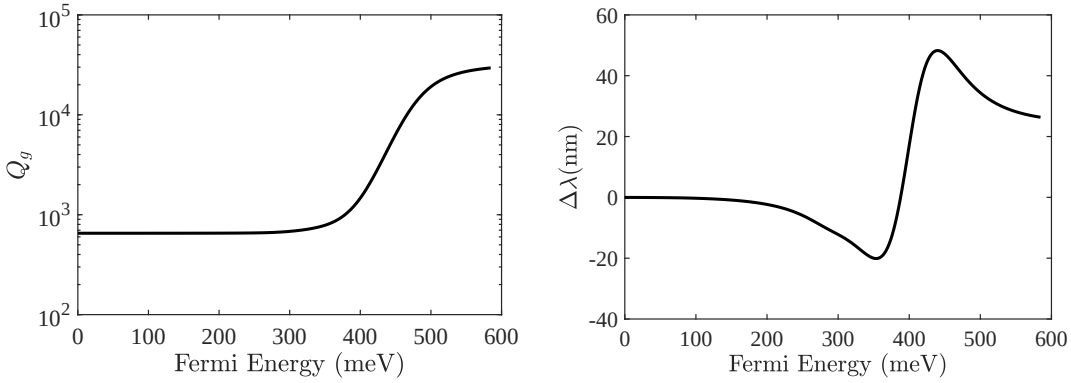


(a) (b)

Figure 4.5: **Theoretical Results:** (a) $Q_g$ versus Fermi energy level. The resonance frequency in the absence of graphene is $\hbar\omega_0 \approx 790\text{meV} \equiv 1550\text{nm}$. (b) Wavelength shift. The results are obtained from perturbation theory. Temperature is assumed to be $T = 300K$

Since a moderately-doped graphene sheet is absorptive –for the optical wavelengths–, a significant reduction of the quality factor is expected.

Subwavelength localization of the field in photonic crystal nanocavities leads to excitation of surface plasmons in graphene. Due to the strong confinement of the plasmons in the vertical direction, numerical modeling of graphene integrated nanocavities using domain discretization techniques (including FDTD) is expensive. The quality factor as well as the resonance shift of the cavity can be conveniently estimated by means of *open cavity perturbation theory* [166]. The reliability of the method is of course limited due to a certain lack of rigor, however insights can be gleaned from the results.

Given the complex resonance frequency defined as $\widetilde{\omega}_0 = \omega_0(1 + j/2Q_0)$ , where $\omega_0$ and $Q_0$ are the resonance frequency and intrinsic quality factor respectively, the variation of $\widetilde{\omega}_0$ caused by the graphene monolayer is calculated as

$$\delta\widetilde{\omega} \approx \frac{j}{4U_0} \iint_{\text{Graphene}} \mathbf{E}_0^*(\omega_0) \cdot \text{Re}\{\overline{\overline{\sigma}}_g\} \cdot \mathbf{E}_0(\omega_0) ds + \frac{\omega_0}{4U_0} \iint_{\text{Graphene}} \mathbf{E}_0^*(\omega_0) \cdot \text{Im}\{\frac{\partial\overline{\overline{\sigma}}_g}{\partial\omega}\} \cdot \mathbf{E}_0(\omega_0) ds \quad (4.2)$$

where the complex in-plane optical conductivity of graphene is denoted by the tensor

$\overline{\overline{\sigma}}_g$ and the vector field $\mathbf{E}_0(\omega_0)$ is the Fourier transform of the electric field at the resonance frequency. The factor $U_0$ is the total energy stored inside the cavity

$$U_0 = \frac{1}{2} \iiint \varepsilon_r \varepsilon_0 \left|\mathbf{E}\right|^2 d^3\mathbf{r} \tag{4.3}$$

In Eq. (4.2), the second term is obtained from the *Generalized Foster's Reactance Theorem* [167]. In the present formulation, an additional radiation loss arising from perturbing the field distribution by graphene has been safely neglected. It can be shown that the absorption loss is the dominant mechanism contributing to resonance broadening in the cavity. Eq. 4.2 allows identification of the intrinsic quality factor $Q_0$ (quality factor of the cavity in the absence of the graphene) and the quality factor associated with the graphene $Q_g = \frac{\omega_0}{2\mathrm{Im}\{\delta\widetilde{\omega}\}}$. The total $Q$ factor is calculated by

$$\frac{1}{Q} = \frac{1}{Q_0} + \frac{1}{Q_g} \tag{4.4}$$

If the fermi energy level allows absorption of the photons confined in the cavity, the quality factor $Q$ would be almost identical to $Q_g$. Fig. 4.5 displays the variations of the resonance wavelength as well as $Q_g$ versus the Fermi energy level.

Photonic crystal nanocavities were fabricated on a silicon-on-insulator wafer with a 260nm-thick silicon membrane using a combination of electron-beam lithography and dry/wet etching steps. A large-area, low-doped monolayer graphene grown by chemical vapor deposition (CVD) was wet transferred onto the silicon graphene directly without any spacer. The sample before and after transferring the graphene layer is shown in Fig. 4.6.

## 4.3 Experimental Characterization of Photonic Crystal Nanocavities Using Cross-polarized Reflectometry Setup

### 4.3.1 Optical Characterization Technique

The experimental characterization of the photonic crystal nanocavity was carried out by free-space illumination of a focused laser beam. The wavelength of the laser is scanned through the resonance of the photonic crystal cavity and the reflected beam is captured by an InGaAs detector equipped with a low noise amplifier. It is difficult to observe the

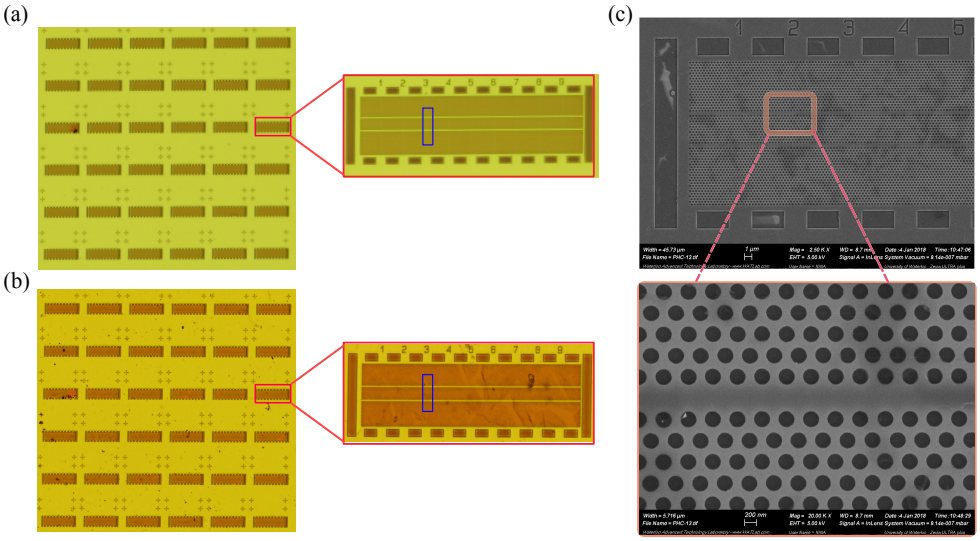


Figure 4.6: **Fabricated Device:** (a,b) Optical microscope images of photonic crystal double heterostructure nanocavity array. Each device containes eighteen equidistant cavities. (a) Bare photonic crystal sample (b) Graphene-cladded photonic crystal array. The cavity regions are marked by numbers. The blue boxes mark a pair of cavities. (c) Scanning electron microcopy image of the graphene-cladded photonic crystal. The dark regions are inhomogeneities in transferring graphene. The graphene layer is smoothly transfered onto the cavity.

cavity spectrum directly, because only a small fraction of the incident light couples to the high-Q cavity mode. The reflected beam predominantly comes from the device interface, which has no spectral dependence. Owing to the high quality factor of the cavity, the resonant mode has slight radiation leakage; According to the reciprocity theorem, the free space modes are barely coupled to the cavity mode. For that reason, the signal reflected by the cavity is monitored in the cross-polarization reflectometry setup.

The operation principle of the experimental setup used to measure the cavity spectrum is schematically illustrated in Fig. 4.7. It can be shown that, the cavity mode is dominantly $y$-polarized (see Fig. 4.7). A polarizing beam splitter couples the vertical polarization component of the incident beam. The coordinate system is selected so that the vertical polarization scheme points toward $x$ direction. A half-wave plate rotates the polarization of the beam by the angle of $2\theta$ where $\theta$ is the angle of the *fast axis* with respect to the $x$ axis shown in the figure. The tilted polarized beam is then focused on the nanocavity by means of a microscope objective. In order to avoid exciting the modes with large in-

plane wave-vector, the spot size can be relatively large ($20\mu m$ for instance). However, low noise operation would require employing a spatial filter at the output to get rid of the rays reflected back from the artifacts surrounding the cavities. If the cavity mode is excited, the reflected beam will gain a large cross-polarized component. The reflected beam is collected by the objective and passes through the $\lambda/2$-plate once more to be rotated back to the vertical-horizontal frame. Only, the horizontal component which corresponds to the cross-polarized term is coupled to the output through a polarizing beam splitter.

The orthogonal polarization configuration of the incident and detection light suppresses background reflectance which is mainly off the device layer. Therefore, not only can artifacts in the spectrum that do not originate in the nanocavity be largely avoided but the visibility of the mode of interest is maximized. For a further reduction of noise , a $10\mu$m pinhole was placed at an optically conjugate plane in front of the detector to eliminate the rays coming from the out-of-focus as well as the region surrounding the cavity. This technique was inspired from Confocal microscopy, originally invented in 1957 by Marvin Minsky [168].

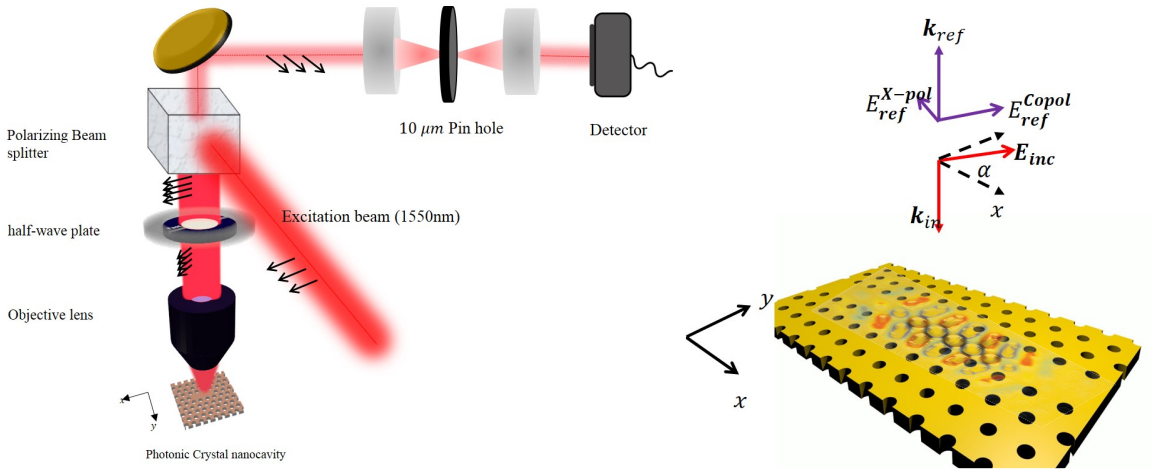


(a) (b)

Figure 4.7: (a) Schematic of cross-polarized confocal reflectometry setup. (b) Mathematical modeling of angle- dependence of the cross-polarized power

As remarked upon above, the cross-polarized component has a resonant nature and it thus provides an accurate way to measure the resonance frequency and quality factor of the excited mode. At the resonance wavelength, variations in the amount of the power coupled to the cross-polarized component versus the angle of the waveplate can be roughly

estimated. Although the calculations are overly simplistic, the resulted expression can accurately explain the experimental results. The amplitude of the resonant mode excited by the illuminating Gaussian beam is proportional to the spatial correlation of the mode shape and the incident electric field [169]. Assuming that the mode is dominantly $y$-polarized, the amplitude of the excited mode ($A_m$) accordingly should be proportional to $A_m \propto \sin(2\theta)$ where $\theta$ is the angle of the half-wave plate. The cross-polarized reflection $E_h$ in turn, is approximately proportional to the projection of the mode in the direction orthogonal to the incident wave [i.e. $E_h \propto A_m \cos(2\theta)$]. Combining the above, the angle-dependence of the cross-polarized power –denoted by $P_X$– is

$$P_X \propto |\sin 4\theta|^2 \tag{4.5}$$

Fig. 4.8 illustrates the schematic of the actual setup used to perform the resonance reflectometry measurements. In addition to the half-wave plate discussed above, the setup takes advantage of a quarter waveplate for precise alignment as well as IR imaging. The $\lambda/4$-plate facilitates the coupling of the co-polarized component to the output for alignment purposes. We have also employed two visible imaging systems namely incoherent and coherent. The incoherent imaging system aims us to search for photonic crystal over a wide sample. The coherent imaging system offers much higher resolution and it is utilized to find cavities over each photonic crystal. The IR imaging has been performed for both cross- and co-polarized configurations. The IR imaging camera employed in the setup (CAM3 in Fig. 4.8) is equipped with a square array of InGaAs detectors.

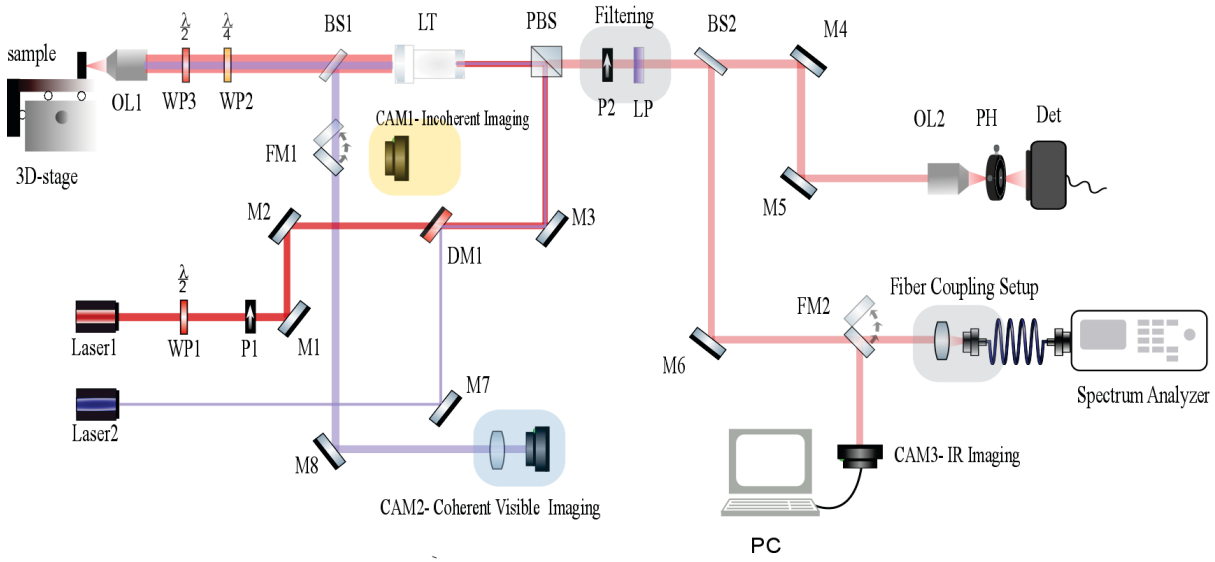


Figure 4.8: **Implemented Setup:** Cross-polarized confocal reflectometry setup. The red lines display the optical path for the $\sim$ 1550nm laser beam generated by the continuous tunable laser source (Laser1). The blue lines represent the visible laser beam (630nm in the actual experiment) generated by Laser 2. The IR beam is initially polarized; Therefore the $\lambda/2$-plate WP1 together with the polarizer P1 control the amount of the power injected into the setup. The polarizer P1 is adjusted to make sure that the beam is vertically polarized. Mirrors M1 and M2 are required to make the beam perfectly parallel to the optical table. DM1 is a dichroic mirror that allows transmission of the IR beam and reflects the visible beam. DM1 has been employed to make the IR and visible beams collinear. PBS is a polarizing beam splitter, which couples the vertically polarized beam to the sample. LT stands for Lens Tube. The lens tube is used to expand the beam to reach to the defraction limit (in terms of the spot size on the sample). In the experiment the lens tube has been designed to expand the IR beam twice is dimeter. BS1 is a beam sample which is used to couple the reflected visible beam to the CAM1 and CAM2 for incoherent and coherent imaging respectively. The $\lambda/4$-plate plate WP2 is employed to couple the vertically polarized beam to the output for alignment and IR-imaging purpose. The $\lambda/2$-plate WP3 is used to rotate the polarization of the incident beam. The objective lens OL1 focuses light on the cavity of interest. The 3D stage provides translation in x, y and z directions with micrometer precision as well as two extra degrees providing ability of rotating the sample. The Filter P2 is adjusted to filter out the vertically polarized beam and only transmits the horizontal components. The filter LP2 is long pass filter which allows transmission of the IR beam. BS2 is a beam splitter (sampler) which splits the beam at the output in two parts, one for detection and one for IR-imaging. OL2 is an objective lens to focus on the 10$\mu$m pinhole PH to filter out unwanted signals. The detector Det reads the cross-polarized signal. Precise coupling to the pin hole is achieved by mirror M4 and M5. The beams is partly coupled to IR camera to observe the cavity mode. A fiber coupled spectrum analyzer is also used to observe the spectrum of the cross-polarized component. FM1 and FM2 are flip mirrors.

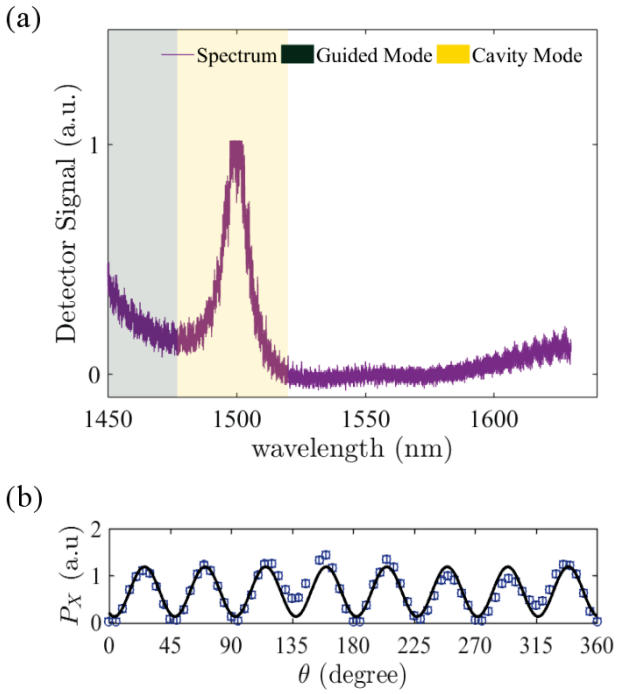


Figure 4.9: **Experimental Results:** Cross-polarized reflectometry measurements for the test cavity (a) cavity spectrum; yellow shaded region displays the resonant mode and green shaded part is the part of the spectrum that the photonic crystal supports guided mode and (b) at $\lambda = 1499$nm: variations of the cross-polarized power versus the angle of the $\lambda/2$-plate close to the sample. The black solid line is the best fitted sinusoidal function. It is observed that $P_X$ varies as $\sim |\sin 4\theta|^2$.

### 4.3.2 Experimental Results

The cross-polarized reflectometry measurements were carried out for two distinct samples. In the first experiment as a test run, the spectrum of a heterostructure nanocavity covered by a thin PMMA [4] layer, without graphene was measured. A tunable laser[5] covering the wavelength range of 1450nm − 1630nm was used as the source. Fig. 4.9 displays the measurement results. The variations of the cross-polarized power (which represent the cavity spectrum) are shown in Fig. 4.9.(a). The resonance peak takes place at $\lambda = 1499$nm.

[4] polymethyl methacrylate
[5] 8164B Lightwave Measurement System, Keysight

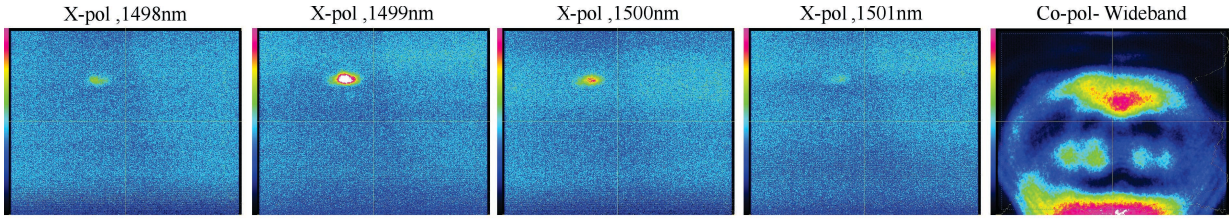


Figure 4.10: **Experimental Results:** IR imaging for the test sample (a)-(d) Cross-polarized imaging for the wavelengths $\lambda = 1498\text{nm}, 1499\text{nm}, 1500\text{nm}, 1501\text{nm}$ and (e) co-polarized imaging.

The relatively low quality factor of the cavity aimed us to adjust the setup and calibrate the polarizer and the waveplates. Fig. 4.9.(b) shows the variations of the power captured by the detector at the resonance wavelength versus the angle of the $\lambda/2$-plate WP3 (see Fig. 4.8). As expected, the variations of the power agree well with Eq. (4.5).

Two distinct parts of the spectrum are shaded in Fig. 4.9.(a). The yellow shaded region displays the cavity mode where the structure supports the resonant mode. The dark green shaded region is the part of the spectrum that the structure (both regions I and II of Fig. 4.3) supports waveguide mode within the line defect. Fig. 4.10 presents the results of IR imaging for the cross- and co-polarized configurations. In the cross-polarized configuration, the cavity mode is imaged at the resonance and it exhibits extreme wavelength dependence. The cavity is ON at the resonance frequency and as expected the cross-polarized components is bright only at the resonance wavelength. The co-polarized imaging has been performed with a wideband semiconductor laser[6]. The image is shown in Fig. 4.10.(e).

The resonance spectrum of the graphene-cladded double heterostructure nanocavity shown in Fig. 4.6, was measured next. This sample was selected to demonstrate all-optical modulation. The cross-polarized signal in the wavelength range of $1450\text{nm} - 1630\text{nm}$ is shown in Fig. 4.11. It is obviouse that, the structure possesses a wide linewidth around the designed wavelength (i.e. $\sim 1550\text{nm}$). The quality factor of this structure is around $Q \sim 100$ which is quite low. However, all-optical modulation can performed satisfactorily by this device. The variations of power captured by the detector in the cross-polarized configuration versus the angle of the plate at $\lambda = 1550\text{nm}$ were also recorded. The $\sim |\sin 4\theta|^2$ dependence indicates the resonant nature of the optical interaction.

[6]FPL1009S - 1550 nm, 100 mW, Butterfly Laser Diode, THORLABS

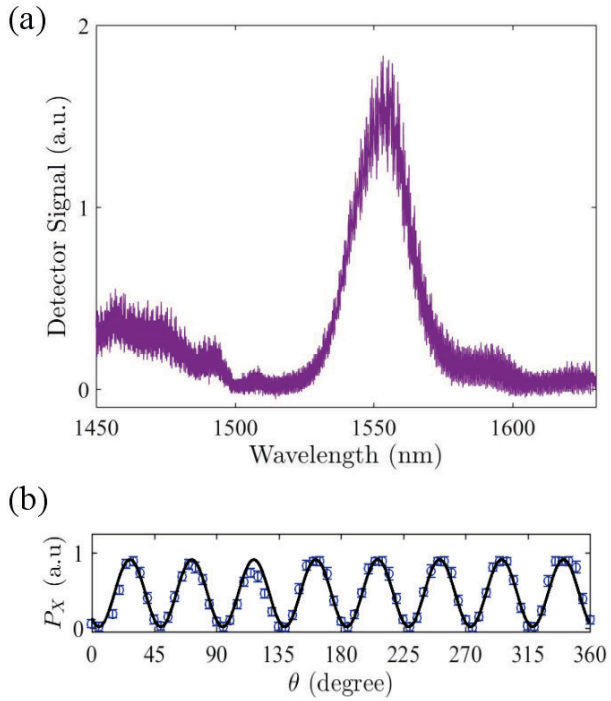


Figure 4.11: **Experimental Results:** (a) Resonance spectrum of the graphene-cladded photonic crystal shown in Fig. 4.6. (b) At $\lambda = 1550$nm: The variations of the cross-polarized power versus the angle of the $\lambda/2$-plate.

## 4.4 All-Optical Modulation

### 4.4.1 Operational Principles and Experimental Setup

As discussed extensively earlier, in the graphene-integrated double heterostructure nanocavity shown in Fig. 4.5, the TE-like resonant mode is evanescently coupled to the monolayer graphene. Absorption loss in the graphene sheet alters the resonance spectrum by reducing of the lifetime of the photons launched into the cavity. It has been observed that the graphene sample transferred onto the photonic crystal slab is absorptive in the optical wavelength range; therefore it should be moderately doped with a low-lying Fermi energy level. According to the results presented in Fig. 4.5, owing to the absorption loss in the graphene, a pronounced resonance broadening would be expected. In contrast, The

resonance shift, would be relatively small. The experimental results confirm this fact.

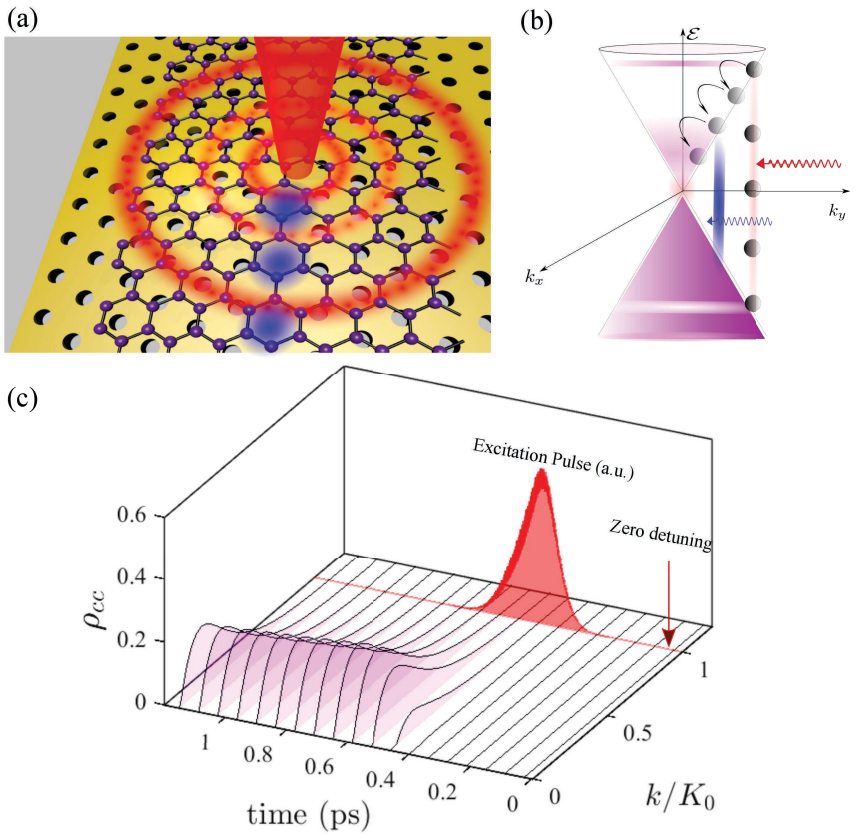


Figure 4.12: All-optical modulation via saturable absorption of graphene (a) **Schematic** of all optical-modulation in the graphene integrated photonic crystal cavity (b) **Schematic** of the electron dynamics underlying the modulation effect. An intense optical pulse (1064nm $\equiv$ 1.16eV) causes quasiparticles to jump to the conduction band. The carriers are then relaxed through electron-electron as well as phonon-assisted scattering processes to the lower energies. The probe light is stored inside the cavity (1550nm $\equiv$ 790meV) and experiences a modified population at the conduction band. (c) **Many-body Simulation:** Population of charged carriers in the conduction band ($\rho_{cc}$) versus Bloch wavenumber $k$ (with respect to the Dirac point, i.e. $k = 0$ is the Bloch momentum at the Dirac point), for several time slices. Excitation pulse in time (with an arbitrary unit) is displayed by the red shaded curve . Zero-detuning line where $\hbar\omega_{pulse} = 2\hbar v_F K_0$ is shown in the figure. Pump fluence is $12\mu\text{J/cm}^2$ with pulse duration of $\tau = 150$fs.

A schematic of the all-optical modulator is shown in Fig. 4.12(a). The photonic crystal

cavity is illuminated by a 1064nm ultrafast laser light (illustrated by the red beam). The ultrafast pulses were characterized by an intensity autocorrelation setup. The measurement results indicate that the duration of the pulses was around $\tau \approx 150$fs. The photon energy of 1064nm light is less than the band gap of silicon, so it can only be absorbed by the graphene. As is schematically illustrated in Fig. 4.12(b), the charged carriers in graphene jump into the upper energy level (conduction band) in the presence of high intensity illuminations and they relax to the lower energies (still within the conduction band) via many-body induced relaxation mechanisms. As a result, the population of the charged carrier in the upper energy level varies over time during and after applying the pulse and part of the optical transitions become prohibited due to Pauli-blocking. The reduced population difference in turn causes fewer photons trapped inside the cavity (with the wavelength of $\sim 1550$nm) to be absorbed by the graphene layer. This effect can be interpreted as optically modifying the Fermi energy level and changing the absorption spectrum of the cavity over the relaxation period of the carriers.

To further illustrate the saturation effect in graphene, a many-body analysis was performed encompassing all carrier-relaxation channels including Coulombic interactions and phonon-induced relaxation mechanisms[7] [114, 118] (details can be found in Appendix. B). The graphene layer is assumed to be undoped and is held at the room temperature. The temporal evolution of the pump-induced carrier occupation in the conduction band (denoted by $\rho_{cc}$) for the pulse fluence of $12\mu\text{J/cm}^2$ is depicted in Fig. 4.12(c). Carrier outscattering from the optically pumped states (denoted by the wavenumber $K_0$) leads to redistribution of the carriers over the conduction band in a picosecond time scale. It can be observed from Fig. 4.12(c), that the lower energies $k < K_0$ acquire nonzero carrier occupations. Consequently, the absorption of the low energy photons is quenched before carrier cooling is completed.

The experimental setup used to demonstrate all-optical modulation is displayed in Fig. 4.13. The pulse laser (acting as the control light) is generated by a Q-switch laser (Module #1) with repetition rate of 40MHz (i.e. the delay between two subsequent pulses is 25ns). The resonant cavity is probed through the cross-polarized reflectometry setup (Module #2) described in Section 4.3. The control and the probe beams are collinear and shine into the cavity from the top. Module #1 is designed to provide an arbitrary delay between two subsequent pulses. Inspired by the pump-probe spectroscopy technique, the control light is split into two parts and an arbitrary amount of delay is generated through a delay-line being adjusted by a translation stage. An optical chopper accompanied by a lock-in amplifier is employed to monitor the modulation effect. The control beam is chopped and the lock-in amplifier picks a portion of the cross-polarized signal (i.e. the resonant mode)

[7] In collaboration with Roland Jago, Ermin Malic, Chalmers University of Technology

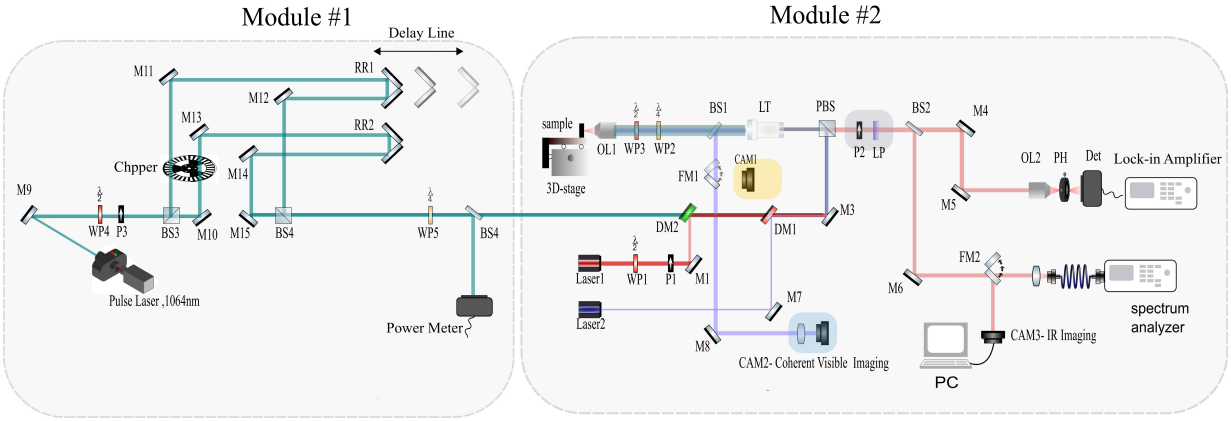


(a)

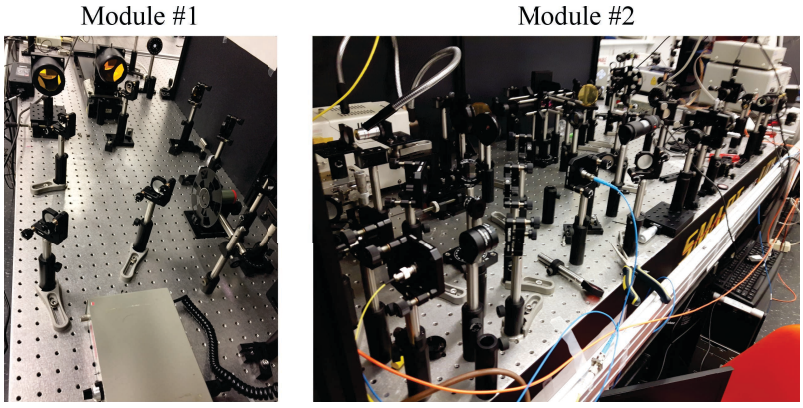


(b)

Figure 4.13: **Implemented Setup:** (a) Module #1 is to inject 1064 pulse train into the setup. Module #2 was explained in Fig. 4.8. The pulse train is generated by a Q-switched pulse laser with the center wavelength of 1064nm, the pulse duration of $\tau = 150$fs and repetition rate of 40MHz. The IR beam is initially polarized; Therefore the $\lambda/2$-plate WP4 together with the polarizer P3 cooperatively control the amount of the power injected into the setup. The separation between pulses are tuned by a delay line and a beam splitter. The beam is split in two parts by the beam splitter BS3. The delay line made of the retroreflector RR1 mounted on a translation stage can control separation between pulses. A second retroreflector is employed to balance the optical paths associated with each beam. A chopper with two types of holes is used to lock out the two beams with different frequencies. The two beams are recombined through the beam splitter BS4. The power injected to the setup is measured and calbrated by the power meter shown in the figure. Since the PBS in Module #2 only couples vertically polarzied beams into the sample, the $\lambda/4$-plate WP5 rotates the polarization to inject enough power into the sampel. (b) Implemented setup in our lab.

oscillating with the frequency determined by the chopper. This setup makes it possible to monitore the part of the signal being affected by the control beam .

### 4.4.2 Experimental Results

Fig. 4.14 presents the experimental results obtained from the optical arrangement described above. The red-shaded curves display the modulated signal captured by a lock-in amplifer. The measurement was performed for a variety of input powers (control light). Quoted power levels are the average power focused onto the sample through free-space illumination. Obviously, by increasing the power of the pulse laser, the saturation effect becomes more noticeable. For the input power of $\sim$ 120mW a complete saturation takes place. The cavity spectrum was simultaneously measured in the presence of high intensity illumination (blue-shaded curves). It is worth pointing out that due to the ultrafast recovery time of carriers, the modulation effect 'predominantly' occurs within a short time interval (only a few picoseconds). Therefore, the cross-polarized signal monitored by the detector is barely affected by the 1064nm laser beam. This necessitates using an optical chopper together with a lock-in amplifier to capture the small fraction of the signal (in time) being modulated by the ultrafast pulse laser. This observation does not imply that the modulation effect is small; given its resonant nature, the modulation depth can reach 100% in a picosecond time scale.

Our experimental observations indicate that there should be a slow relaxation mechanism attributable to carrier injection into the silicon layer. As will be clarified shortly, the graphene-silicon heterojunction prompts carrier injection into the silicon layer via slow carrier dynamics comparable to the time-separation between subsequent pulses. Apart from the non-equilibrium charge redistribution, the high intensity illumination is expected to vary the temperature of the graphene layer at equilibrium. The cooperative impact of the slow non-equilibrium charge injection and the equilibrium thermal effects leads to the slight changes in the cavity spectrum as the power increases.

The slight dependence of the cavity spectrum on the temperature rise, confirms that the Fermi energy level in the graphene layer (denoted by $E_f$) should be much lower than the energy of the photons confined inside the cavity. If $E_f \ll \frac{1}{2}\hbar\omega$ where $\hbar\omega \sim 790$meV, the absorption loss in the graphene would be minimally affected by any change to temperature.

To verify that the modulation effect is originating from the graphene, the experiment was also carried out with a bare photonic crystal nanocavity (without graphene) and no modulation effect was observed.

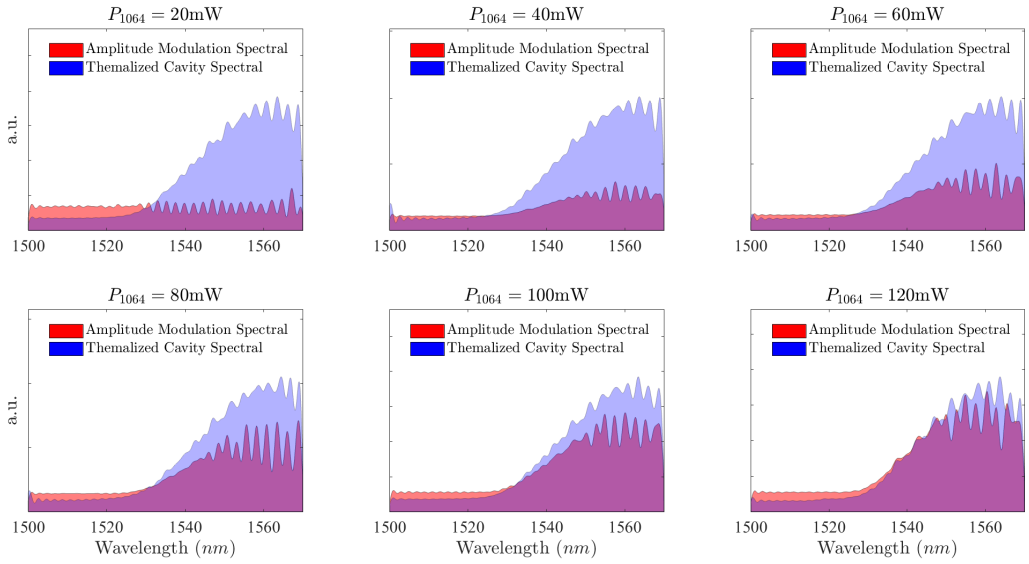


Figure 4.14: **Experimental Results:** Spectral dependence of modulation intensity. Red-shaded region is the spectral dependence of modulation depth (signal capture by lock-in amplifier in arbitrary units). Blue-shaded region is spectrum of the cavity in the presence of high intensity illumination.

Next, the impact of the slow relaxation dynamics was experimentally investigated. Since this effect is negligibly small , a pump-probe spectroscopic scheme would not be the most viable option. In order to verify the slow relaxation mechanism, the variation of modulation-depth versus power of the control beam was observed. If the photo-excited charge carriers survive in nanosecond time scale, '*communication*' would be instigated between subsequent ultrafast pulses that are separated by $\sim 25$ns. To further understand this, let us assume two subsequent ultrafast pulses being shot to the structure. The first pulse redistributes the carriers via the cooperative impact of the ultrafast and the slow relaxation mechanisms. The subsequent pulse would impinge upon the remaining carriers that are still undergoing relaxation beyond the time separation between the pulses. As a result, the modulation intensity is expected to carry a memory. That is, the modulation effect created by a given pulse should depend on the laser irradiation prior to that pulse.

Fig. 4.15 displays the modulation intensity versus average power of the control beam. The input power has been steadily swept within a closed loop. A slow sweeping of the input power guaranties thermal equilibrium in the presence of intense illumination. It is quite interesting that the modulation-depth follows a hysteresis loop. The high- and

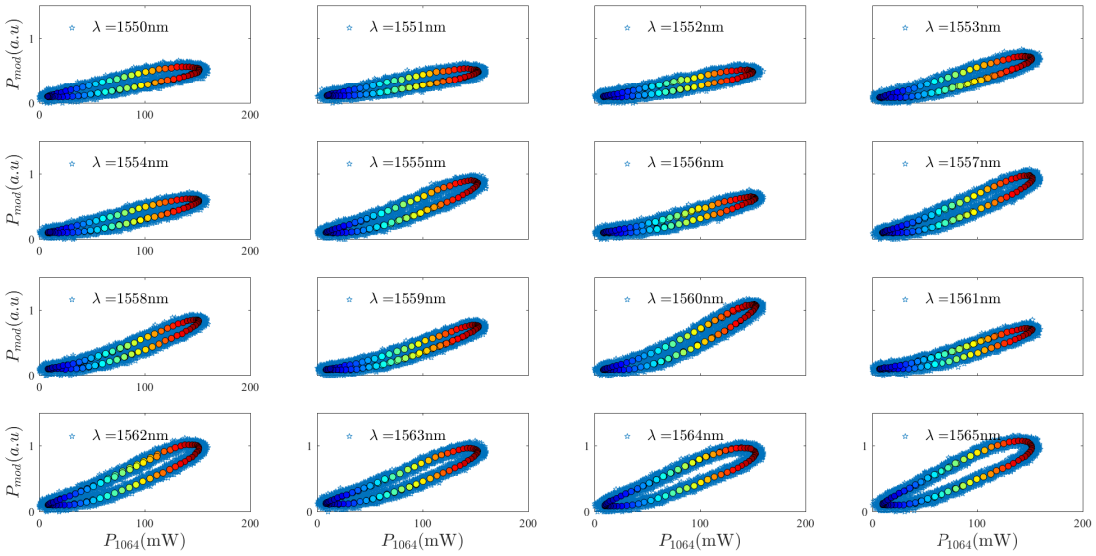


Figure 4.15: **Experimental Results:** Mapping of modulation-depth ($P_{mod}$) versus the power of the control beam ($P_{1064}$). Hysteresis behavior which can be attributed to the slow relaxation dynamics.

low-state modulations are illustrated in Fig. 4.15. The hysteresis loops indicate that the modulation-depth carries memory with respect to the control beam.

It is speculated that this effect can be attributed to carrier injection into the silicon layer through the graphene-silicon heterojunction. With the pulse laser on, the photo-excited electrons in graphene are partly transferred into silicon and this causes the un-occupied states in the valence band of graphene to go down gradually. The excess free electrons transferred into the silicon structure create extra amount of loss in the cavity region [170]. This extra amount of loss would compete with the optically-induced transparency in graphene to change the resonance spectrum of the hybrid cavity. It should be emphasized that the 1064nm pulse-train is weakly absorbed by silicon without graphene. The absorption coefficient of silicon for 1064nm light is reported to be $\alpha \approx 11\text{cm}^{-1}$ which is quite small and it does not give rise to any significant effect [171, 172].

The adopted physical picture can also explain *photo-induced doping* in graphene-silicon Schottky structures [173–175]. Motivated by potential applications of photo-induced doping in solar cells and energy harvesting, the electrical and photoelectrical properties of graphene-silicon heterojunctions have been characterized by several groups [173, 174]. Ex-

perimental results supported by theoretical studies, confirm that the Raman spectra of graphene-silicon heterojunctions are changed (mostly downshifted) by light irradiation [173]. The band configuration of the hybrid structure can be inferred from the experimental observations reported in Refs. [173]. In this work we do not plunge into a rigorous analysis of the effect and a qualitative explanation of the physical process underlying the experimental results should suffice, given the scope of this thesis work.

Fig. 4.16 schematically displays the energy diagram of a graphene-silicon heterojunction. The quality factor drop-off due to the free carriers injected into the silicon cavity depends on several factors including the free carrier absorption (denoted by $\alpha_{FCA}$) in silicon and the free carrier concentration [172]. The free carrier absorption coefficient in silicon probed by 1550nm light is estimated to be around $\alpha_{FCA} \sim 1.4 \times 10^{-17} N$ where $N$ is the free carrier concentration of silicon [176]. The light-induced carrier injection from the graphene to the silicon would lead to a charge accumulation over the interface. However, equilibrium is attained due to an electrostatic field build-up at the interface. The relaxation process is quite slow so that the graphene-silicon heterostructure exhibits non-memory-less behavior in the presence of coherent pulse irradiation.

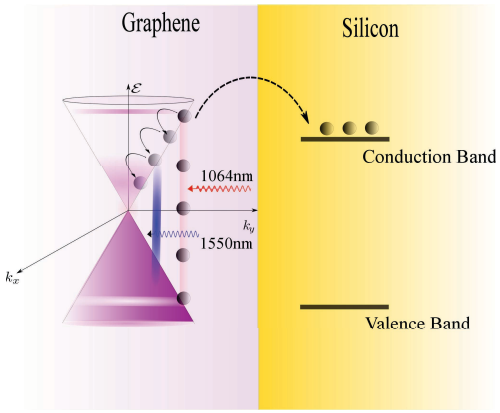


Figure 4.16: Energy diagram of graphene-silicon heterojunctions. Graphene injects the photo-excited carriers into the conduction band of silicon.

## 4.5 Summary

All-optical modulation in a graphene-integrated photonic crystal double heterostructure nanocavity has been demonstrated experimentally for the first time. A high intensity

pulse laser beam can effectively control the resonance spectrum of a graphene-cladded photonic crystal nanocavity via saturable absorption. The graphene layer absorbs the photons confined inside the cavity through interband transitions and the cavity brightness is thus reduced. The control pulse can redistribute the quasiparticles in graphene so that absorption quenching takes place. As a result, the resonance spectrum of the cavity is manipulated by the external pulse-train impinging onto the structure. Cavity brightness is thus controlled by the pulse-train via Pauli-blocking the optical transitions.

The optical characterization method employed in this work enables the capture of both ultrafast and slow relaxation mechanisms. The spectral dependence of the modulation depth was experimentally investigated. It was concluded that, the modulation depth follows the cavity spectrum. This observation is expected, since the modulation mechanism is based on the change in the cavity spectrum.

It was experimentally demonstrated that the modulation depth exhibits a discernible two-state dependence on the power of the control pulse. Since the optical structure does not provide any platform to trap the modulating pulses (i.e. 1064nm pulse-train), the non-memory-less state of the system is attributed to the slow carrier relaxation channels. It was argued that slow carrier injection from the graphene into the silicon layer competes with the ultrafast relaxation processes in the graphene to change the resonance spectrum of the cavity. This observation suggests that graphene-silicon heterostructures could be efficiently employed in energy-harvesting and related applications including solar cells.

The experimental observations presented in this chapter suggest that the integration of graphene with state-of-the-art optical platforms including photonic crystal structures can efficiently enable several nonlinear optical functionalities. In particular, graphene transferred onto a wavelength-scale nanocavity can significantly enhance the nonlinear effects , suggesting a new paradigm for chip-scale photonics and ultrafast optics for all-optical signal processing.

# Chapter 5

# Conclusion and Outlook

This thesis work undertook a combination of theoretical modeling, numerical analysis and experimentation. Although the nature of the concepts studied in this thesis did not allow for the verification of every theoretical extrapolation by experimentations, overal satisfactory rate of agreement between the predictions made and experimental observations was achieved. A summary of original contributions reported in this thesis are outlined in Section 5.1. Suggested areas for future work are discussed in Section 5.2.

## 5.1 Summary of Contributions

In Chapter 2, a comprehensive quantum theory of light-graphene interaction was developed. The adopted mathematical method allowed for the identification of the distinct nonlinear processes contributing to the third-order optical response of graphene. It was theoretically proved that the chirality of quasiparticles entails a diverging field induced interband coupling. Since this singularity has a physical origin, its impact was shown to be observable. It was argued that the anomalous structure of the interband coupling causes the charge carrier to undergo ultrafast Rabi oscillations accompanied by slow relaxation dynamics. As a result, even under arbitrarily weak electromagnetic radiation, low energy quasiparticles become optically saturated. It was claimed, for the first time, that optical response of graphene is in essence nonperturbative. In particular, for small Fermi energy levels or low-energy excitations, this effect is quite significant and therefore defining 'nonlinear coefficients' is no longer valid.

Luckily, for moderately doped graphene, the Kerr coefficient can be still defined within the optical wavelength range. The results of our experimental characterization of the

intensity-dependent refractive index of graphene was presented. Propitiously, both in terms of spectral dependence and orders of magnitude, the theoretical predictions successfully explained the experimental results.

In Chapter 3, a novel graphene integerated plasmonic structure for THG was proposed and numerically analyzed. To this end, the formulations developed in Chapter 3 were employed. The proposed structure was shown to exhibit competitive performance among state-of-the-art integrated nonlinear devices.

Along with the main purpose of Chapter 3, a novel topology was proposed to maximize the interaction of plasmon-enhanced fields and graphene. Since graphene only interacts with the part of the electromagnetic field whose polarization is parallel to the graphene sheet, enhancement of the magnitude is not necessarily enough. It was demonstrated that the integration of a plasmonic nanostructure and a multilayer Bragg reflector –which mimic a perfect magnetic conductor– could not only intensify the field , but would rotate the polarization of the enhanced field to improve the light-graphene interaction. This was accomplished by means of a novel numerical method which combines the GMT method and the plane wave expansion technique.

In Chapter 4, a new experimental demonstration of all-optical modulation in a graphene integrated photonic crystal nanocavity was presented. Using confocal cross-polarized reflectometry technique, the resonance spectrum of a cavity covered with graphene was characterized. It was experimentally confirmed that, the cavity spectrum varies in the presence of high intensity illuminations. This observation indicates that the graphene-cladded photonic crystal nanocavity can execute all-optical modulation via photoexcited carriers in graphene in the presence of ultrafast pulses. In addition, the experimental results indicate that carrier injection in the graphene-silicon heterostructure also partly contribute to the modulation effect. This effect introduces a slow process.

A sumamry of the contributions are listed below.

- **Theoretical development:** comprehensive semiclassical theory of light-graphene interaction leading to explicit expression for nonlinear optical response of graphene.
- **Theoretical development:** theory of spontaneous optical saturation of low-energy Dirac fermions.
- **Experimental characterization:** spectral dependence of the Kerr coefficient of graphene.
- **Proposed structure:** efficient optical third harmonic generation in a graphene-integrated plasmonic structure.

- **New numerical method:** hybrid numerical method; a combination of of boundary discretization method and plane wave expansion technique.
- **Experimental demonstration:** All-optical modulation in graphene integrated double heterostructure nanocavity.

## 5.2 Outlook

### 5.2.1 Two-Color Pump-Probe Spectroscopy

The pump-probe time-resolved spectroscopy technique can be used to obtain information on ultrafast phenomena. In this technique, a sample is hit by a pump pulse that modifies its refractive index via photo-excited carriers. After an adjustable time delay, a probe pulse impinges onto the sample, and its transmission or reflection is measured. By monitoring the reflected (or transmitted) probe signal as a function of the time delay, it is possible to obtain information on the decay of the carrier, and/or other processes initiated by the pump pulses. The probe signal is typically averaged over many pulses, and a fast photodetector is not required. The temporal resolution is fundamentally limited only by the pulse duration of the pump and probe pulses.

In commonly available pump-probe setups, a pulse laser beam is split into a high intensity pump and a low intensity probe. Since the two generated beams have identical origins, they are synchronous in time and an arbitrary amount of delay between the pump and probe pulses can be introduced by means of a spatial delay-line. Obviously, pump and probe have identical spectral distributions. However, in many applications, the pump and probe pulses are required to be at different wavelengths (i.e. two colors) to extract particular information; therefore two different lasers should be utilized. The most important requirement to perform pump-probe measurement is the synchronization of the pump and probe pulse trains. To date, several strategies have been introduced in the literature. The use of nonlinear crystals for second harmonic generation, external cavity lasers and electro-optical modulators are among the proposed techniques [177–179]. These techniques usually impose limitations on the wavelengths of the pump and probe and are highly complicated.

The performance of the graphene-cladded photonic crystal nanocavity was successfully demonstrated in Chapter 4. Since the modulation effect is predominately executed through the ultrafast carrier relaxation dynamics of the graphene, the modulated signal is expected to acquire a pulse shape with a picosecond-scale pulse width. Obviously, the pulse is oscillatory at the wavelength of 1550nm and is synchronous with the 1064nm modulating

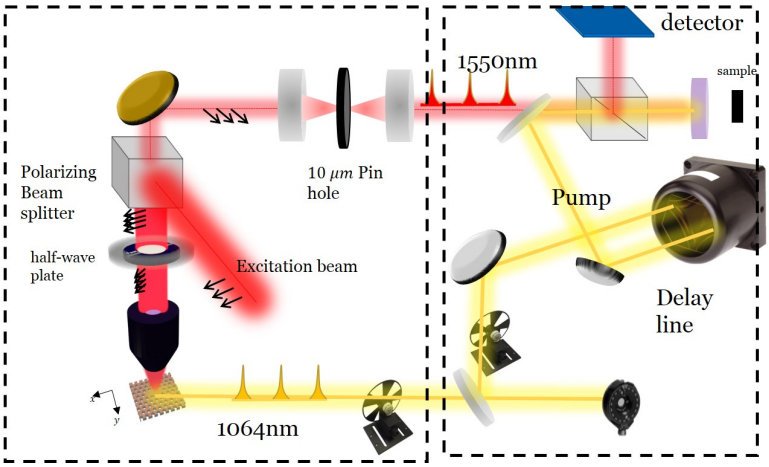


Figure 5.1: Schematics of two-color pump-probe spectroscopy technique based on all-optical modulation.

pulse train. A suggested direction for future experimental development, is to use the two synchronized beams (i.e the original pulse train that modulates the cavity and the modulated signal) to perform two-color pump probe spectroscopy. The proposed scheme is illustrated in Fig. 5.1. The proposed method offers several advantages over commonly used approaches. First, it is extremely simple and low cost. Second, the cavities can be designed to conduct pump-probe spectroscopy at arbitrary wavelengths. Third, due to the ultrafast carrier relaxation dynamics of graphene, the pulse width remains still quite small providing a reasonable resolution in time.

### 5.2.2 Optical Bistability in Graphene-Cladded Photonic Crysal Nanocavity

In Chapter 4, it was demonstrated that the exceptional third-order optical nonlinearity of graphene can add a substantial amount of nonlinearity to a wavelength-scale photonic crystal nanocavity. Hybrid graphene-silicon photonic crystal nanocavities can serve as an efficient platform for all-optical operations. In the all-optical modulation device investigated in Chapter 4, the saturable absorption of graphene was utilized to execute modulation. It would be even more stimulating to harness the nonlinear refractive index of graphene to perform all-optical switching in a fully integrated fashion. However, the implementation of such devices is challenging. All-optical switching would require using ultra-high-Q nanocavities to observe a bistable response. Due to the absorption loss of graphene over

the optical wavelengths, the quality factor of a cavity covered with graphene significantly drops. However, this problem can circumvented by electrical gating of the graphene sheet.

According to the results of the quantum mechanical calculations presented in Chapter 2, the Kerr coefficient of graphene peaks around $\hbar\omega \sim E_f$ (see Fig 2.9(a)). Luckily, the graphene is barely absorptive for the photon energies below $2E_f$ (i.e $\hbar\omega < 2E_f$). This essentially implies that, if the Fermi energy level of graphene is lifted up by applying a gate volage, the Kerr coefficient would increase and the quality factor of the cavity would still remain high. This in turn results in a unique optical bistabale device with ultra-low switching power.

# References


[1] S. M. Hendrickson, A. C. Foster, R. M. Camacho, and B. D. Clader, "Integrated nonlinear photonics: emerging applications and ongoing challenges [invited]," *Journal of the Optical Society of America B*, vol. 31, no. 12, p. 3193, nov 2014. [Online]. Available: https://doi.org/10.1364/josab.31.003193

[2] C. R. Pollock and M. Lipson, *Integrated photonics*. Springer, 2003, vol. 20, no. 25.

[3] R. Soref, "The past, present, and future of silicon photonics," *IEEE Journal of Selected Topics in Quantum Electronics*, vol. 12, no. 6, pp. 1678–1687, nov 2006. [Online]. Available: https://doi.org/10.1109/jstqe.2006.883151

[4] Y. Taur, D. Buchanan, W. Chen, D. Frank, K. Ismail, S.-H. Lo, G. Sai-Halasz, R. Viswanathan, H.-J. Wann, S. Wind, and H.-S. Wong, "CMOS scaling into the nanometer regime," *Proceedings of the IEEE*, vol. 85, no. 4, pp. 486–504, apr 1997. [Online]. Available: https://doi.org/10.1109/5.573737

[5] B. Jalali and S. Fathpour, "Silicon photonics," *J. Lightwave Technol.*, vol. 24, no. 12, pp. 4600–4615, Dec 2006. [Online]. Available: http://jlt.osa.org/abstract.cfm?URI=jlt-24-12-4600

[6] R. S. Tucker, "The role of optics and electronics in high-capacity routers," *Journal of Lightwave Technology*, vol. 24, no. 12, pp. 4655–4673, dec 2006. [Online]. Available: https://doi.org/10.1109/jlt.2006.885774

[7] H. J. Dorren, N. Calabretta, and O. Raz, "Scaling all-optical packet routers: how much buffering is required?" *Journal of Optical Networking*, vol. 7, no. 11, p. 936, oct 2008. [Online]. Available: https://doi.org/10.1364/jon.7.000936

[8] K. Liu, S. Sun, A. Majumdar, and V. J. Sorger, "Fundamental scaling laws in nanophotonics," *Scientific Reports*, vol. 6, no. 1, nov 2016. [Online]. Available: https://doi.org/10.1038/srep37419

[9] T. Volz, A. Reinhard, M. Winger, A. Badolato, K. J. Hennessy, E. L. Hu, and A. Imamoğlu, "Ultrafast all-optical switching by single photons," *Nature Photonics*, vol. 6, no. 9, pp. 605–609, aug 2012. [Online]. Available: https://doi.org/10.1038/nphoton.2012.181

[10] J. Leuthold, C. Koos, and W. Freude, "Nonlinear silicon photonics," *Nature Photonics*, vol. 4, no. 8, pp. 535–544, jul 2010. [Online]. Available: https://doi.org/10.1038/nphoton.2010.185

[11] E. Yablonovitch, "Photonic crystals: semiconductors of light," *Scientific American*, vol. 285, no. 6, pp. 46–55, 2001.

[12] T. F. Krauss, "Planar photonic crystal waveguide devices for integrated optics," *physica status solidi (a)*, vol. 197, no. 3, pp. 688–702, jun 2003. [Online]. Available: https://doi.org/10.1002/pssa.200303117

[13] M. Soljačić, C. Luo, J. D. Joannopoulos, and S. Fan, "Nonlinear photonic crystal microdevices for optical integration," *Optics Letters*, vol. 28, no. 8, p. 637, apr 2003. [Online]. Available: https://doi.org/10.1364/ol.28.000637

[14] V. R. Almeida, C. A. Barrios, R. R. Panepucci, and M. Lipson, "All-optical control of light on a silicon chip," *Nature*, vol. 431, no. 7012, pp. 1081–1084, oct 2004. [Online]. Available: https://doi.org/10.1038/nature02921

[15] K. Nozaki, T. Tanabe, A. Shinya, S. Matsuo, T. Sato, H. Taniyama, and M. Notomi, "Sub-femtojoule all-optical switching using a photonic-crystal nanocavity," *Nature Photonics*, vol. 4, no. 7, pp. 477–483, may 2010. [Online]. Available: https://doi.org/10.1038/nphoton.2010.89

[16] A. H. Safavi-Naeini, T. P. M. Alegre, J. Chan, M. Eichenfield, M. Winger, Q. Lin, J. T. Hill, D. E. Chang, and O. Painter, "Electromagnetically induced transparency and slow light with optomechanics," *Nature*, vol. 472, no. 7341, pp. 69–73, mar 2011. [Online]. Available: https://doi.org/10.1038/nature09933

[17] M. Bajcsy, S. Hofferberth, V. Balic, T. Peyronel, M. Hafezi, A. S. Zibrov, V. Vuletic, and M. D. Lukin, "Efficient all-optical switching using slow light within a hollow fiber," *Physical Review Letters*, vol. 102, no. 20, may 2009. [Online]. Available: https://doi.org/10.1103/physrevlett.102.203902

[18] L. Liu, R. Kumar, K. Huybrechts, T. Spuesens, G. Roelkens, E.-J. Geluk, T. de Vries, P. Regreny, D. V. Thourhout, R. Baets, and G. Morthier, "An

ultra-small, low-power, all-optical flip-flop memory on a silicon chip," *Nature Photonics*, jan 2010. [Online]. Available: https://doi.org/10.1038/nphoton.2009.268

[19] G. nter Steinmeyer, "A review of ultrafast optics and optoelectronics," *Journal of Optics A: Pure and Applied Optics*, vol. 5, no. 1, pp. R1–R15, nov 2002. [Online]. Available: https://doi.org/10.1088/1464-4258/5/1/201

[20] F. Xia, H. Wang, D. Xiao, M. Dubey, and A. Ramasubramaniam, "Two-dimensional material nanophotonics," *Nature Photonics*, vol. 8, no. 12, pp. 899–907, nov 2014. [Online]. Available: https://doi.org/10.1038/nphoton.2014.271

[21] Z. Sun, A. Martinez, and F. Wang, "Optical modulators with 2d layered materials," *Nature Photonics*, vol. 10, no. 4, pp. 227–238, apr 2016. [Online]. Available: https://doi.org/10.1038/nphoton.2016.15

[22] S. Yu, X. Wu, Y. Wang, X. Guo, and L. Tong, "2d materials for optical modulation: Challenges and opportunities," *Advanced Materials*, vol. 29, no. 14, p. 1606128, feb 2017. [Online]. Available: https://doi.org/10.1002/adma.201606128

[23] R. L. Espinola, J. I. Dadap, J. Richard M. Osgood, S. J. McNab, and Y. A. Vlasov, "C-band wavelength conversion in silicon photonic wire waveguides," *Optics Express*, vol. 13, no. 11, p. 4341, 2005. [Online]. Available: https://doi.org/10.1364/opex.13.004341

[24] K. Yamada, H. Fukuda, T. Tsuchizawa, T. Watanabe, T. Shoji, and S. Itabashi, "All-optical efficient wavelength conversion using silicon photonic wire waveguide," *IEEE Photonics Technology Letters*, vol. 18, no. 9, pp. 1046–1048, may 2006. [Online]. Available: https://doi.org/10.1109/lpt.2006.873469

[25] A. Pasquazi, R. Ahmad, M. Rochette, M. Lamont, B. E. Little, S. T. Chu, R. Morandotti, and D. J. Moss, "All-optical wavelength conversion in an integrated ring resonator," *Optics Express*, vol. 18, no. 4, p. 3858, feb 2010. [Online]. Available: https://doi.org/10.1364/oe.18.003858

[26] T. Carmon and K. J. Vahala, "Visible continuous emission from a silica microphotonic device by third-harmonic generation," *Nature Physics*, vol. 3, no. 6, pp. 430–435, may 2007. [Online]. Available: https://doi.org/10.1038/nphys601

[27] B. Corcoran, C. Monat, C. Grillet, D. J. Moss, B. J. Eggleton, T. P. White, L. OFaolain, and T. F. Krauss, "Green light emission in silicon through slow-light enhanced third-harmonic generation in photonic-crystal waveguides,"

*Nature Photonics*, vol. 3, no. 4, pp. 206–210, mar 2009. [Online]. Available: https://doi.org/10.1038/nphoton.2009.28

[28] M. R. Shcherbakov, D. N. Neshev, B. Hopkins, A. S. Shorokhov, I. Staude, E. V. Melik-Gaykazyan, M. Decker, A. A. Ezhov, A. E. Miroshnichenko, I. Brener, A. A. Fedyanin, and Y. S. Kivshar, "Enhanced third-harmonic generation in silicon nanoparticles driven by magnetic response," *Nano Letters*, vol. 14, no. 11, pp. 6488–6492, nov 2014. [Online]. Available: http://dx.doi.org/10.1021/nl503029j

[29] S. M. Raeis-Zadeh and S. Safavi-Naeini, "Analysis of electromagnetic wave scattering by graphene flakes using the generalized multipole technique," *IEEE Trans. Antennas Propagat.*, pp. 1–1, 2016. [Online]. Available: http://dx.doi.org/10.1109/TAP.2016.2515123

[30] F. Li, M. Pelusi, D.-X. Xu, A. Densmore, R. Ma, S. Janz, and D. Moss, "Error-free all-optical demultiplexing at 160gb/s via FWM in a silicon nanowire," *Optics Express*, vol. 18, no. 4, p. 3905, feb 2010. [Online]. Available: https://doi.org/10.1364/oe.18.003905

[31] B. Corcoran, M. D. Pelusi, C. Monat, J. Li, L. O'Faolain, T. F. Krauss, and B. J. Eggleton, "Ultracompact 160 gbaud all-optical demultiplexing exploiting slow light in an engineered silicon photonic crystal waveguide," *Optics Letters*, vol. 36, no. 9, p. 1728, apr 2011. [Online]. Available: https://doi.org/10.1364/ol.36.001728

[32] R. W. Boyd, *Nonlinear optics*. Academic press, 2003.

[33] B. Semnani, S. M. Raeis-Zadeh, A. Rohani, A. H. Majedi, and S. Safavi-Naeini, "Graphene-integrated plasmonic structure for optical third harmonic generation," *IEEE Journal of Selected Topics in Quantum Electronics*, vol. 23, no. 1, pp. 156–167, jan 2017. [Online]. Available: https://doi.org/10.1109/jstqe.2016.2617619

[34] T. Gu, N. Petrone, J. F. McMillan, A. van der Zande, M. Yu, G. Q. Lo, D. L. Kwong, J. Hone, and C. W. Wong, "Regenerative oscillation and four-wave mixing in graphene optoelectronics," *Nature Photonics*, vol. 6, no. 8, pp. 554–559, jul 2012. [Online]. Available: http://dx.doi.org/10.1038/nphoton.2012.147

[35] T. Tanabe, M. Notomi, S. Mitsugi, A. Shinya, and E. Kuramochi, "Fast bistable all-optical switch and memory on a silicon photonic crystal on-chip," *Optics letters*, vol. 30, no. 19, pp. 2575–2577, 2005.

[36] M. Tlidi, P. Mandel, and R. Lefever, "Localized structures and localized patterns in optical bistability," *Physical review letters*, vol. 73, no. 5, p. 640, 1994.

[37] M. Soljačić, M. Ibanescu, S. G. Johnson, Y. Fink, and J. Joannopoulos, "Optimal bistable switching in nonlinear photonic crystals," *Physical Review E*, vol. 66, no. 5, p. 055601, 2002.

[38] F. Bonaccorso, Z. Sun, T. Hasan, and A. C. Ferrari, "Graphene photonics and optoelectronics," *Nature Photonics*, vol. 4, no. 9, pp. 611–622, aug 2010. [Online]. Available: https://doi.org/10.1038/nphoton.2010.186

[39] S.-Y. Hong, J. I. Dadap, N. Petrone, P.-C. Yeh, J. Hone, and R. M. Osgood, "Optical third-harmonic generation in graphene," *Phys. Rev. X*, vol. 3, p. 021014, Jun 2013. [Online]. Available: http://link.aps.org/doi/10.1103/PhysRevX.3.021014

[40] E. Malic, T. Winzer, F. Wendler, and A. Knorr, "Review on carrier multiplication in graphene," *physica status solidi (b)*, vol. 253, no. 12, pp. 2303–2310, oct 2016. [Online]. Available: https://doi.org/10.1002/pssb.201600416

[41] H. P. Boehm, R. Setton, and E. Stumpp, "Nomenclature and terminology of graphite intercalation compounds (iupac recommendations 1994)," *Pure and Applied Chemistry*, vol. 66, no. 9, pp. 1893–1901, 1994.

[42] M. I. Katsnelson, *Graphene: carbon in two dimensions*. Cambridge University Press, 2012.

[43] A. K. Geim and K. S. Novoselov, "The rise of graphene," *Nature Materials*, vol. 6, no. 3, pp. 183–191, mar 2007. [Online]. Available: https://doi.org/10.1038/nmat1849

[44] B. R. Patton and L. Sham, "Conductivity, superconductivity, and the peierls instability," *Physical Review Letters*, vol. 31, no. 10, p. 631, 1973.

[45] K. S. Novoselov, A. K. Geim, S. Morozov, D. Jiang, Y. Zhang, S. Dubonos, I. Grigorieva, and A. Firsov, "Electric field effect in atomically thin carbon films," *science*, vol. 306, no. 5696, pp. 666–669, 2004.

[46] K. S. Novoselov, A. K. Geim, S. V. Morozov, D. Jiang, M. I. Katsnelson, I. V. Grigorieva, S. V. Dubonos, and A. A. Firsov, "Two-dimensional gas of massless dirac fermions in graphene," *Nature*, vol. 438, no. 7065, pp. 197–200, nov 2005. [Online]. Available: http://dx.doi.org/10.1038/nature04233

[47] K. Novoselov, D. Jiang, F. Schedin, T. Booth, V. Khotkevich, S. Morozov, and A. Geim, "Two-dimensional atomic crystals," *Proceedings of the National Academy of Sciences of the United States of America*, vol. 102, no. 30, pp. 10 451–10 453, 2005.

[48] A. H. Castro Neto, F. Guinea, N. M. R. Peres, K. S. Novoselov, and A. K. Geim, "The electronic properties of graphene," *Rev. Mod. Phys.*, vol. 81, pp. 109–162, Jan 2009. [Online]. Available: http://link.aps.org/doi/10.1103/RevModPhys.81.109

[49] C. Lee, X. Wei, J. W. Kysar, and J. Hone, "Measurement of the elastic properties and intrinsic strength of monolayer graphene," *science*, vol. 321, no. 5887, pp. 385–388, 2008.

[50] F. Bonaccorso, Z. Sun, T. Hasan, and A. Ferrari, "Graphene photonics and optoelectronics," *Nature photonics*, vol. 4, no. 9, pp. 611–622, 2010.

[51] M. Katsnelson and K. Novoselov, "Graphene: New bridge between condensed matter physics and quantum electrodynamics," *Solid State Communications*, vol. 143, no. 1, pp. 3–13, 2007.

[52] K. Bolotin, K. Sikes, Z. Jiang, M. Klima, G. Fudenberg, J. Hone, P. Kim, and H. Stormer, "Ultrahigh electron mobility in suspended graphene," *Solid State Communications*, vol. 146, no. 9, pp. 351 – 355, 2008. [Online]. Available: http://www.sciencedirect.com/science/article/pii/S0038109808001178

[53] M. I. Katsnelson, "Zitterbewegung, chirality, and minimal conductivity in graphene," *The European Physical Journal B*, vol. 51, no. 2, pp. 157–160, may 2006. [Online]. Available: https://doi.org/10.1140/epjb/e2006-00203-1

[54] A. F. Young and P. Kim, "Quantum interference and klein tunnelling in graphene heterojunctions," *Nat Phys*, vol. 5, no. 3, pp. 222–226, Mar 2009. [Online]. Available: http://dx.doi.org/10.1038/nphys1198

[55] Y. Zhang, Y.-W. Tan, H. L. Stormer, and P. Kim, "Experimental observation of the quantum hall effect and berry's phase in graphene," *Nature*, vol. 438, no. 7065, pp. 201–204, Nov 2005. [Online]. Available: http://dx.doi.org/10.1038/nature04235

[56] V. P. Gusynin and S. G. Sharapov, "Unconventional integer quantum hall effect in graphene," *Phys. Rev. Lett.*, vol. 95.

[57] R. V. Gorbachev, J. C. W. Song, G. L. Yu, A. V. Kretinin, F. Withers, Y. Cao, A. Mishchenko, I. V. Grigorieva, K. S. Novoselov, L. S. Levitov, and

A. K. Geim, "Detecting topological currents in graphene superlattices," *Science*, 2014. [Online]. Available: http://science.sciencemag.org/content/early/2014/09/10/science.1254966

[58] K. S. Novoselov, A. K. Geim, S. V. Morozov, D. Jiang, M. I. Katsnelson, I. V. Grigorieva, S. V. Dubonos, and A. A. Firsov, "Two-dimensional gas of massless dirac fermions in graphene," *Nature*, vol. 438, no. 7065, pp. 197–200, nov 2005. [Online]. Available: http://dx.doi.org/10.1038/nature04233

[59] J. G. Checkelsky, L. Li, and N. P. Ong, "Zero-energy state in graphene in a high magnetic field," *Phys. Rev. Lett.*, vol. 100, p. 206801, May 2008. [Online]. Available: https://link.aps.org/doi/10.1103/PhysRevLett.100.206801

[60] F. Schwierz, "Graphene transistors," *Nature nanotechnology*, vol. 5, no. 7, pp. 487–496, 2010.

[61] C. Qiu, W. Gao, R. Vajtai, P. M. Ajayan, J. Kono, and Q. Xu, "Efficient modulation of 1.55 m radiation with gated graphene on a silicon microring resonator," *Nano Letters*, vol. 14, no. 12, pp. 6811–6815, nov 2014. [Online]. Available: https://doi.org/10.1021/nl502363u

[62] X. Gan, R.-J. Shiue, Y. Gao, K. F. Mak, X. Yao, L. Li, A. Szep, D. Walker, J. Hone, T. F. Heinz, and D. Englund, "High-contrast electrooptic modulation of a photonic crystal nanocavity by electrical gating of graphene," *Nano Letters*, vol. 13, no. 2, pp. 691–696, jan 2013. [Online]. Available: https://doi.org/10.1021/nl304357u

[63] Y. Gao, R.-J. Shiue, X. Gan, L. Li, C. Peng, I. Meric, L. Wang, A. Szep, D. Walker, J. Hone, and D. Englund, "High-speed electro-optic modulator integrated with graphene-boron nitride heterostructure and photonic crystal nanocavity," *Nano Letters*, vol. 15, no. 3, pp. 2001–2005, mar 2015. [Online]. Available: https://doi.org/10.1021/nl504860z

[64] C. T. Phare, Y.-H. D. Lee, J. Cardenas, and M. Lipson, "Graphene electro-optic modulator with 30 GHz bandwidth," *Nature Photonics*, vol. 9, no. 8, pp. 511–514, jul 2015. [Online]. Available: https://doi.org/10.1038/nphoton.2015.122

[65] T. Mueller, F. Xia, and P. Avouris, "Graphene photodetectors for high-speed optical communications," *Nature Photonics*, vol. 4, no. 5, pp. 297–301, mar 2010. [Online]. Available: https://doi.org/10.1038/nphoton.2010.40

[66] M. Furchi, A. Urich, A. Pospischil, G. Lilley, K. Unterrainer, H. Detz, P. Klang, A. M. Andrews, W. Schrenk, G. Strasser, and T. Mueller, "Microcavity-integrated graphene photodetector," *Nano Letters*, vol. 12, no. 6, pp. 2773–2777, may 2012. [Online]. Available: https://doi.org/10.1021/nl204512x

[67] X. Wang, L. Zhi, and K. Müllen, "Transparent, conductive graphene electrodes for dye-sensitized solar cells," *Nano Letters*, vol. 8, no. 1, pp. 323–327, jan 2008. [Online]. Available: https://doi.org/10.1021/nl072838r

[68] P. Matyba, H. Yamaguchi, G. Eda, M. Chhowalla, L. Edman, and N. D. Robinson, "Graphene and mobile ions: The key to all-plastic, solution-processed light-emitting devices," *ACS Nano*, vol. 4, no. 2, pp. 637–642, feb 2010. [Online]. Available: https://doi.org/10.1021/nn9018569

[69] Q. Bao, H. Zhang, Y. Wang, Z. Ni, Y. Yan, Z. X. Shen, K. P. Loh, and D. Y. Tang, "Atomic-layer graphene as a saturable absorber for ultrafast pulsed lasers," *Advanced Functional Materials*, vol. 19, no. 19, pp. 3077–3083, oct 2009. [Online]. Available: https://doi.org/10.1002/adfm.200901007

[70] M. I. Katsnelson, K. S. Novoselov, and A. K. Geim, "Chiral tunnelling and the klein paradox in graphene," *Nature Physics*, vol. 2, no. 9, pp. 620–625, aug 2006. [Online]. Available: http://dx.doi.org/10.1038/nphys384

[71] B. Semnani, A. H. Majedi, and S. Safavi-Naeini, "Nonlinear quantum optical properties of graphene," *Journal of Optics*, vol. 18, no. 3, p. 035402, 2016. [Online]. Available: http://stacks.iop.org/2040-8986/18/i=3/a=035402

[72] H. Min, J. E. Hill, N. A. Sinitsyn, B. R. Sahu, L. Kleinman, and A. H. MacDonald, "Intrinsic and rashba spin-orbit interactions in graphene sheets," *Physical Review B*, vol. 74, no. 16, oct 2006. [Online]. Available: https://doi.org/10.1103/physrevb.74.165310

[73] J. L. Cheng, N. Vermeulen, and J. E. Sipe, "DC current induced second order optical nonlinearity in graphene," *Opt. Express*, vol. 22, no. 13, p. 15868, 2014. [Online]. Available: http://dx.doi.org/10.1364/OE.22.015868

[74] ——, "Third-order nonlinearity of graphene: Effects of phenomenological relaxation and finite temperature," *Physical Review B*, vol. 91, no. 23, jun 2015. [Online]. Available: https://doi.org/10.1103/physrevb.91.235320

[75] S. A. Mikhailov, "Quantum theory of the third-order nonlinear electrodynamic effects of graphene," *Physical Review B*, vol. 93, no. 8, feb 2016. [Online]. Available: https://doi.org/10.1103/physrevb.93.085403

[76] E. Hendry, P. J. Hale, J. Moger, A. K. Savchenko, and S. A. Mikhailov, "Coherent nonlinear optical response of graphene," *Phys. Rev. Lett.*, vol. 105, p. 097401, Aug 2010. [Online]. Available: http://link.aps.org/doi/10.1103/PhysRevLett.105.097401

[77] H. Zhang, S. Virally, Q. Bao, L. K. Ping, S. Massar, N. Godbout, and P. Kockaert, "Z-scan measurement of the nonlinear refractive index of graphene," *Opt. Lett.*, vol. 37, no. 11, p. 1856, 2012. [Online]. Available: http://dx.doi.org/10.1364/OL.37.001856

[78] W. Chen, G. Wang, S. Qin, C. Wang, J. Fang, J. Qi, X. Zhang, L. Wang, H. Jia, and S. Chang, "The nonlinear optical properties of coupling and decoupling graphene layers," *AIP Advances*, vol. 3, no. 4, p. 042123, apr 2013. [Online]. Available: https://doi.org/10.1063/1.4802889

[79] E. Dremetsika, B. Dlubak, S.-P. Gorza, C. Ciret, M.-B. Martin, S. Hofmann, P. Seneor, D. Dolfi, S. Massar, P. Emplit, and P. Kockaert, "Measuring the nonlinear refractive index of graphene using the optical kerr effect method," *Optics Letters*, vol. 41, no. 14, p. 3281, jul 2016. [Online]. Available: https://doi.org/10.1364/ol.41.003281

[80] L. Miao, Y. Jiang, S. Lu, B. Shi, C. Zhao, H. Zhang, and S. Wen, "Broadband ultrafast nonlinear optical response of few-layers graphene: toward the mid-infrared regime," *Photon. Res.*, vol. 3, no. 5, p. 214, 2015. [Online]. Available: http://dx.doi.org/10.1364/PRJ.3.000214

[81] Y. Zhang, Y.-W. Tan, H. L. Stormer, and P. Kim, "Experimental observation of the quantum hall effect and berrys phase in graphene," *Nature*, vol. 438, no. 7065, pp. 201–204, nov 2005. [Online]. Available: http://dx.doi.org/10.1038/nature04235

[82] V. P. Gusynin, S. G. Sharapov, and J. P. Carbotte, "Magneto-optical conductivity in graphene," *J. Phys.: Condens. Matter*, vol. 19, no. 2, p. 026222, dec 2006. [Online]. Available: http://dx.doi.org/10.1088/0953-8984/19/2/026222

[83] ——, "AC conductivity of graphene: From tight-binding model to 2 1-dimensional quantum electrodynamics," *Int. J. Mod. Phys. B*, vol. 21, no. 27, pp. 4611–4658, oct 2007. [Online]. Available: http://dx.doi.org/10.1142/S0217979207038022

[84] E. H. Hwang and S. Das Sarma, "Dielectric function, screening, and plasmons in two-dimensional graphene," *Phys. Rev. B*, vol. 75, p. 205418, May 2007. [Online]. Available: http://link.aps.org/doi/10.1103/PhysRevB.75.205418

[85] T. Stauber, N. M. R. Peres, and A. K. Geim, "Optical conductivity of graphene in the visible region of the spectrum," *Phys. Rev. B*, vol. 78, p. 085432, Aug 2008. [Online]. Available: http://link.aps.org/doi/10.1103/PhysRevB.78.085432

[86] J. Horng, C.-F. Chen, B. Geng, C. Girit, Y. Zhang, Z. Hao, H. A. Bechtel, M. Martin, A. Zettl, M. F. Crommie, Y. R. Shen, and F. Wang, "Drude conductivity of dirac fermions in graphene," *Phys. Rev. B*, vol. 83, p. 165113, Apr 2011. [Online]. Available: http://link.aps.org/doi/10.1103/PhysRevB.83.165113

[87] J. M. Dawlaty, S. Shivaraman, J. Strait, P. George, M. Chandrashekhar, F. Rana, M. G. Spencer, D. Veksler, and Y. Chen, "Measurement of the optical absorption spectra of epitaxial graphene from terahertz to visible," *Appl. Phys. Lett.*, vol. 93, no. 13, p. 131905, 2008. [Online]. Available: http://dx.doi.org/10.1063/1.2990753

[88] A. Bácsi and A. Virosztek, "Low-frequency optical conductivity in graphene and in other scale-invariant two-band systems," *Phys. Rev. B*, vol. 87, p. 125425, Mar 2013. [Online]. Available: http://link.aps.org/doi/10.1103/PhysRevB.87.125425

[89] S. A. Mikhailov and K. Ziegler, "Nonlinear electromagnetic response of graphene: frequency multiplication and the self-consistent-field effects," *J. Phys.: Condens. Matter*, vol. 20, no. 38, p. 384204, aug 2008. [Online]. Available: http://dx.doi.org/10.1088/0953-8984/20/38/384204

[90] A. R. Wright, X. G. Xu, J. C. Cao, and C. Zhang, "Strong nonlinear optical response of graphene in the terahertz regime," *Appl. Phys. Lett.*, vol. 95, no. 7, p. 072101, 2009. [Online]. Available: http://dx.doi.org/10.1063/1.3205115

[91] K. L. Ishikawa, "Nonlinear optical response of graphene in time domain," *Phys. Rev. B*, vol. 82, p. 201402, Nov 2010. [Online]. Available: http://link.aps.org/doi/10.1103/PhysRevB.82.201402

[92] A. Roberts, D. Cormode, C. Reynolds, T. Newhouse-Illige, B. J. LeRoy, and A. S. Sandhu, "Response of graphene to femtosecond high-intensity laser irradiation," *Appl. Phys. Lett.*, vol. 99, no. 5, p. 051912, 2011. [Online]. Available: http://dx.doi.org/10.1063/1.3623760

[93] K. L. Ishikawa, "Electronic response of graphene to an ultrashort intense terahertz radiation pulse," *New J. Phys.*, vol. 15, no. 5, p. 055021, may 2013. [Online]. Available: http://dx.doi.org/10.1088/1367-2630/15/5/055021

[94] J. L. Cheng, N. Vermeulen, and J. E. Sipe, "Third order optical nonlinearity of graphene," *New J. Phys.*, vol. 16, no. 5, p. 053014, may 2014. [Online]. Available: http://dx.doi.org/10.1088/1367-2630/16/5/053014

[95] S. A. Mikhailov, "Quantum theory of third-harmonic generation in graphene," *Phys. Rev. B*, vol. 90, p. 241301, Dec 2014. [Online]. Available: http://link.aps.org/doi/10.1103/PhysRevB.90.241301

[96] S. A. Jafari, "Nonlinear optical response in gapped graphene," *Journal of Physics: Condensed Matter*, vol. 24, no. 20, p. 205802, apr 2012. [Online]. Available: http://dx.doi.org/10.1088/0953-8984/24/20/205802

[97] Y. Hatsugai, "Topological aspect of graphene physics," *J. Phys.: Conf. Ser.*, vol. 334, p. 012004, dec 2011. [Online]. Available: http://dx.doi.org/10.1088/1742-6596/334/1/012004

[98] M. Lindberg and S. W. Koch, "Effective bloch equations for semiconductors," *Phys. Rev. B*, vol. 38, pp. 3342–3350, Aug 1988. [Online]. Available: http://link.aps.org/doi/10.1103/PhysRevB.38.3342

[99] C. F. Klingshirn, *Semiconductor optics*. Springer Science & Business Media, 2012.

[100] C. Aversa and J. E. Sipe, "Nonlinear optical susceptibilities of semiconductors: Results with a length-gauge analysis," *Phys. Rev. B*, vol. 52, pp. 14 636–14 645, Nov 1995. [Online]. Available: http://link.aps.org/doi/10.1103/PhysRevB.52.14636

[101] H. K. Avetissian, G. F. Mkrtchian, K. G. Batrakov, S. A. Maksimenko, and A. Hoffmann, "Nonlinear theory of graphene interaction with strong laser radiation beyond the dirac cone approximation: Coherent control of quantum states in nano-optics," *Phys. Rev. B*, vol. 88, p. 245411, Dec 2013. [Online]. Available: http://link.aps.org/doi/10.1103/PhysRevB.88.245411

[102] T. Stroucken, J. H. Grönqvist, and S. W. Koch, "Optical response and ground state of graphene," *Phys. Rev. B*, vol. 84, p. 205445, Nov 2011. [Online]. Available: http://link.aps.org/doi/10.1103/PhysRevB.84.205445

[103] H. K. Kelardeh, V. Apalkov, and M. I. Stockman, "Wannier-stark states of graphene in strong electric field," *Physical Review B*, vol. 90, no. 8, aug 2014. [Online]. Available: https://doi.org/10.1103/physrevb.90.085313

[104] S. Reich, J. Maultzsch, C. Thomsen, and P. Ordejón, "Tight-binding description of graphene," *Phys. Rev. B*, vol. 66, p. 035412, Jul 2002. [Online]. Available: http://link.aps.org/doi/10.1103/PhysRevB.66.035412

[105] T. Stauber, P. Parida, M. Trushin, M. V. Ulybyshev, D. L. Boyda, and J. Schliemann, "Interacting electrons in graphene: Fermi velocity renormalization and optical response," *Phys. Rev. Lett.*, vol. 118, p. 266801, Jun 2017. [Online]. Available: https://link.aps.org/doi/10.1103/PhysRevLett.118.266801

[106] J. J. Sakurai and S. F. Tuan, *Modern quantum mechanics*. Addison-Wesley Reading, Massachusetts, 1985, vol. 1.

[107] M. Gradhand, D. V. Fedorov, F. Pientka, P. Zahn, I. Mertig, and B. L. Györffy, "First-principle calculations of the berry curvature of bloch states for charge and spin transport of electrons," *Journal of Physics: Condensed Matter*, vol. 24, no. 21, p. 213202, may 2012. [Online]. Available: http://dx.doi.org/10.1088/0953-8984/24/21/213202

[108] B. A. Bernevig, *Topological Insulators and Topological Superconductors*. Princeton University Press, 2013.

[109] C. L. Kane and E. J. Mele, "Quantum spin hall effect in graphene," *Phys. Rev. Lett.*, vol. 95, p. 226801, Nov 2005. [Online]. Available: http://link.aps.org/doi/10.1103/PhysRevLett.95.226801

[110] T. Choudhari and N. Deo, "Graphene with wedge disclination in the presence of intrinsic and rashba spin orbit couplings," *EPL*, vol. 108, no. 5, p. 57006, dec 2014. [Online]. Available: http://dx.doi.org/10.1209/0295-5075/108/57006

[111] T. Stauber, P. Parida, M. Trushin, M. Ulybyshev, D. Boyda, and J. Schliemann, "Interacting electrons in graphene: Fermi velocity renormalization and optical response," *Physical Review Letters*, vol. 118, no. 26, jun 2017. [Online]. Available: https://doi.org/10.1103/physrevlett.118.266801

[112] L. Yang, J. Deslippe, C.-H. Park, M. L. Cohen, and S. G. Louie, "Excitonic effects on the optical response of graphene and bilayer graphene,"

*Physical Review Letters*, vol. 103, no. 18, oct 2009. [Online]. Available: https://doi.org/10.1103/physrevlett.103.186802

[113] M. I. Katsnelson, "Zitterbewegung, chirality, and minimal conductivity in graphene," *The European Physical Journal B*, vol. 51, no. 2, pp. 157–160, may 2006. [Online]. Available: https://doi.org/10.1140/epjb/e2006-00203-1

[114] E. Malic, T. Winzer, E. Bobkin, and A. Knorr, "Microscopic theory of absorption and ultrafast many-particle kinetics in graphene," *Physical Review B*, vol. 84, no. 20, nov 2011. [Online]. Available: https://doi.org/10.1103/physrevb.84.205406

[115] R. W. Boyd, *Nonlinear optics*. Academic press, 2003.

[116] R. W. Boyd and M. Sargent, "Population pulsations and the dynamic stark effect," *Journal of the Optical Society of America B*, vol. 5, no. 1, p. 99, jan 1988. [Online]. Available: https://doi.org/10.1364/josab.5.000099

[117] T. Stauber, N. M. R. Peres, and F. Guinea, "Electronic transport in graphene: A semiclassical approach including midgap states," *Phys. Rev. B*, vol. 76, p. 205423, Nov 2007. [Online]. Available: http://link.aps.org/doi/10.1103/PhysRevB.76.205423

[118] E. Malic and A. Knorr, *Graphene and Carbon Nanotubes: Ultrafast Optics and Relaxation Dynamics*. John Wiley & Sons, 2013.

[119] L. M. Malard, K. F. Mak, A. H. C. Neto, N. M. R. Peres, and T. F. Heinz, "Observation of intra- and inter-band transitions in the transient optical response of graphene," *New J. Phys.*, vol. 15, no. 1, p. 015009, jan 2013. [Online]. Available: http://dx.doi.org/10.1088/1367-2630/15/1/015009

[120] Y. Hatsugai, T. Morimoto, T. Kawarabayashi, Y. Hamamoto, and H. Aoki, "Chiral symmetry and its manifestation in optical responses in graphene: interaction and multilayers," *New Journal of Physics*, vol. 15, no. 3, p. 035023, mar 2013. [Online]. Available: http://dx.doi.org/10.1088/1367-2630/15/3/035023

[121] R. D. Coso and J. Solis, "Relation between nonlinear refractive index and third-order susceptibility in absorbing media," *Journal of the Optical Society of America B*, vol. 21, no. 3, p. 640, 2004. [Online]. Available: http://dx.doi.org/10.1364/JOSAB.21.000640

[122] M. Sheik-Bahae, D. Hutchings, D. Hagan, and E. V. Stryland, "Dispersion of bound electron nonlinear refraction in solids," *IEEE J. Quantum Electron.*, vol. 27, no. 6, pp. 1296–1309, jun 1991. [Online]. Available: http://dx.doi.org/10.1109/3.89946

[123] M. Sheik-bahae, A. A. Said, and E. W. V. Stryland, "High-sensitivity, single-beam n_2 measurements," *Optics Letters*, vol. 14, no. 17, p. 955, sep 1989. [Online]. Available: https://doi.org/10.1364/ol.14.000955

[124] M. Sheik-Bahae, A. Said, T.-H. Wei, D. Hagan, and E. V. Stryland, "Sensitive measurement of optical nonlinearities using a single beam," *IEEE Journal of Quantum Electronics*, vol. 26, no. 4, pp. 760–769, apr 1990. [Online]. Available: https://doi.org/10.1109/3.53394

[125] M. J. Bastiaans, "The expansion of an optical signal into a discrete set of gaussian beams," in *Erzeugung und Analyse von Bildern und Strukturen*. Springer, 1980, pp. 23–32.

[126] D. A. Kleinman and W. G. Spitzer, "Theory of the optical properties of quartz in the infrared," *Physical Review*, vol. 125, no. 1, pp. 16–30, jan 1962. [Online]. Available: https://doi.org/10.1103/physrev.125.16

[127] J. B. Lassiter, X. Chen, X. Liu, C. Ciracì, T. B. Hoang, S. Larouche, S.-H. Oh, M. H. Mikkelsen, and D. R. Smith, "Third-harmonic generation enhancement by film-coupled plasmonic stripe resonators," *ACS Photonics*, vol. 1, no. 11, pp. 1212–1217, nov 2014. [Online]. Available: http://dx.doi.org/10.1021/ph500276v

[128] A. Bouhelier, M. Beversluis, A. Hartschuh, and L. Novotny, "Near-field second-harmonic generation induced by local field enhancement," *Phys. Rev. Lett.*, vol. 90, no. 1, jan 2003. [Online]. Available: http://dx.doi.org/10.1103/PhysRevLett.90.013903

[129] W. R. Zipfel, R. M. Williams, and W. W. Webb, "Nonlinear magic: multiphoton microscopy in the biosciences," *Nat Biotechnol*, vol. 21, no. 11, pp. 1369–1377, nov 2003. [Online]. Available: http://dx.doi.org/10.1038/nbt899

[130] S. Kim, J. Jin, Y.-J. Kim, I.-Y. Park, Y. Kim, and S.-W. Kim, "High-harmonic generation by resonant plasmon field enhancement," *Nature*, vol. 453, no. 7196, pp. 757–760, jun 2008. [Online]. Available: http://dx.doi.org/10.1038/nature07012

[131] M. Sivis, M. Duwe, B. Abel, and C. Ropers, "Extreme-ultraviolet light generation in plasmonic nanostructures," *Nat Phys*, vol. 9, no. 5, pp. 304–309, mar 2013. [Online]. Available: http://dx.doi.org/10.1038/nphys2590

[132] W. L. Barnes, A. Dereux, and T. W. Ebbesen, "Surface plasmon subwavelength optics," *Nature*, vol. 424, no. 6950, pp. 824–830, aug 2003. [Online]. Available: http://dx.doi.org/10.1038/nature01937

[133] Y. Akahane, T. Asano, B.-S. Song, and S. Noda, "High-q photonic nanocavity in a two-dimensional photonic crystal," *Nature*, vol. 425, no. 6961, pp. 944–947, oct 2003. [Online]. Available: http://dx.doi.org/10.1038/nature02063

[134] J. Bravo-Abad, A. Rodriguez, P. Bermel, S. G. Johnson, J. D. Joannopoulos, and M. Soljacic, "Enhanced nonlinear optics in photonic-crystal microcavities," *Opt. Express*, vol. 15, no. 24, p. 16161, 2007.

[135] J. Lee, M. Tymchenko, C. Argyropoulos, P.-Y. Chen, F. Lu, F. Demmerle, G. Boehm, M.-C. Amann, A. Alù, and M. A. Belkin, "Giant nonlinear response from plasmonic metasurfaces coupled to intersubband transitions," *Nature*, vol. 511, no. 7507, pp. 65–69, jul 2014. [Online]. Available: http://dx.doi.org/10.1038/nature13455

[136] O. Wolf, S. Campione, A. Benz, A. P. Ravikumar, S. Liu, T. S. Luk, E. A. Kadlec, E. A. Shaner, J. F. Klem, M. B. Sinclair, and I. Brener, "Phased-array sources based on nonlinear metamaterial nanocavities," *Nature Communications*, vol. 6, p. 7667, jul 2015. [Online]. Available: http://dx.doi.org/10.1038/ncomms8667

[137] D. Akinwande, N. Petrone, and J. Hone, "Two-dimensional flexible nanoelectronics," *Nature Communications*, vol. 5, p. 5678, dec 2014. [Online]. Available: http://dx.doi.org/10.1038/ncomms6678

[138] C. Ciracì, M. Scalora, and D. R. Smith, "Third-harmonic generation in the presence of classical nonlocal effects in gap-plasmon nanostructures," *Phys. Rev. B*, vol. 91, no. 20, may 2015. [Online]. Available: http://dx.doi.org/10.1103/PhysRevB.91.205403

[139] B. Semnani, A. H. Majedi, and S. Safavi-Naeini, "Nonlinear quantum optical properties of graphene," *Journal of Optics*, vol. 18, no. 3, p. 035402, feb 2016. [Online]. Available: http://dx.doi.org/10.1088/2040-8978/18/3/035402

[140] A. B. Evlyukhin, C. Reinhardt, E. Evlyukhin, and B. N. Chichkov, "Multipole analysis of light scattering by arbitrary-shaped nanoparticles on a plane surface," *Journal of the Optical Society of America B*, vol. 30, no. 10, p. 2589, sep 2013. [Online]. Available: http://dx.doi.org/10.1364/JOSAB.30.002589

[141] N. A. Savostianova and S. A. Mikhailov, "Giant enhancement of the third harmonic in graphene integrated in a layered structure," *Appl. Phys. Lett.*, vol. 107, no. 18, p. 181104, nov 2015. [Online]. Available: http://dx.doi.org/10.1063/1.4935041

[142] B. Auguié and W. L. Barnes, "Collective resonances in gold nanoparticle arrays," *Phys. Rev. Lett.*, vol. 101, no. 14, sep 2008. [Online]. Available: http://dx.doi.org/10.1103/PhysRevLett.101.143902

[143] A. Trügler, *Optical properties of metallic nanoparticles*. Springer, 2011.

[144] J. Smajic, C. Hafner, L. Raguin, K. Tavzarashvili, and M. Mishrikey, "Comparison of numerical methods for the analysis of plasmonic structures," *Journal of Computational and Theoretical Nanoscience*, vol. 6, no. 3, pp. 763–774, mar 2009. [Online]. Available: http://dx.doi.org/10.1166/jctn.2009.1107

[145] A. Y. Nikitin, F. J. Garcia-Vidal, and L. Martin-Moreno, "Analytical expressions for the electromagnetic dyadic green's function in graphene and thin layers," *IEEE J. Select. Topics Quantum Electron.*, vol. 19, no. 3, pp. 4 600 611–4 600 611, may 2013. [Online]. Available: http://dx.doi.org/10.1109/JSTQE.2012.2226147

[146] A. K. Bhattacharyya, *Phased array antennas: Floquet analysis, synthesis, BFNs and active array systems*. John Wiley & Sons, 2006, vol. 179.

[147] H. Kim, J. Park, and B. Lee, *Fourier modal method and its applications in computational nanophotonics*. CRC Press, 2012.

[148] J. B. Monteiro-Filho and L. A. Gómez-Malagón, "Resonant third order nonlinear optical susceptibility of gold nanoparticles," *Journal of the Optical Society of America B*, vol. 29, no. 7, p. 1793, jun 2012. [Online]. Available: http://dx.doi.org/10.1364/JOSAB.29.001793

[149] R. W. Boyd, Z. Shi, and I. D. Leon, "The third-order nonlinear optical susceptibility of gold," *Optics Communications*, vol. 326, pp. 74–79, sep 2014. [Online]. Available: http://dx.doi.org/10.1016/j.optcom.2014.03.005

[150] S. Selleri, M. Mussetta, P. Pirinoli, R. E. Zich, and L. Matekovits, "Differentiated meta-PSO methods for array optimization," *IEEE Trans. Antennas Propagat.*, vol. 56, no. 1, pp. 67–75, jan 2008. [Online]. Available: http://dx.doi.org/10.1109/TAP.2007.912942

[151] H. Aouani, M. Rahmani, M. Navarro-Cía, and S. A. Maier, "Third-harmonic-upconversion enhancement from a single semiconductor nanoparticle coupled to a plasmonic antenna," *Nature Nanotech*, vol. 9, no. 4, pp. 290–294, mar 2014. [Online]. Available: http://dx.doi.org/10.1038/nnano.2014.27

[152] D. J. Lockwood and L. Pavesi, "Silicon fundamentals for photonics applications," in *Topics in Applied Physics*. Springer Berlin Heidelberg, feb 2004, pp. 1–50. [Online]. Available: https://doi.org/10.1007/978-3-540-39913-1_1

[153] A. Haché and M. Bourgeois, "Ultrafast all-optical switching in a silicon-based photonic crystal," *Applied Physics Letters*, vol. 77, no. 25, pp. 4089–4091, dec 2000. [Online]. Available: https://doi.org/10.1063/1.1332823

[154] S. F. Preble, Q. Xu, B. S. Schmidt, and M. Lipson, "Ultrafast all-optical modulation on a silicon chip," *Optics Letters*, vol. 30, no. 21, p. 2891, nov 2005. [Online]. Available: https://doi.org/10.1364/ol.30.002891

[155] W. Li, B. Chen, C. Meng, W. Fang, Y. Xiao, X. Li, Z. Hu, Y. Xu, L. Tong, H. Wang, W. Liu, J. Bao, and Y. R. Shen, "Ultrafast all-optical graphene modulator," *Nano Letters*, vol. 14, no. 2, pp. 955–959, jan 2014. [Online]. Available: https://doi.org/10.1021/nl404356t

[156] S. Yu, X. Wu, K. Chen, B. Chen, X. Guo, D. Dai, L. Tong, W. Liu, and Y. R. Shen, "All-optical graphene modulator based on optical kerr phase shift," *Optica*, vol. 3, no. 5, p. 541, may 2016. [Online]. Available: https://doi.org/10.1364/optica.3.000541

[157] J. D. Joannopoulos, S. G. Johnson, J. N. Winn, and R. D. Meade, *Photonic crystals: molding the flow of light*. Princeton university press, 2011.

[158] J. S. Foresi, P. R. Villeneuve, J. Ferrera, E. R. Thoen, G. Steinmeyer, S. Fan, J. D. Joannopoulos, L. C. Kimerling, H. I. Smith, and E. P. Ippen, "Photonic-bandgap microcavities in optical waveguides," *Nature*, vol. 390, no. 6656, pp. 143–145, nov 1997. [Online]. Available: https://doi.org/10.1038/36514

[159] O. Painter, J. Vučkovič, and A. Scherer, "Defect modes of a two-dimensional photonic crystal in an optically thin dielectric slab," *Journal of the Optical Society of America B*, vol. 16, no. 2, p. 275, feb 1999. [Online]. Available: https://doi.org/10.1364/josab.16.000275

[160] J. Vučković, M. Lončar, H. Mabuchi, and A. Scherer, "Design of photonic crystal microcavities for cavity QED," *Physical Review E*, vol. 65, no. 1, dec 2001. [Online]. Available: https://doi.org/10.1103/physreve.65.016608

[161] B.-S. Song, S. Noda, T. Asano, and Y. Akahane, "Ultra-high-q photonic double-heterostructure nanocavity," *Nature Materials*, vol. 4, no. 3, pp. 207–210, feb 2005. [Online]. Available: https://doi.org/10.1038/nmat1320

[162] S. G. Johnson, S. Fan, P. R. Villeneuve, J. D. Joannopoulos, and L. A. Kolodziejski, "Guided modes in photonic crystal slabs," *Physical Review B*, vol. 60, no. 8, pp. 5751–5758, aug 1999. [Online]. Available: https://doi.org/10.1103/physrevb.60.5751

[163] J. Vučković, M. Pelton, A. Scherer, and Y. Yamamoto, "Optimization of three-dimensional micropost microcavities for cavity quantum electrodynamics," *Physical Review A*, vol. 66, no. 2, aug 2002. [Online]. Available: https://doi.org/10.1103/physreva.66.023808

[164] B.-S. Song, T. Asano, and S. Noda, "Physical origin of the small modal volume of ultra-high-q photonic double-heterostructure nanocavities," *New Journal of Physics*, vol. 8, no. 9, pp. 209–209, sep 2006. [Online]. Available: https://doi.org/10.1088/1367-2630/8/9/209

[165] Y. Akahane, T. Asano, B.-S. Song, and S. Noda, "High-q photonic nanocavity in a two-dimensional photonic crystal," *Nature*, vol. 425, no. 6961, pp. 944–947, 2003.

[166] F. Ruesink, H. M. Doeleman, R. Hendrikx, A. F. Koenderink, and E. Verhagen, "Perturbing open cavities: Anomalous resonance frequency shifts in a hybrid cavity-nanoantenna system," *Physical Review Letters*, vol. 115, no. 20, nov 2015. [Online]. Available: https://doi.org/10.1103/physrevlett.115.203904

[167] G. Vandenbosch, "Reactive energies, impedance, and Q factor of radiating structures," *IEEE Transactions on Antennas and Propagation*, vol. 58, no. 4, pp. 1112–1127, apr 2010. [Online]. Available: https://doi.org/10.1109/tap.2010.2041166

[168] M. Minsky, "Memoir on inventing the confocal scanning microscope," *Scanning*, vol. 10, no. 4, pp. 128–138, 1988. [Online]. Available: https://doi.org/10.1002/sca.4950100403

[169] M. Skorobogatiy and J. Yang, *Fundamentals of photonic crystal guiding*. Cambridge University Press, 2009.

[170] Z. Cheng, H. K. Tsang, X. Wang, K. Xu, and J.-B. Xu, "In-plane optical absorption and free carrier absorption in graphene-on-silicon waveguides," *IEEE Journal of Selected Topics in Quantum Electronics*, vol. 20, no. 1, pp. 43–48, jan 2014. [Online]. Available: https://doi.org/10.1109/jstqe.2013.2263115

[171] M. A. Green and M. J. Keevers, "Optical properties of intrinsic silicon at 300 k," *Progress in Photovoltaics: Research and Applications*, vol. 3, no. 3, pp. 189–192, 1995. [Online]. Available: https://doi.org/10.1002/pip.4670030303

[172] Z. Shi, L. Gan, T.-H. Xiao, H.-L. Guo, and Z.-Y. Li, "All-optical modulation of a graphene-cladded silicon photonic crystal cavity," *ACS Photonics*, vol. 2, no. 11, pp. 1513–1518, nov 2015. [Online]. Available: https://doi.org/10.1021/acsphotonics.5b00469

[173] X.-J. Wang, L. Zou, D. Li, Q. Zhang, F. Wang, and Z. Zhang, "Photo-induced doping in graphene/silicon heterostructures," *The Journal of Physical Chemistry C*, vol. 119, no. 2, pp. 1061–1066, jan 2015. [Online]. Available: https://doi.org/10.1021/jp509878m

[174] C.-C. Chen, M. Aykol, C.-C. Chang, A. F. J. Levi, and S. B. Cronin, "Graphene-silicon schottky diodes," *Nano Letters*, vol. 11, no. 5, pp. 1863–1867, may 2011. [Online]. Available: https://doi.org/10.1021/nl104364c

[175] S. Tongay, M. Lemaitre, X. Miao, B. Gila, B. R. Appleton, and A. F. Hebard, "Rectification at graphene-semiconductor interfaces: Zero-gap semiconductor-based diodes," *Physical Review X*, vol. 2, no. 1, jan 2012. [Online]. Available: https://doi.org/10.1103/physrevx.2.011002

[176] C. Horvath, D. Bachman, R. Indoe, and V. Van, "Photothermal nonlinearity and optical bistability in a graphene–silicon waveguide resonator," *Optics Letters*, vol. 38, no. 23, p. 5036, nov 2013. [Online]. Available: https://doi.org/10.1364/ol.38.005036

[177] A. Yu, X. Ye, D. Ionascu, W. Cao, and P. M. Champion, "Two-color pump-probe laser spectroscopy instrument with picosecond time-resolved electronic delay and extended scan range," *Review of Scientific Instruments*, vol. 76, no. 11, p. 114301, nov 2005. [Online]. Available: https://doi.org/10.1063/1.2126808

[178] C. Manzoni, D. Polli, and G. Cerullo, "Two-color pump-probe system broadly tunable over the visible and the near infrared with sub-30fs temporal resolution," *Review of Scientific Instruments*, vol. 77, no. 2, p. 023103, feb 2006. [Online]. Available: https://doi.org/10.1063/1.2167128

[179] A. Gambetta, G. Galzerano, A. G. Rozhin, A. C. Ferrari, R. Ramponi, P. Laporta, and M. Marangoni, "Sub-100 fs pump-probe spectroscopy of single wall carbon nanotubes with a 100 MHz er-fiber laser system," *Optics Express*, vol. 16, no. 16, p. 11727, jul 2008. [Online]. Available: https://doi.org/10.1364/oe.16.011727

[180] K. S. Virk and J. E. Sipe, "Semiconductor optics in length gauge: A general numerical approach," *Physical Review B*, vol. 76, no. 3, jul 2007. [Online]. Available: https://doi.org/10.1103/physrevb.76.035213

[181] G. B. Ventura, D. J. Passos, J. M. B. L. dos Santos, J. M. V. P. Lopes, and N. M. R. Peres, "Gauge covariances and nonlinear optical responses," *Physical Review B*, vol. 96, no. 3, jul 2017. [Online]. Available: https://doi.org/10.1103/physrevb.96.035431

[182] I. Al-Naib, J. E. Sipe, and M. M. Dignam, "High harmonic generation in undoped graphene: Interplay of inter- and intraband dynamics," *Physical Review B*, vol. 90, no. 24, dec 2014. [Online]. Available: https://doi.org/10.1103/physrevb.90.245423

[183] S. Piscanec, M. Lazzeri, F. Mauri, A. C. Ferrari, and J. Robertson, "Kohn anomalies and electron-phonon interactions in graphite," *Physical Review Letters*, vol. 93, no. 18, oct 2004. [Online]. Available: https://doi.org/10.1103/physrevlett.93.185503

[184] R. F. Harrington, "Time-harmonic electromagnetic fields," 2015.

# APPENDICES

# Appendix A

# Length Gauge versus Velocity Gauge for Graphene

In the long wavelength regime where the spatial dependence of the electromagnetic field can be neglected, there are two theoretical approaches to couple electromagnetic radiation into the dynamical equations. Within the so called *velocity gauge* light and matter are coupled via the minimal substitution of the vector magnetic potential $\mathbf{A}(t)$, with the electric field given by $\mathbf{E}(t) = -\partial\mathbf{A}/\partial t$. The alternative approach is referred to *length gauge* [100] where the field is directly coupled by means of the additive scalar potential $V(\mathbf{r}) = e\mathbf{E}.\mathbf{r}$ with the elementary charge $e > 0$ . Although the velocity gauge preserves the translation symmetry and different Bloch states remain uncoupled, there are several undesirable features associated with velocity gauge that plague the calculations [100, 180].

In particular, the treatment of the nonlinear optical response of the semiconductors within the velocity gauge is susceptible to numerical errors caused by truncation of the band space [100, 181]. Since the electric field is proportional to the time derivative of the vector magnetic potential, some poles at $\omega = 0$ inevitably appear. Diverging terms are not obviously real in semiconductors. It has been rigorously proven that they essentially vanish due to time reversal symmetry and an effective mass sum rule [100]. However, a full calculation of the optical transitions over the entire band is required to eliminate the diverging terms [180] and numerical errors due to truncations of the calculation would always amplify. Moreover, in the two-level systems where an effective Hamiltonian is intended to describe the electrons' dynamics (the case of graphene for instance), the application of velocity gauge is quite vulnerable [181]. Refs. [100, 181] show that in the perturbative treatment of the nonlinear optical response of such systems, the contribution made by the remaining parts of the band cannot be ignored in the calculations. This observation implies

that a *local interpretation* of the optical transitions within the velocity gauge is not reliable and all Bloch states collectively impact the optical response [181].

To cope with this situation, the length gauge can be employed. The different contributions of the position operators have been extensively discussed in the literature [100, 180] and has been shown that the perturbative treatment of the nonlinear optical response of semiconductors can be reliably performed in a two-level model by making use of the length gauge [182]. This gauge eliminates the nonphysical diverging terms and renders it possible to locally interpret the optical transition over the band space. The matrix element of the position operator between the Bloch states indexed by $(\mathbf{k}, s)$ and $(\mathbf{k}', s')$ is [180]

$$\mathbf{r}_{\mathbf{k}s,\mathbf{k}'s'} = \delta(\mathbf{k}-\mathbf{k}')[i\delta_{ss'}\frac{\partial}{\partial\mathbf{k}} + i\boldsymbol{\zeta}_{ss'}(\mathbf{k})] \tag{A.1}$$

The position operator can be interpreted as the generator of the translation in the space of Bloch functions [180]. The Berry potential $\boldsymbol{\zeta}_{ss'}(\mathbf{k})$ is required as the geometric phase correction and therefore its action in nontrivial topologies is more crucial.

To shed light on the applicability of the velocity gauge to the pertubation theory , as a benchmark, we proceed with finding the linear optical response of graphene within the velocity gauge. Assume that a graphene layer lying on the xy-plane is illuminated by an obliquely incident electromagnetic field $\mathbf{E}(\mathbf{r}) = \mathbf{E}_0 \exp(i\omega t - i\mathbf{k}_0.\mathbf{r})$. Where $\mathbf{k}_0$ is the wavenumber of the incident field. For mathematical convenience, the tangential component of $\mathbf{k}_0$ is shown by $\mathbf{q} \triangleq \mathbf{k}_0.(\hat{x}\hat{x} + \hat{y}\hat{y})$. Within the velocity gauge the time derivative of the divergence less magnetic potential $\mathbf{A}$ is linearly related to the electric field. The magnetic vector potential reads as

$$-i\omega\mathbf{A} = \mathbf{E}(\mathbf{r}) \tag{A.2}$$

The interaction Hamiltonian is then $\hat{H}_I = \mathbf{A}.\hat{\vec{\mathcal{J}}}$ where $\hat{\vec{\mathcal{J}}}$ is the current operator derived in Eq. (2.28). Using the customary minimal electron-light coupling prescription, the overal Hamiltonian reads

$$\hat{H} = \hat{H}_0 + \mathbf{A}.\hat{\vec{\mathcal{J}}} = \hat{H}_0 + \mathbf{A}_0.\hat{\vec{\mathcal{R}}}(-\mathbf{q}) \tag{A.3}$$

For compactness, we have defined the operator $\hat{\vec{\mathcal{R}}}(\mathbf{q})$ as

$$\hat{\vec{\mathcal{R}}}(\mathbf{q}) = \hat{\vec{\mathcal{J}}}\exp(+i\mathbf{q}.\boldsymbol{\rho}) \tag{A.4}$$

The linear variation of the density matrix due to the presence of the external potential is calculated using the perturbation expansion

$$\hat{\rho} = \hat{\rho}_0 + \delta\hat{\rho}^{(1)} + \cdots \tag{A.5}$$

The first order perturbation theory gives the $\delta\hat{\rho}^{(1)}$ which linearly depends on the electric field.

$$\delta\hat{\rho}^{(1)}_{\mathbf{k}s,\mathbf{k}'s'} = \frac{f(E_{\mathbf{k}',s'}) - f(E_{\mathbf{k},s})}{E_{\mathbf{k}',s'} - E_{\mathbf{k},s} + \hbar\omega + i\gamma_{ss'}} \langle \mathbf{k}, s|\hat{H}_I|\mathbf{k}', s'\rangle \tag{A.6}$$

where $f(E)$ is the Fermi-Dirac distribution.The index $s$ refers the upper and lower energy states. The parameter $\gamma$ appearing in the denominator is the phenomenological relaxation coefficient. The first order induced current is then obtained as

$$\mathbf{J}_{\mathbf{q}} = \mathrm{Tr}\left\{\delta\hat{\rho}^{(1)}\hat{\vec{\mathcal{R}}}(\mathbf{q})\right\} \tag{A.7}$$

$$\mathbf{J}_{\mathbf{q}} = \mathbf{A}_0 \cdot \sum_{ss'} \frac{f(E_{\mathbf{k}',s'}) - f(E_{\mathbf{k},s})}{E_{\mathbf{k}',s'} - E_{\mathbf{k},s} + \hbar\omega + i\gamma_{ss'}} \langle s|\hat{\vec{\mathcal{R}}}_{\mathbf{k}s,\mathbf{k}'s'}(-\mathbf{q})|s'\rangle\langle s'|\hat{\vec{\mathcal{R}}}_{\mathbf{k}'s',\mathbf{k}s}(\mathbf{q})|s\rangle \tag{A.8}$$

where

$$\hat{\vec{\mathcal{R}}}_{\mathbf{k}s,\mathbf{k}'s'}(\mathbf{q}) \approx \left(\hat{\mathbf{u}}\sigma_z + \hat{\boldsymbol{\varphi}}_u\sigma_y\right)(-ev_F) \tag{A.9}$$

form now on we define $\Pi^{ss'}_{\mathbf{k}\mathbf{k}'}$ as

$$\Pi^{ss'}_{\mathbf{k}\mathbf{k}'} \triangleq \frac{f(E_{\mathbf{k}',s'}) - f(E_{\mathbf{k},s})}{E_{\mathbf{k}',s'} - E_{\mathbf{k},s} + \hbar\omega + i\gamma_{ss'}} \tag{A.10}$$

the unit vectors $\hat{\mathbf{u}}$ and $\hat{\boldsymbol{\varphi}}_u$ are defined as

$$\hat{\mathbf{u}}(\mathbf{k},\mathbf{q}) = \frac{\hat{\mathbf{k}}'(\mathbf{k},\mathbf{q}) + \hat{\mathbf{k}}}{\left|\hat{\mathbf{k}}'(\mathbf{k},\mathbf{q}) + \hat{\mathbf{k}}\right|} \quad , \quad \hat{\boldsymbol{\varphi}}_u(\mathbf{k},\mathbf{q}) = \hat{z} \times \hat{\mathbf{u}}(\mathbf{k},\mathbf{q}) \tag{A.11}$$

where $\hat{\mathbf{k}}'(\mathbf{k},\mathbf{q}) = (\mathbf{k}+\mathbf{q})/\left|\mathbf{k}+\mathbf{q}\right|$ . The integrand in Eq. (A.8) is explicitly writen as $\bar{\bar{\xi}}_{\mathbf{k},\mathbf{q}}$ defined below

$$\bar{\bar{\xi}}_{\mathbf{k},\mathbf{q}}(\omega) \triangleq \left(\Pi^{11}_{\mathbf{k},\mathbf{k}+\mathbf{q}} + \Pi^{22}_{\mathbf{k},\mathbf{k}+\mathbf{q}}\right)\hat{\mathbf{u}}(\mathbf{k},-\mathbf{q})\hat{\mathbf{u}}(\mathbf{k},\mathbf{q}) + \left(\Pi^{12}_{\mathbf{k},\mathbf{k}+\mathbf{q}} + \Pi^{21}_{\mathbf{k},\mathbf{k}+\mathbf{q}}\right)\hat{\boldsymbol{\varphi}}(\mathbf{k},-\mathbf{q})\hat{\boldsymbol{\varphi}}(\mathbf{k},\mathbf{q}) \tag{A.12}$$

Using Eq. A.2, the conductivity tensor associated with the transitions between the quasiparticles with the Bloch indices $\mathbf{k}$ and $\mathbf{k}+\mathbf{q}$ is then obtained as $\overline{\overline{\sigma}}^{(1)}_{\mathbf{k},\mathbf{q}} = i\overline{\overline{\xi}}_{\mathbf{k},\mathbf{q}}(\omega)/\omega$. However, as we expected, this term is diverging at lower frequencies due the pole at $\omega = 0$. It is at this point that the undesirable features of the velocity gauge manifest themselves; the diverging term appears in the optical response and therefore special care must be taken. As discussed, this singularity would be resolved in a full band calculation where all contribution are included. In order to eliminate this singularity, one can manually add a zero to the optical response to cancel out the pole existing at $\omega = 0$ and yield a physically correct result.

$$\tilde{\overline{\overline{\sigma}}}^{(1)}_{\mathbf{k},\mathbf{q}} = \frac{i}{\omega}\left[\overline{\overline{\xi}}_{\mathbf{k},\mathbf{q}}(\omega) - \overline{\overline{\xi}}_{\mathbf{k},\mathbf{q}}(0)\right] \tag{A.13}$$

Accordingly we define $\tilde{\Pi}^{ss'}_{\mathbf{k}\mathbf{k}'}$ as

$$\tilde{\Pi}^{ss'}_{\mathbf{k}\mathbf{k}'} \approx -\frac{1}{E_{\mathbf{k}',s'} - E_{\mathbf{k},s}} \frac{f(E_{\mathbf{k}',s'}) - f(E_{\mathbf{k},s})}{E_{\mathbf{k}',s'} - E_{\mathbf{k},s} + \hbar\omega + i\gamma_{ss'}} \tag{A.14}$$

which yields

$$\tilde{\overline{\overline{\sigma}}}_{\mathbf{k},\mathbf{q}}(\omega) \triangleq \left(\tilde{\Pi}^{11}_{\mathbf{k},\mathbf{k}+\mathbf{q}} + \tilde{\Pi}^{22}_{\mathbf{k},\mathbf{k}+\mathbf{q}}\right)\hat{\mathbf{u}}(\mathbf{k},-\mathbf{q})\hat{\mathbf{u}}(\mathbf{k},\mathbf{q}) + \left(\tilde{\Pi}^{12}_{\mathbf{k},\mathbf{k}+\mathbf{q}} + \tilde{\Pi}^{21}_{\mathbf{k},\mathbf{k}+\mathbf{q}}\right)\hat{\boldsymbol{\varphi}}(\mathbf{k},-\mathbf{q})\hat{\boldsymbol{\varphi}}(\mathbf{k},\mathbf{q}) \tag{A.15}$$

the conductivity tensor reads

$$\overline{\overline{\sigma}}^{(1)}(\omega,\mathbf{q}) = i\frac{e^2}{\hbar} g_s g_v \frac{1}{4\pi^2} \iint \mathrm{d}\mathcal{E}_x \mathrm{d}\mathcal{E}_y \tilde{\overline{\overline{\sigma}}}_{\mathbf{k},\mathbf{q}}(\omega) \tag{A.16}$$

where $\mathcal{E}_i = \hbar v_F k_i$ is defined to make the integral dimension less. In the long wavelength limit, the optical conductivity obtained above and the results of the calculations within the length gauge offer identical expressions for the linear conductivity tensor. It should be noted that

$$\lim_{q\to 0} \tilde{\Pi}^{ss}_{\mathbf{k},\mathbf{k}+\mathbf{q}} = \frac{\partial f(\mathcal{E}_{s,k})}{\partial \mathcal{E}} \frac{1}{\omega + i\Gamma} \tag{A.17a}$$

$$\lim_{q\to 0} \hat{\mathbf{u}}(\mathbf{k},-\mathbf{q}) = \lim_{q\to 0} \hat{\mathbf{u}}(\mathbf{k},\mathbf{q}) = \hat{\mathbf{k}} \tag{A.17b}$$

Where $\gamma_{ss} = \Gamma$ is, by definition, the intraband relaxation coefficient. This part of the conductivity is obviously responsible for the intraband dynamics manifested in the $\partial/\partial\mathbf{k}$

terms appearing in Eq. (A.1). Likewise, for the interband contribution where $s \neq s'$

$$\lim_{q\to 0} \tilde{\Pi}^{ss'}_{\mathbf{k},\mathbf{k}+\mathbf{q}} = \pm \frac{1}{2\mathcal{E}_{s,k}} \frac{f(\mathcal{E}_{k,s'}) - f(\mathcal{E}_{k,s})}{\mathcal{E}_{k,s'} - \mathcal{E}_{k,s} + \hbar\omega + i\gamma_{\mathbf{k}}} \tag{A.18a}$$

$$\lim_{q\to 0} \hat{\boldsymbol{\varphi}}(\mathbf{k}, -\mathbf{q}) = \lim_{q\to 0} \hat{\boldsymbol{\varphi}}(\mathbf{k}, \mathbf{q}) = \hat{\boldsymbol{\varphi}}_{\mathbf{k}} \tag{A.18b}$$

where $\mathcal{E}_{k,s} = -\mathcal{E}_{k,s'}$. The prefactor $1/2\mathcal{E}_{s,k}$ together with the multiplicative vector $\hat{\boldsymbol{\varphi}}_{\mathbf{k}}$ corresponds to $\boldsymbol{\zeta}_{ss'}(\mathbf{k})$ appearing in Eq. (A.1).

In closing, by removing the artificial diverging pole in the velocity gauge, both approaches yield identical results. The aforementioned pole arises due to the band space truncation and it can be removed by developing the sum rule reported in Ref. [100]. In the effective two-band model, the velocity gauge should be repaired to account for the nonphysical terms and as a result, the perturbative treatment of the optical response of graphene within the velocity gauge, in its original form, is not perfectly reliable. The length gauge can be consistently employed to develop a full theoretical model for the nonlinear optics of graphene.

# Appendix B

# Dynamics and Effective Relaxation Coefficients

The adopted theoretical models for graphene in this thesis are based on single particle picture that treats many body effects at the phenomenological level. In some circumstances, a more accurate inclusion of the relaxation coefficients would provide a substantial improvement in understanding the underlying physics. Striving to use a single particle description of the electron dynamics in graphene, the many body effects are analyzed within a microscopic theory (detailed below) and the microscopic relaxation coefficients (k-depend coefficients) are obtained numerically by means of a long pulse excitation. Inspired by the practical methods of measurement in the laboratory, we excite graphene within the many-body model by a long and sharp edged pulse to resolve the relaxation time for the microscopic polarization $\mathcal{P}(\mathbf{k}, t)$ and the population $\mathcal{N}(\mathbf{k}, t)$.

### B.0.1 Model Description

We have utilized [1] the microscopic model developed in Ref. [114] which takes in to account the Coulomb and phonon-induced relaxation channels. The adopted model employs a many-body Hamiltonian which consists of the free carriers (electron and phonon) part $H_0$, the carrier field $H_{c-f}$, and the carrier-carrier and carrier phonon Hamiltonians which are represented by $H_{c-c}$ and $H_{c-p}$ respectively [114]

$$H = H_0 + H_{c-f} + H_{c-c} + H_{c-p} \tag{B.1}$$

[1] In collaboration with Chalmers University of Technology, Philippe Tassin, Ermin Malic and Roland Jago

The approximations existing in the model are concisely outlined as follows .

(i) The free carriers (band induced) Hamiltonian $H_0$ consists of free electron and free phonon dynamics. The free electron Hamiltonian is constructed based on a full band model beyond the Dirac cone approximation for weakly bounded $2p_z$ orbitals. The full-band model is capable of resolving exciting effects in the absorption spectrum of graphene. More importantly, phonon induced intervalley scattering is efficiently modeled in the full-band Hamiltonian. The Hamiltonian $H_0$ also contains the dispersion of the free phonons including both the optical and acoustic ones. The optical phonons possess two sharp kinks in their dispersion around the high symmetry points [183]. The corresponding phonon modes causes strong electron-phonon coupling which in turn yields nonzero population relaxation around the Dirac points [114].

(ii) The carrier-field coupling ($H_{c-f}$) is obtained using minimal coupling into the conical momentum. Since we are using a full-band model, the velocity gauge offers reliable results and the issues discussed in Appendix A would not lead to trouble.

(iii) The electron-electron interaction has been modeled within the first order mean-field Hartree-Fock approximation. The electrostatic screen effect is calculated using an effective single-particle picture that leads to the Lindhard approximation of the dielectric function. It is worth pointing out that the calculations are carried out in the static limit. The low energy excitations (particularly those ones in the vicinity of the Dirac points) are minimally affected by this approximation. Many body dephasing due to radiation is almost nonexistent in low frequency limit due to the reduced phase space accessible to the low energy photons.

(iv) The electron -phonon coupling ($H_{c-p}$) is also obtained accurately using phonon-induced defamation potentials. The appropriate potential functions for the optical and acoustic phonons are calculated in Refs. [183].

### B.0.2 Effective Relaxation Coefficients

The numerical estimation of the microscopic relaxation dynamics is carried out by *projecting* the many body dynamics into the SBEs obtained from the reduced Liouville equation. In compliance with the mathematical structure of the SBEs, we excite the graphene Bloch equations (full microscopic dynamics) with a relatively long and sharp-edged pulse and capture the relaxation time scale. The long duration of the optical excitation allows us to capture the steady state dynamics and the sharp edged nature of the excitation facilitates

time domain characterization of the microscopic relaxation coefficients. As per SBEs, we basically curve-fit the envelope of the microscopic polarization and population (after the pulse is tuned off) to an exponential decay. The numerical steps are outlined below.

1. Use Hilbert transform to capture the envelope of the microscopic polarization.
2. Use low pass filter to get rid of higher harmonics contents in the polarization envelope as well as the population pulsations.
3. Curve-fit the decay part of the dynamics to an exponential function. The decay of the microscopic polarization is $\gamma_{\mathbf{k}}^{(2)}$ and that of the population is $\gamma_{\mathbf{k}}^{(1)}$.

Figures B.1 and B.2 display the steps followed to extract the microscopic relaxation coefficients for the pulse excitation of $\hbar\omega = 80$meV and 800meV respectively. It is assumed that the amplitude of the electric fields for the both optical pulses are $E_0 = 10^6$V/m. The duration of the pulses have been selected to be 800fs and 400fs for the cases of 80meV and 800meV respectively.

The results of calculations for a few distinct points over the k-space are shown in Fig. B.3. As expected, the low energy excitation offers significantly slow relaxation dynamics. It is also worth noting that, unlike the coherence dephasing coefficient $\gamma_k^{(2)}$, the coefficient $\gamma_k^{(1)}$ tends to be negligibly small in the vicinity of the Dirac point. This would lead to a pronounced saturation effect. The red solid lines are the fitted exponential (decay) functions. For the case of microscopic polarization the envelope of the curved needs to be captured where $\mathcal{HP}$ stands for the Hilbert transformed of the polarization. The calculations are shown for two district points over the reciprocal space (low energy around the Dirac point and a high energy slightly higher than the zero detuning region)

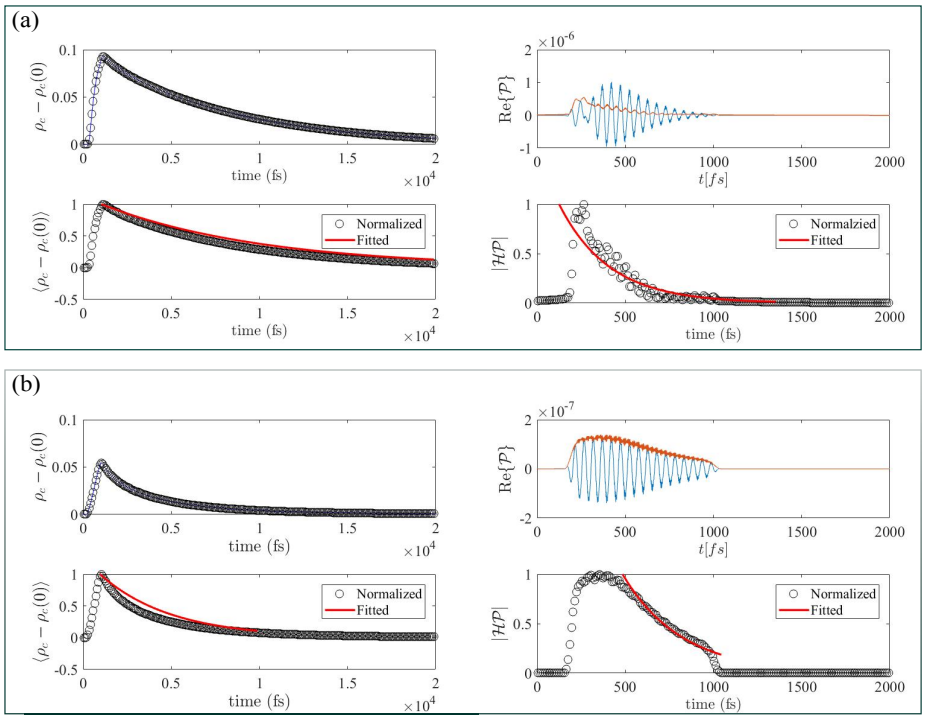


Figure B.1: Extraction of the microscopic relaxation coefficients for the optical excitation of $\hbar\omega = 80$meV at (a) $\hbar v_F k = 10$meV(low energy) and (b) for $\hbar v_F k = 100$meV (high energy) points.

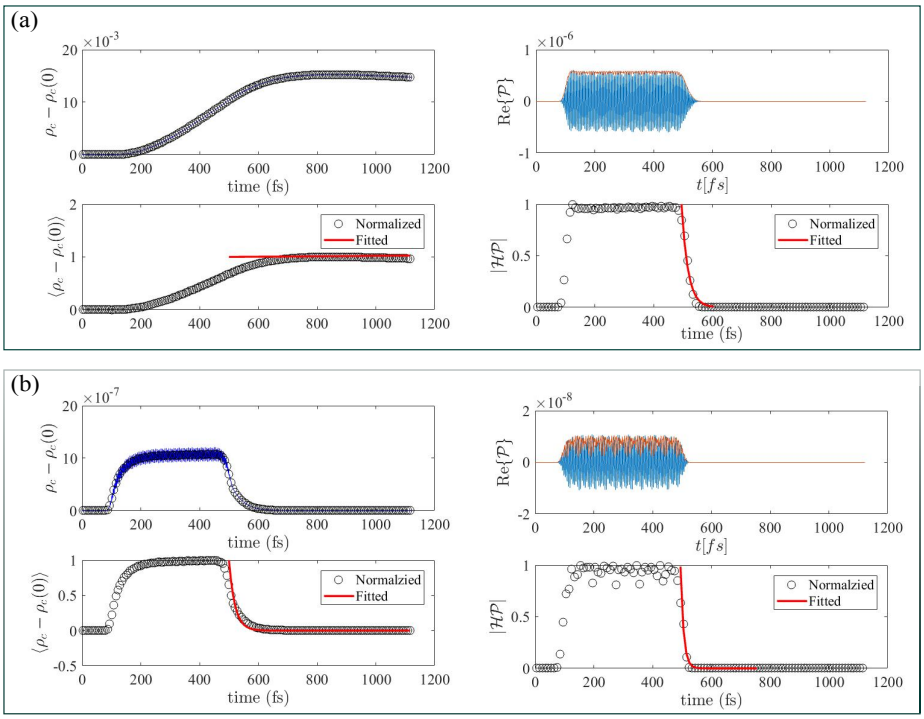


Figure B.2: Extraction of the microscopic relaxation coefficients for the optical excitation of $\hbar\omega = 800$meV at (a) $\hbar v_F k = 50$meV(low energy) and (b) for $\hbar v_F k = 500$meV (high energy) points.

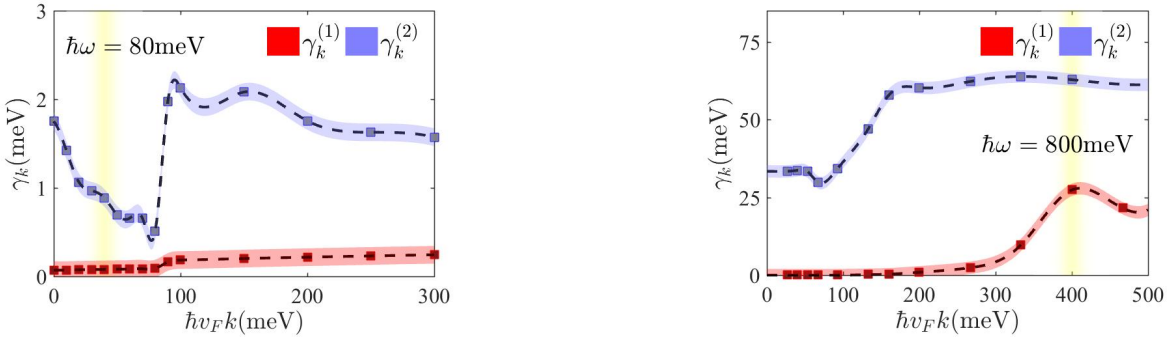


(a) (b)

Figure B.3: k-dependent relaxation coefficients $\gamma_{\mathbf{k}}^{(1)}$ and $\gamma_{\mathbf{k}}^{(2)}$ for an undoped graphene. The yellow shaded regions are the zero detuning regions

# Appendix C

# Nonperturbative Kerr Type Nonlinearity of Graphene

A nonperturbative formulation of the Kerr effect in graphene is obtained by taking the steady state population difference as the optically modified inversion. In the steady state analysis, essentially only one-photon processes are retained. The impact of higher order effects including two photon absorption (TPA) is then incorporated into the response function via additional complex contributions to the population difference. By substituting *the effective complex population difference* into the linear response theory, one obtains the induced interband nonlinear current as

$$\vec{NL}_1(\omega) = -\frac{e^2}{\hbar} v_F g_s g_v D \iint_{\mathrm{RBZ}} \mathrm{d}\mathbf{k}^2 \left\{ \hat{\varphi}_{\mathbf{k}} (\hat{\varphi}_{\mathbf{k}} \cdot \mathbf{E}) \frac{1}{k} \mathcal{L}_{\mathbf{k}}(\omega) \left[ \widetilde{\mathcal{N}}^{st}_{\mathbf{k}} + \delta\mathcal{N}^{TPA}_{\mathbf{k}} + \delta\mathcal{N}^{B}_{\mathbf{k}} - \mathcal{N}^{eq}_{\mathbf{k}} \right] \right\} \tag{C.1}$$

where the complex function $\delta\mathcal{N}^{TPA}_{\mathbf{k}}$ accounts for the population oscillations at the second harmonics of excitation. In the dressed state picture, TPA is conceived as the absorption of two subsequent photons via a virtual state. In the density matrix formulation, that contribution results in the oscillation of the population difference at the second harmonic. By expanding the inversion as $\mathcal{N}_{\mathbf{k}} \approx \widetilde{\mathcal{N}}^{st}_{\mathbf{k}} + (\mathcal{N}^{(2)}_{\mathbf{k}} \exp(i2\omega t) + c.c.)$ and plugging into the SBEs one obtained the complex contribution to the inversion as

$$\delta\mathcal{N}^{TPA}_{\mathbf{k}} = -\frac{1}{2} \mathcal{L}_{\mathbf{k}}(\omega) \frac{|\widetilde{\Phi}_{\mathbf{k}}|^2}{\gamma^{(1)}_{\mathbf{k}} + 2i\omega} \widetilde{\mathcal{N}}^{st}_{\mathbf{k}} \tag{C.2}$$

The second contribution $\delta\mathcal{N}^{B}_{\mathbf{k}}$ enters due to intraband dynamics or Boltzman type transport. According to Eq. (2.34), the intraband dynamics can be incorporated by displacing

the density matrix in k-space by $\Delta\mathbf{k}$. As a result of two subsequent translations conducted by two conjugate fields with the frequency of $\omega$ and $-\omega$, the steady state population difference experiences a minor change denoted by $\delta\mathcal{N}_{\mathbf{k}}^{B}$. By Taylor expanding the population, one obtains

$$\delta\mathcal{N}_{\mathbf{k}}^{B} = \frac{e^2}{\hbar^2(\omega^2+\Gamma^2)}(\mathbf{E}\cdot\nabla_{\mathbf{k}})(\mathbf{E}^{*}\cdot\nabla_{\mathbf{k}})\widetilde{\mathcal{N}}_{\mathbf{k}}^{st} \tag{C.3}$$

Similarly the intraband nonlinear response reads

$$\vec{NL}_2 \approx \frac{e^2 v_F g_s g_v D}{i\omega+\Gamma}\iint_{\mathrm{RBZ}} \mathrm{d}\mathbf{k}^2 \left\{\hat{\mathbf{k}}\mathbf{E}\cdot\nabla_{\mathbf{k}}\left[\widetilde{\mathcal{N}}_{\mathbf{k}}^{st}+\delta\mathcal{N}_{\mathbf{k}}^{B}-\mathcal{N}_{\mathbf{k}}^{eq}\right]\right\} \tag{C.4}$$

# Appendix D

# Scattering matrix calculation of the Bragg mirror, graphene layer and the plasmonic meta-surface

**Scattering Matrix of the Multilayer Structure**

The scattering matrix of the multilayer structure described in Chpater 3 is obtained by calculating the reflection from the layered media illuminated by the $\mathrm{TE}_{mn}$ and $\mathrm{TM}_{mn}$ Floquet modes. This goal can be readily achieved by means of the transfer matrix method [169]. The overall transfer matrix of the multilayer structure relating the expansion coefficients of the Floquet mode labeled by $mn$ and the polarization index $i$ is the multiplication of the transfer matrices in the intermediate layers [169].

$$\overline{M}^{(\alpha)} = \overline{M}^{(\alpha)}_{N-1,N} \cdots \overline{M}^{(\alpha)}_{1,2} \overline{M}^{(\alpha)}_{0,1} \tag{D.1}$$

where $N$ is the number of the layers and the matrices $\overline{M}^{(\alpha)}_{l-1,l}$'s are the transfer matrices in the intermediate layers relating the expansion coefficients of waves propagating in $\pm\hat{z}$ directions at $(l-1)$'th layer to those of the $l$'th layer.

$$\overline{M}^{(i=1,mn)}_{l-1,l} = \begin{bmatrix} e^{-j\phi_{l-1}} \left(1 + \frac{k_z^{(l-1,mn)} n_l^2}{k_z^{(l,mn)} n_{l-1}^2}\right) & e^{j\phi_{l-1}} \left(1 + \frac{k_z^{(l-1,mn)} n_l^2}{k_z^{(l,mn)} n_{l-1}^2}\right) \\ e^{-j\phi_{l-1}} \left(1 + \frac{k_z^{(l-1,mn)} n_l^2}{k_z^{(l,mn)} n_{l-1}^2}\right) & e^{j\phi_{l-1}} \left(1 + \frac{k_z^{(l-1,mn)} n_l^2}{k_z^{(l,mn)} n_{l-1}^2}\right) \end{bmatrix} \tag{D.2}$$

$$\overline{M}_{l-1,l}^{(i=2,mn)} = \begin{bmatrix} e^{-j\phi_{l-1}}\left(1+\frac{k_z^{(l-1,mn)}}{k_z^{(l,mn)}}\right) & e^{j\phi_{l-1}}\left(1+\frac{k_z^{(l-1,mn)}}{k_z^{(l,mn)}}\right) \\ e^{-j\phi_{l-1}}\left(1+\frac{k_z^{(l-1,mn)}}{k_z^{(l,mn)}}\right) & e^{j\phi_{l-1}}\left(1+\frac{k_z^{(l-1,mn)}}{k_z^{(l,mn)}}\right) \end{bmatrix} \tag{D.3}$$

the phase $\phi_l$'s are defined as $\phi_l \triangleq k_z^{(l,mn)} t_l$ and the longitudinal wave number is obtained as

$$k_z^{(l,mn)} = \sqrt{n_l^2 k_0^2 - |\mathbf{k}_{mn}|^2} \quad , \quad \mathrm{Im}\left\{k_z^{(l,mn)}\right\} < 0$$

The layered media possesses the planar symmetry and thereby the reflected signal conserves the lateral variations as well as the polarization of the incident wave. As a result, the scattering matrix associated with the multilayer structure is diagonal and is given by

$$S_M^{\alpha\alpha'} = -\frac{M_{21}^{(\alpha)}}{M_{22}^{(\alpha)}}\delta_{\alpha\alpha'} \tag{D.4}$$

where $\delta_{\alpha\alpha'}$ is the Kronecker delta function.

**Scattering Matrix of the Graphene Layer**

The linear conductivity tensor of doped graphene layers has been calculated in chapter 2. Graphene as a 2D material conserves the transverse variations of the illuminating electromagnetic field in the linear domain. However, the scattered field does not have the same polarization as the incident wave. The scattering matrix of graphene $\overline{S}_G$ therefore is diagonal in the $mn$ subspace but not in the polarization $(i)$ subspace. The scattering of the TE and TM Floquet modes from a free-standing graphene layer is obtained by satisfying the boundary conditions. The total induced field is related to the excitation coefficient of the corresponding Floquet mode $mn$ as

$$\begin{bmatrix} V^{(TM)} \\ V^{(TE)} \end{bmatrix}_{total} = \overline{A}^{(mn)^{-1}} \begin{bmatrix} V^{(TM)} \\ V^{(TE)} \end{bmatrix}_{incident} \tag{D.5}$$

where the $2 \times 2$ matrix $\overline{A}^{(mn)}$ is defined as

$$\overline{A}^{(mn)} = \overline{U} + \frac{1}{2}\begin{bmatrix} Z^{TM} & 0 \\ 0 & Z^{TE} \end{bmatrix}\begin{bmatrix} \sigma_{\kappa\kappa}^{(1)} & \sigma_{\kappa\xi}^{(1)} \\ \sigma_{\xi\kappa}^{(1)} & \sigma_{\xi\xi}^{(1)} \end{bmatrix} \tag{D.6}$$

$$Z^{TE} = \eta_0 \frac{k_0}{k_z^{mn}} \quad , \quad Z^{TM} = \eta_0 \frac{k_z^{mn}}{k_0} \tag{D.7}$$

where $\overline{U}$ is the $2 \times 2$ identity matrix and $\eta_0 = \sqrt{\mu_0/\varepsilon_0}$ is the free space characteristic impedance. The conductivity tensor containing $\sigma_{\kappa\kappa}^{(1)}$, $\sigma_{\xi\xi}^{(1)}$ ,$\sigma_{\kappa\xi}^{(1)}$ and $\sigma_{\xi\kappa}^{(1)}$ are given in the supplementary information. For mathematical convenience, we define $\overline{C}^{(mn)} = \overline{A}^{(mn)^{-1}}$. The scattering matrix is then calculated as

$$S_G^{\gamma\gamma'} = \delta_{mn,m'n'} \left( \overline{C}_{ii'}^{(mn)} - \delta_{ii'}\delta_{pp'} \right) \tag{D.8}$$

**Scattering Matrix of the Nanoparticles Array**

The scattering matrix relating the incident and reflected Floquet modes in the nanoparticle array, the Generalized Multipole Technique (GMT) is proposed [29]. We assume that the suspended array shown in Fig. 3.4 is excited by $\mathbf{E}_i^{(\gamma)}$

$$\mathbf{E}_i^{(\gamma)} = \left\{ \left( \hat{\kappa}_{mn} \mp \frac{|\mathbf{k}_{mn}|}{k_z^{mn}} \hat{z} \right) \delta_{i,1} + \hat{\xi}_{mn} \delta_{i,2} \right\} \exp\left[ -j(\mathbf{k}_{mn}.\boldsymbol{\rho} + k_z^{m'n'} |z - z_p|) \right] \tag{D.9}$$

where $z_p$ is the location of the channel $p$. The scattering of the incident field $\mathbf{E}_i^{(\gamma)}$ by the nanoparticle array is calculated via GMT. The details of GMT analysis are presented in the appendix E. Assume that $\mathbf{E}_s^{\gamma}(x, y, z)$ is the electric field scattered from the nanoparticles array. The scattered field is obtained from from GMT analysis. The scattering matrix is then related to the modal coefficients of the scattered field $\mathbf{E}_s^{\gamma}(x, y, z)$ as

$$S_P^{\gamma\gamma'} = \boldsymbol{\mathcal{E}}_{m'n',p'}^{\gamma} \cdot \left( \delta_{i'1} \hat{\kappa}_{m'n'} + \delta_{i'2} \hat{\xi}_{m'n'} \right) + (1 - \delta_{pp'}) \left[ 1 + e^{-jk_z^{mn} |z_p - z_p'|} \right] \tag{D.10}$$

where $\boldsymbol{\mathcal{E}}_{m'n',p'}^{\gamma}$ are calculated via the inverse Fourier integral

$$\boldsymbol{\mathcal{E}}_{m'n',p'}^{\gamma} = \frac{1}{WL} \iint_{\text{unit cell}} \mathbf{E}_s^{\gamma}(x, y, z = z_{p'}). \exp(j\mathbf{k}_{mn}.\boldsymbol{\rho}) \mathrm{d}x\mathrm{d}y \tag{D.11}$$

# Appendix E

# GMT Analysis of Nanodisk Array

Fig. E.1 shows the multipole setting used to simulate the cylinder nanoparticle. Spherical multipoles of the Maxwell's equation are used as three dimensional (3D) expansion wave functions in each region. The radial components of $\mathrm{TE}_r$ and $\mathrm{TM}_r$ multipoles can be written as [184]

$$E_r^{nm} = \frac{n(n+1)}{j\omega\varepsilon r^2} P_n^m(\cos\theta)\hat{H}_n^{(2)}(kr)e^{jm\phi} \qquad -n \le m \le n \tag{E.1a}$$

$$H_r^{nm} = \frac{n(n+1)}{j\omega\mu r^2} P_n^m(\cos\theta)\hat{H}_n^{(2)}(kr)e^{jm\phi} \qquad -n \le m \le n \tag{E.1b}$$

where $P_n^m$ are the associated Legendre polynomials and $\hat{H}_n^{(2)}$ are the Schelkunoff-Hankel functions of the second kind. The multipoles shown by circles and stars generate the field inside the cylinder while the rest of multipoles generate the field in the periodic cell and outside the cylinder. To capture the edge effects of the cylinder nanoparticle, a series of multipoles are placed in the vicinity of edges. Between each two multipoles that are connected with a line, there are 11 multipoles that their coefficients are linearly dependent to the edge multipoles. Using this approach it is possible to model the smooth field variation around the edge while keeping the number of multipoles as low as possible [29]. Figures E.1(a) and E.1(b) show the actual location of multipoles used in the simulation. The maximum order of spherical multipoles is $n = 2$ associated with the maximum order of Legendre polynomials. We verified the developed code using the result of HFSS and also by checking the convergence of results as the number of multipoles changes.

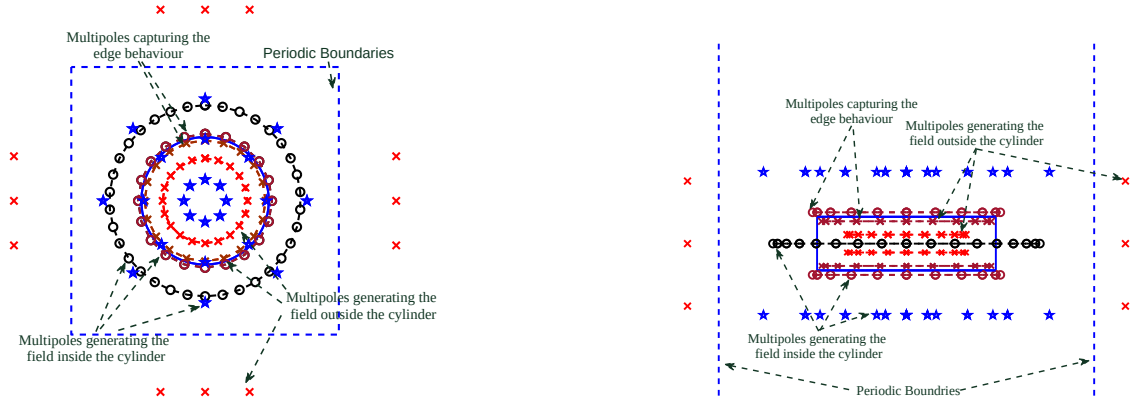


(a) (b)

Figure E.1: Multipole arrangement used in chapter 3 for the GMT analysis of the periodic nanodisk array.

# Appendix F

# Calculation of Conversion Efficiency

A typical high power pulsed-laser generates Gaussian (in time) optical pules modulated around the center frequency $\omega_0$ with the reparation rate of $R_n$. The repetition rate is always low enough to safely assume that the frequency tripler only mixes up the individual Gaussian packs. Henceforth, every Gaussian pack is treated independently. The time dependence of the $\alpha$'th component of the incident electric field is given by $S_\alpha(t)$. The $\xi$'th component of the generated third harmonic signal, $S_\xi^{out}$, is obtained from the following convolution integral

$$S_\xi^{out}(\Omega) = \sum_{\alpha\beta\gamma}\sum_{ijkl}\int \mathrm{d}\omega_p \int \mathrm{d}\omega_q \sigma^{(3)}_{ijkl}(\Omega-\omega_p-\omega_q,\omega_p,\omega_q) \\ G^{ijkl}_{\xi,\alpha\beta\gamma} S_\alpha(\Omega-\omega_p,\omega_q) S_\beta(\omega_p) S_\gamma(\omega_q) \quad \text{(F.1)}$$

Where $\sigma^{(3)}$ is the third order conductivity of the graphene layer (see supplemental information). The frequencies $\omega_p$ and $\omega_q$ run over the fundamental frequency band and The *gain function* $G^{ijkl}_{\xi,\alpha\beta\gamma}$ is obtained from the network analysis outlined in section 3.4.

$$G^{ijkl}_{\xi,\alpha\beta\gamma}(\Omega,\omega_p,\omega_q) \triangleq Z_{\xi i}(\Omega) T_{j\alpha}(\Omega-\omega_p-\omega_q) T_{k\beta}(\omega_p) T_{l\gamma}(\omega_q) \quad \text{(F.2)}$$

The functions $T_{ab}(\omega)$, $Z_{ab}(\Omega)$ are the transfer functions at the fundamental and third harmonic bands respectively and they are obtained from the network shown in Fig. 3.4. Accordingly, the transfer function $T_{ab}(\omega)$ gives the $a$'th component of the electric field induced at the graphene layer (at the fundamental frequency band) excited by the $b$'th component of the incident field. The mutual impedance $Z_{ab}(\Omega)$ is defined as the ratio of the $a$'th component of the electric field induced right on top of the structure (correspond

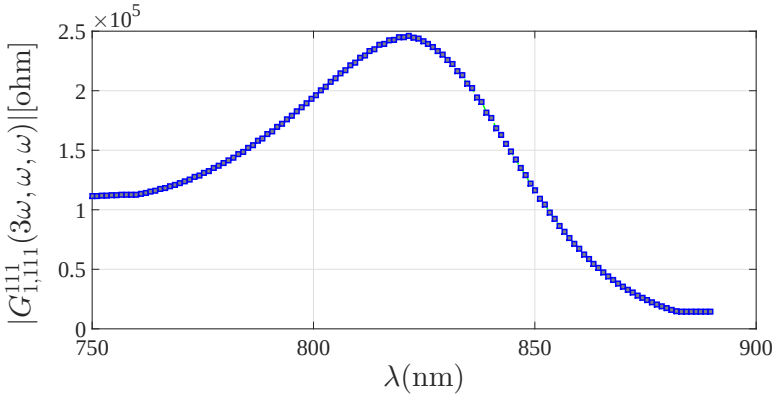


Figure F.1: Gain function $|G^{1111}_{1,111}(3\omega,\omega,\omega)|$ versus the wavelength $\lambda$ corresponding to the fundamental frequency $\omega$.

to the $AA'$ cross section in Fig. 3.4) at the frequency of $\Omega$ to the $b$'th component of the third harmonic current induced over the graphene layer (correspond to $\overline{I}(\Omega = 3\omega)$ ). In order to get an idea about the magnitude of the gain function, $\left|G^{1111}_{1,111}(3\omega,\omega,\omega)\right|$ is plotted in Fig. F.1.